eXPRESS Polymer Letters Vol.10, No.6 (2016) 438
Available online at www.expresspolymlett.com
DOI: 10.3144/expresspolymlett.2016.41

Editorial corner – a personal view
Polymer technology and bioengineering – which learns from the other?

Gy. Marosi[*]

Organic Chemistry and Technology Department of Budapest University of Technology and Economics, H-1111 Budapest, Műegyetem rkp. 3, Hungary

From the technological point of view pharmaceutical and biomedical engineering remained underdeveloped for a long time compared to the polymer industry, in spite of their high scientific respect and good financial background. Economic and versatile continuous polymer technologies (such as extrusion injection molding, fiber and film formation) started to revolutionize the pharmaceutical industry just recently replacing mature batch methods. While pharmaceutical extrusion has already been introduced into the industrial practice by some leading pharma-market players other methods, such as two component injection molding; electro-spinning; melt blowing; 3D printing and supercritical-extrusion, are only at the exploratory stage. Polymer research gained new impetus in the health related application fields focusing on molecular mobility; polymorphism; T_g manipulation; chemical-physical stability; shape memory; and interactions with biomolecules or living organs. While trying to influence these factors effectively well-established polymer technologies became under spotlight of interest and their new potential (e.g. capability for controlling the structure accurately) are recognized. On the other hand, instead of the robust mass production of the plastic industry much subtler treatment is required for processing the very sensitive substances used in the biopharmaceutical industry. Efforts to meet these requirements induce technological innovations such as new alternating current (AC) electrospinning for the formation of drug loaded nanofibers and bio-printing for constructing organs from stem cells. Polymers, optimized for the purposes of pharmaceutical and tissue engineering, have to be developed and their manufacturing needs to be combined with real time monitoring (e.g. Raman or other spectroscopic techniques) and strict closed loop control of the product quality. Authorities promote this approach, called Process Analytical Technology (PAT), through their recent directives. There is a chance now for utilizing the recent advancement in the combination of biotechnology and polymer processing, achieved by the health related polymer researches, for unique engineering purposes (e.g. controlled release of protecting substances, microbiological protection against fouling, 3D printing of enzyme-activated energy harnessing systems, etc.). It is the right time now for refreshing the polymer engineering-related knowledge by considering the achievements of pharma- and bioengineering.

Prof. Dr. György Marosi
Member of International Advisory Board

[*]Corresponding author, e-mail: gmarosi@mail.bme.hu

eXPRESS Polymer Letters Vol.10, No.6 (2016) 439–449
Available online at www.expresspolymlett.com
DOI: 10.3144/expresspolymlett.2016.42

An orthogonal, one-pot, simultaneous UV-mediated route to thiol-ene/sol-gel film

A. Chemtob[1], H. De Paz-Simon[1], M. Sibeaud[1], B. El Fouhali[1], C. Croutxé-Barghorn[1], L. Jacomine[2], Ch. Gauthier[2], V. Le Houérou[2]*

[1]Laboratory of Macromolecular Photochemistry and Engineering, University of Haute-Alsace, EA 4567, ENSCMu, 3 bis rue Alfred Werner, 68093 Mulhouse Cedex, France
[2]Institut Charles Sadron, CNRS, UPR 22, University of Strasbourg, 23 Rue du Loess, BP 84047, 67034 Strasbourg Cedex 2, France

Received 9 October 2015; accepted in revised form 22 December 2015

Abstract. We describe a novel combination of orthogonal reactions based on UV-driven thiol–ene and alkoxysilyl condensation reactions to form a single-step route toward thioether-bridged silsesquioxane films. Our chemical strategy consists of using two bifunctional (meth)acrylate (**E**) and propanethiol (**T**) trimethoxysilyl precursors containing two complementary functional moieties for thiol-ene coupling and sol-gel process. The reaction kinetics revealed that c.a. 85% of thiol and ene conversions were consumed concomitantly. Meanwhile, a complete hydrolysis was accomplished, affording ultimately a high degree of condensation (81%). Emphasis was placed on differences of mechanical properties between sol-gel hybrids resulting from thiol-ene reaction (**E-T** mixture) and ene homopolymerization (**E** only) using scratch test measurements. For the methacrylate system, the formation of thioether linkages within a vitreous silica network emerged as a useful strategy for the formation of a uniform, low-stress and flexible crosslinked hybrid structure. Enhanced mechanical properties were manifested by an expanded elastic domain, and better resistance to cracking. Moreover, there are clear indications that mechanical properties can be easily tuned upon varying the ratio of the two hybrid precursors.

Keywords: *mechanical properties, thiol-ene, nanocomposites, photopolymerization, UV irradiation*

1. Introduction

The revival of 'thiol-ene' reaction, which refers to the radical-mediated addition of thiol across terminal alkene, hinges mainly on some essential factors: accessibility of raw materials, mild reaction conditions, efficiency and chemoselectivity [1, 2]. The last feature refers to the fact that this coupling reaction can be 'orthogonal' to a broad array of reagents, solvents, and functional groups. Thiol-ene orthogonality [3] has already paved the way for step-growth polymerizations and chain functionalizations performed in a wide range of chemical environments: aerated [4] and aqueous [5] conditions for example, or in the presence of biological [6] and complex [7] systems. The recent combination of thiol-ene with sol-gel chemistry provides another perfect illustration of this tolerance, because this inorganic polymerization process generally entails water and alcoholic solvents/byproducts, acid or base catalysts, and precursors bearing chloro or alkoxy hydrolyzable reactive groups [8]. However, most of the reported synthesis methodologies remain sequential describing a thiol-ene step uncoupled from the sol-gel process [9]. In most instances, the (photoinduced) thiol-ene cross-linking was thus carried out subsequently from isolated and purified thiol- or vinyl-functionalized hybrid building blocks including silsesquioxanes [10–17], POSS (polyoligomeric silsesquiox-

*Corresponding author, e-mail: abraham.chemtob@uha.fr

ane) cages [18, 19] or zirconium oxoclusters [20], all prepared separately. These approaches were derived from the conventional two-step route used to synthesize hybrid sol-gel photopolymer films via radical or cationic photopolymerization [21]. Complementing a thiol-ene network with an intimately mixed silica or oxide matrix is clearly part of a wider strategy to improve its mechanical properties, which are usually plagued by low glass transition temperature and poor cross-link densities [22]. Although the aforementioned approaches claimed notable improvements in properties such as abrasion resistance, thermal stability [12] or refractive index [23], they do not allow optimum use of thiol-ene orthogonality, raising hopes that synthesis conditions could be dramatically improved.

We describe herein a combination of two photoinduced orthogonal reactions based on thiol–ene and alkoxysilyl sol-gel condensation toward the rapid formation of thioether-siloxane nanocomposite films. As outlined in Figure 1, this novel approach focuses on simultaneous, one-pot reactions, thereby minimizing the number of required synthetic steps and reducing the number of work-up and purification operations. Our chemical strategy consists of using a bifunctional monomer – 3-(trimethoxysilyl)propyl methacrylate (**E$_1$**) or acrylate (**E$_2$**) – containing two complementary ene and trimethoxysilyl functional moieties for thiol-ene and sol-gel process, respectively. This latter is coupled with 3-(trimethoxysilyl)-1-propanethiol (**T**) to form a single-step route toward thioether-bridged silsesquioxane films (if no

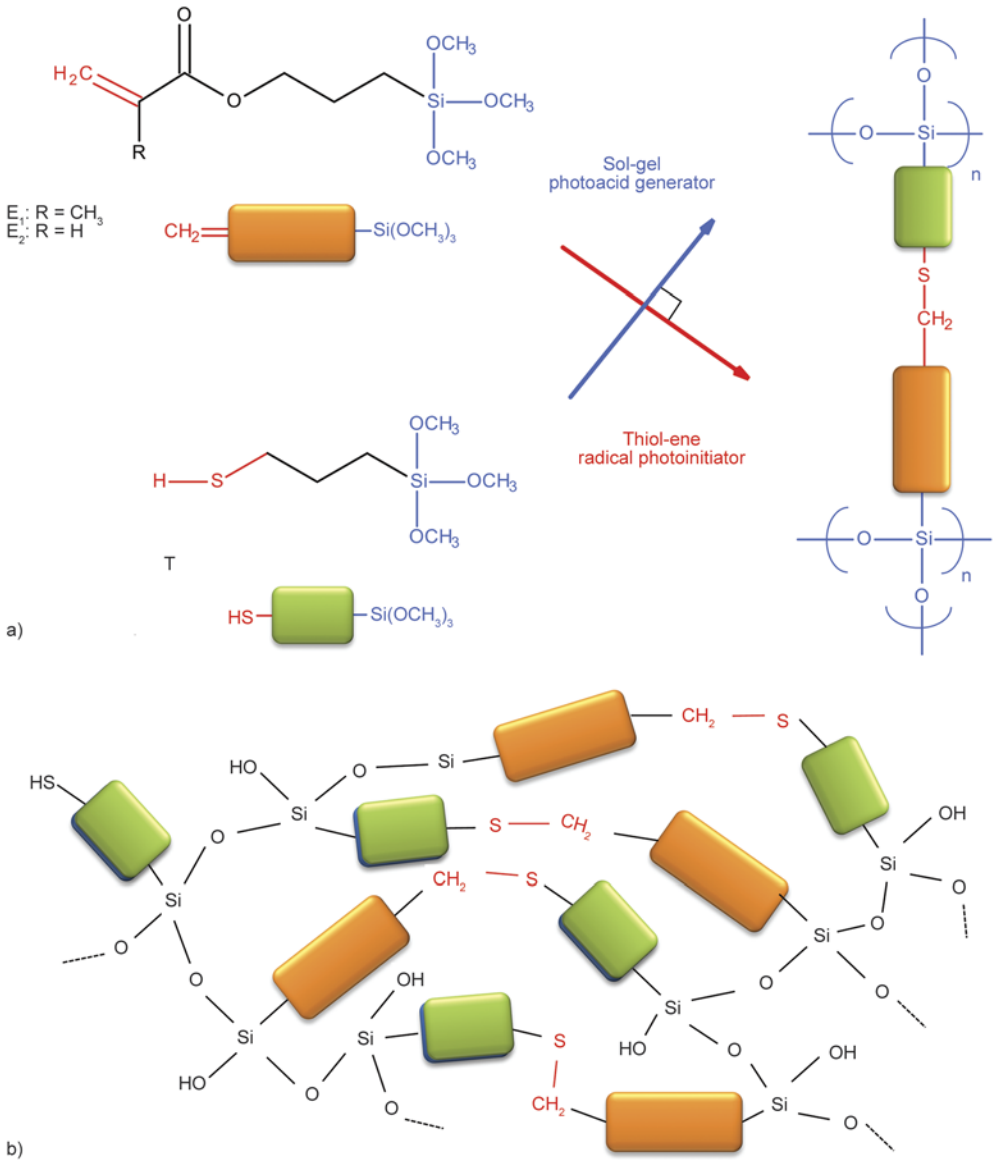

Figure 1. a) An orthogonal coupling strategy was developed by combining thiol–ene and sol-gel reactions for the synthesis of hybrid thiol-ene films. b) schematic representation of the thioether-bridged silsesquioxane network

homopolymerization of ene occurs) represented in Figure 1. Thiol-ene is photochemically triggered by the aid of a radical photoinitiator, while sol-gel process is catalyzed through the release of photoacids. The concept of sol-gel photopolymerization of silicon alkoxide-based films has the peculiar advantages of proceeding in bulk, thus avoiding solvent or water addition, and sol-gel transition. Nevertheless, it proceeds through a hydrolysis-condensation mechanism, entirely similar to that of a conventional hydrolytic sol-gel process [24, 25]. Catalysis is mediated by photogenerated Brönsted superacids, while the hydrolysis stage relies on the permeation of air moisture. The high chemoselectivity of thiol-ene allows it to form a highly orthogonal reaction pair with photoacid-catalyzed hydrolysis-condensation of the trimethoxysilyl groups. Additionally, this route obviates the necessity for solvent, deprotection/activation steps, or thermal densification of the oxo-polymer network.

In contrast to chain-growth polymerization leading to multiple additions, thiol-ene is a true coupling reaction as a single S–C bond arises from the net addition of thiol across an ene. The resulting benefit is the formation of a well-defined silsesquioxane network including fewer crosslinks and flexible thioether bridges able to offset silica brittleness and residual stress. Emphasis was placed on the possible differences of mechanical responses between sol-gel hybrids resulting from thiol-ene reaction and ene homopolymerization since little study has been done so far on this subject. In our case, the choice of (meth)acrylate precursors (**E**) able to undergo both reactions creates an opportunity to elucidate their distinct mechanical behaviors. Unlike main approaches in the literature based on dynamic mechanical analysis, we investigated surface properties through scratch test apparatus equipped with *in situ* visualization and image-analysis protocol. This technique can provide new insight into the adhesion of the hybrid films, elasto-plastic properties of the film material, fracture mechanism, and more generally resistance to scratch.

2. Experimental section

2.1. Materials

3-(Trimethoxysilyl)-1-propanethiol (**T**, 98 mol%), 3-(trimethoxysilyl)propyl methacrylate ($\mathbf{E_1}$, 98 mol%) and acrylate ($\mathbf{E_2}$, 98 mol%) were purchased from Sigma-Aldrich and used without further purification. 4-methylphenyl)[4-(2-methylpropyl)phenyl] iodonium hexafluorophosphate (Irgacure 250, 75 wt% in propylene carbonate) is a ionic photoacid generator provided by BASF and used to photocatalyze the inorganic photopolymerization. The radical photoinitiator for thiol-ene coupling or ene homopolymerization is 2-hydroxy-2-methyl-1-phenyl-propan-1-one (Darocur 1173) kindly provided by BASF. The silicon wafer (100) substrate was purchased from SILTRONIX Silicon Technologies. Optically polished BaF_2 IR windows (25×5 mm) were purchased from Korth Kristalle GmbH.

2.2. Hybrid thiol-ene film preparation

2 wt% of I250 and D1173 were added to a $\mathbf{T\text{-}E_i}$ thiol-ene mixture containing an equimolar ratio in SH and C=C functions. Before UV exposure, the homogeneous and solvent-free formulations were cast onto two different substrates (BaF_2 pellet or borosilicate glass) using a wire-wound bar to yield a liquid film with a thickness of 3.8±0.2 μm. BaF_2 substrate was employed for real-time Fourier transform infrared (RT-FTIR) experiments. In this specific case, irradiation was performed at room temperature with simultaneous exposure to UV and IR analytical beam during 200 s. As UV source, a polychromatic mercury-xenon lamp (Hamamatsu, L8252, 200 W, 365 nm reflector) was used, which covers a broad continuous spectrum spanning from short-wavelength UV to infrared (250–2000 nm). This lamp was connected to a flexible light-guide to generate a spot light beam on the film sample and an elliptical cold reflector was added to prevent any adverse effects from heat (IR radiation). In the spectral region between 250 and 600 nm, the light irradiance I was estimated at 600 $mW \cdot cm^{-2}$. After the irradiation process, the temperature increase was very limited (<2 °C), neglecting any thermal contribution to the sol-gel process. All measurements were repeated at least three times and reproducible results were obtained. Larger films dedicated to mechanical characterization and solid-state NMR analysis were prepared with the same formulation deposited on glass substrate previously cleaned with acetone and ethanol. In this second case, irradiation was performed at room temperature under an industrial UV conveyor using a microwave Hg arc lamp (H lamp, Fusion). The belt speed of the conveyor was set at 10 m/min and the lamp intensity at 100%. Under these conditions, for each pass, the emitted light dose

is 1.46 J/cm^2 (UVA [320–390 nm]: 0.45 J/cm^2, UVB [280–320 nm]: 0.42 J/cm^2, UVC [250–260 nm]: 0.09 J/cm^2 and UVV [395–445 nm]: 0.5 J/cm^2). Only 5 passes under the UV conveyor were performed to afford solid crosslinked films. For ene chain-growth polymerization (homopolymerization), the same procedure was repeated without including the thiol-based organosilane (**T**).

2.3. Characterization

Time-resolved infrared spectra obtained by RT-FTIR spectroscopy were recorded with a Bruker Vertex 70. The resolution of the infrared spectra was 4 cm^{-1}. Liquid film thickness prior to irradiation was determined by optical profilometry using an Altisurf 500 workstation (Altimet) equipped with a 350 µm AltiProbe optical sensor. During the UV irradiation, the absorbance decrease of the CH_3 symmetric stretching vibration band centred at 2848 cm^{-1} (distinctive from CH_3 methanol vibration modes) was monitored to follow the methoxysilyl hydrolysis in PDMOS. All spectra were baseline corrected prior to integration with the software OPUS 6.5. To obtain quantitatively reliable ^{29}Si and ^{13}C solid state NMR spectra, single pulse magic angle spinning (SPE-MAS) experiments were performed on a Bruker Avance II 400 spectrometer operating at 79.48 and 100.6 MHz respectively with a Bruker double channel 7 mm probe. Spectra were recorded using a pulse angle of π/4, a recycling delay of 80 and 60 s respectively, a spinning frequency of 4 or 5 kHz and high-power proton decoupling during the acquisition. ^{29}Si and ^{13}C chemical shifts are both relative to tetramethylsilane. Deconvolution of the spectrum was performed using Dmfit software [26]. The scratch resistance of the UV-cured coatings deposited onto glass plate was characterized at room temperature using the apparatus described in previous articles [27]. The tip was a diamond sphere of radius 96 µm, and the sliding speed was maintained constant (30 µm/s). First of all, one should note that the penetration of the spherical indenter is at least 40 times smaller than the film thickness. As a result, this latter can be considered as a semi-infinite solid. The tests were performed under a dry atmosphere (Relative Humidity <4%). Stepwise normal load ramps were performed in the range of 0.04 to 10 N. At each force step, the tip moved over a distance of 1 mm to obtain a groove that can be analyzed in terms of steady state regime. The tangential load was recorded throughout the experiment, and pictures were taken with the help of an *in situ* microscope equipped with a CCD camera. Then, the size and shape of the contacts on the coatings were analyzed through the transparent sample and substrate.

3. Results and discussion

3.1. Synthesis and characterization of thiol-ene hybrid films

Based on real-time FTIR data, Figure 2a is a conversion-time plot (SH, C=C and $OSi(OCH_3)_3$) during UV irradiation in an air environment of a **E$_1$-T** film including a stoichiometric ratio of thiol-ene functional groups. The formulation contains also 2 wt% diaryl iodonium salt photoacid generator (I250) and hydroxyphenylketone radical photoinitiator (D1173), to build-up the two silsesquioxane networks and the thioether bridges, respectively. The acid-catalyzed hydrolysis of $OSi(OCH_3)_3$ into SiOH, which precedes condensation, occurs at very fast rates achiev-

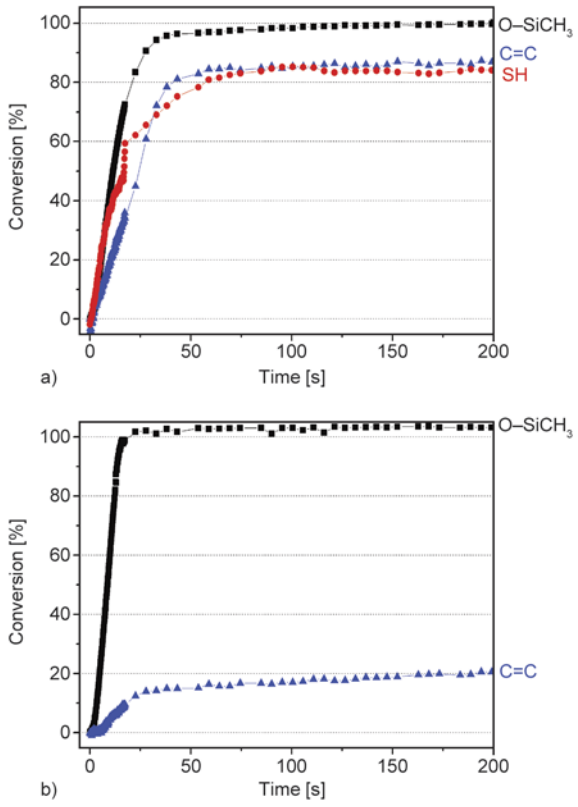

Figure 2. Temporal conversion in ene, thiol and methoxysilyl groups during the UV irradiation of **E$_1$-T** with a 1:1 thiol-ene stoichiometry (a) and **E$_1$** (b). Kinetic data were obtained from integrated absorbance in the FTIR spectra: C=C (triangle, =CH_2 bending at 1310 cm^{-1}), SH (circle, S-H stretching at 2570 cm^{-1}) SiO-CH_3 (square, CH_3 asymmetric stretching at 2848 cm^{-1}).

ing completion after 20 s exposure. In addition, there are clear indications that thiol and methacrylate are consumed concomitantly, suggesting that a thiol-ene coupling is preferentially active compared to a conventional ene homopolymerization. Low film thickness (≈4 μm) and viscosity (2–3 mPa·s at 25 °C) are both conducive to oxygen permeation to form peroxy radicals. While these species are inactive in a chain-growth radical process, they can readily abstract a hydrogen atom from a thiol to form an active thiyl radical adding to an acrylate. Therefore, a single transfer/addition thiol-ene mechanism is likely to operate under these conditions, to yield a homogenous thioether-bridged silica network as sketched in Figure 1. Furthermore, because sol-gel photopolymerization is generally under a water permeation controlled-regime [25], thin film conditions favour a fast a complete hydrolysis reaction. Under these conditions, thiol-ene reaction which takes place rapidly (<25 s), proceeds almost synchronously with hydrolysis. This latter feature is critical to ensure high conversion (85%) as an early sol-gel vitrification is likely to impede the thiol-ene coupling reaction. Conversely, a conventional chain-growth polymerization can be favored by irradiating the single precursor **E$_1$** film. In this second case, the silsesquioxane network architecture changes significantly (Figure 3). In conventional chain-growth polymerizations, each monomer is coupled to two other monomers units affording higher cross-link density in contrast to radical thiol–ene reaction in which each ene group forms only a single bond with

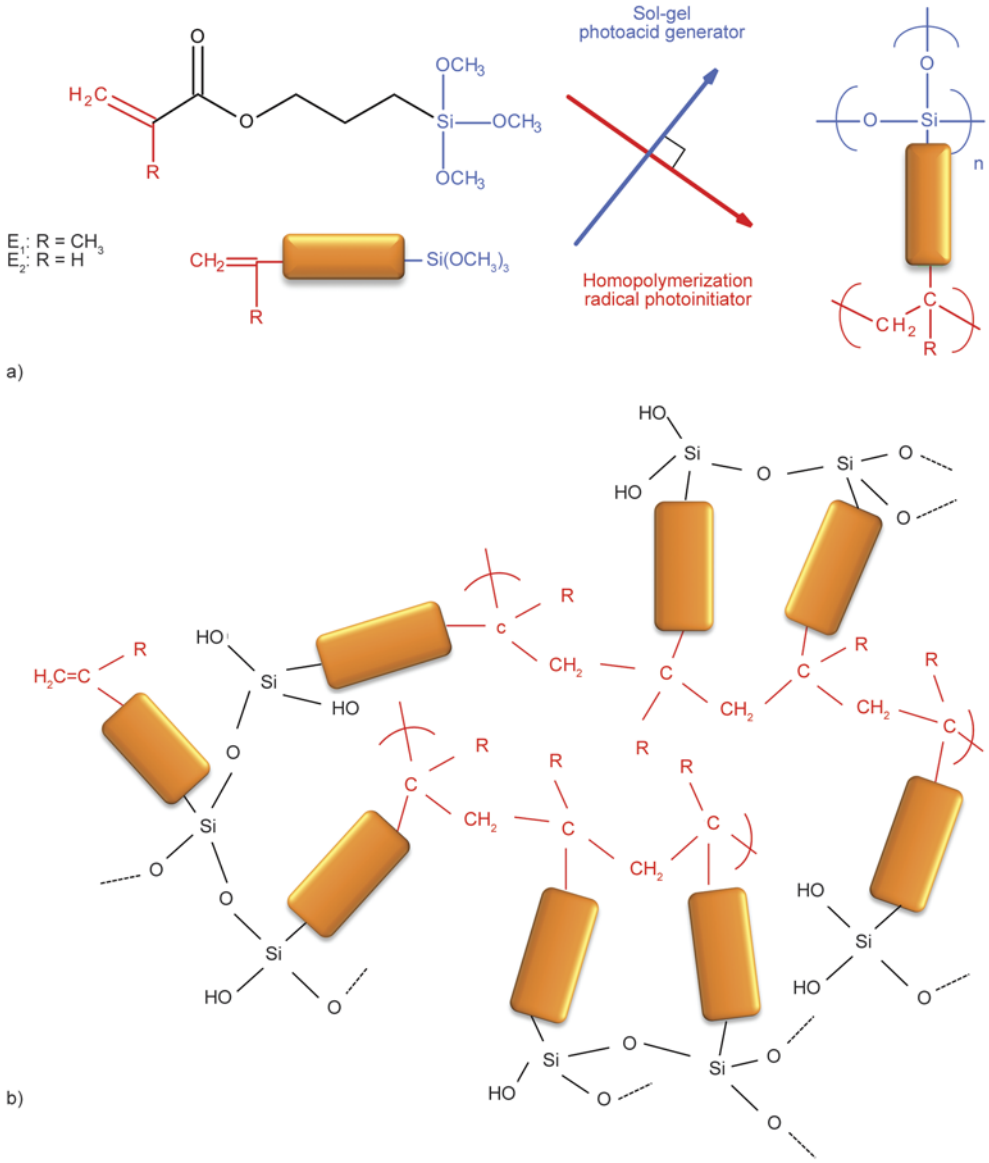

Figure 3. a) Dual ene homopolymerization and sol-gel process from precursors **E$_1$** (R = CH_3) and **E$_2$** (R = H) affording a polymer-siloxane nanocomposite structure represented in b).

another thiol. Figure 2b displays the organic-inorganic kinetic curves for the nanocomposite film derived from **E$_1$** irradiated alone. The hydrolysis rates remain unchanged with respect to the thiol-ene **E$_1$-T** mixture, whereas the consumption of the methacrylate moiety is significantly different. As expected, methacrylate homopolymerization is slower and strongly restricted by oxygen inhibition, which limits the conversion to ca. 20%. However, the resultant polymethacrylate hybrid film is tack-free.

Likewise, a thiol-ene/sol-gel tandem reaction was carried out with the **E$_2$-T** pair. Figure 4 shows some kinetic profiles very similar to the first couple (100% hydrolysis, 80% thiol-ene conversion). This suggests that this approach could accept a range of thiol- or ene-based silsesquioxane precursors. Compared with conventional routes to hybrid thiol-ene networks, a key feature of this tandem photosol-gel and photopolymerization is high reaction speed. Although the present data establish sol-gel and thiol-ene reactions as a robust orthogonal set of coupling reactions, the chemoselectivity must be mitigated by the fact that carboradicals from radical PI or thiyl radicals can be oxidized by Ph_2I^+. However, consumption of onium salt by this mechanism does not seem to affect the sol-gel progress.

Evidence of sol-gel condensation in the two nanocomposite thiol-ene films was indeed provided by ^{29}Si solid-state NMR. Figure 5 displays the quantitative ^{29}Si SPE-MAS NMR spectra of the two **E$_1$-T** and **E$_2$-T** nanocomposite films. In both systems, the broad resonances at –48, –57 and –69 ppm were straightforwardly assigned to $(XO)_2(R)Si(OSi)$ (T^1), $(XO)(R)Si(OSi)_2$ (T^2) and $(R)Si(OSi)_3$ (T^3) where R is the organic component, and X is CH_3 or H (after hydrolysis). The proportion of the different T^n is provided in the same figure. A comparable and moderate condensation degree of 81% was estimated for the two thiol-ene hybrid films, supporting the efficiency of the photoinduced sol-gel reaction despite a high thiol-ene coupling yield. We note that similar levels were achieved with the two hybrid analogues obtained from the single ene organosilane precursors: **E$_1$** (78%) and **E$_2$** (80%), although much lower ene conversion was reported in this case (<30%). Additionally, the formation of thioether bonds was investigated for the **E$_1$-T** pair by ^{13}C SPE-MAS NMR (data not given). The **–C–S–C–** connectivity was reflected by the almost disappearance of the two unsaturated carbons (120–130 ppm) from **E$_1$** and the appearance of an intense resonance at 35 ppm assigned to the two α-carbons attached to sulfur, with a chemical shift significantly different from α-carbon in thiols (25 ppm for **–C–**SH in precursor **T**).

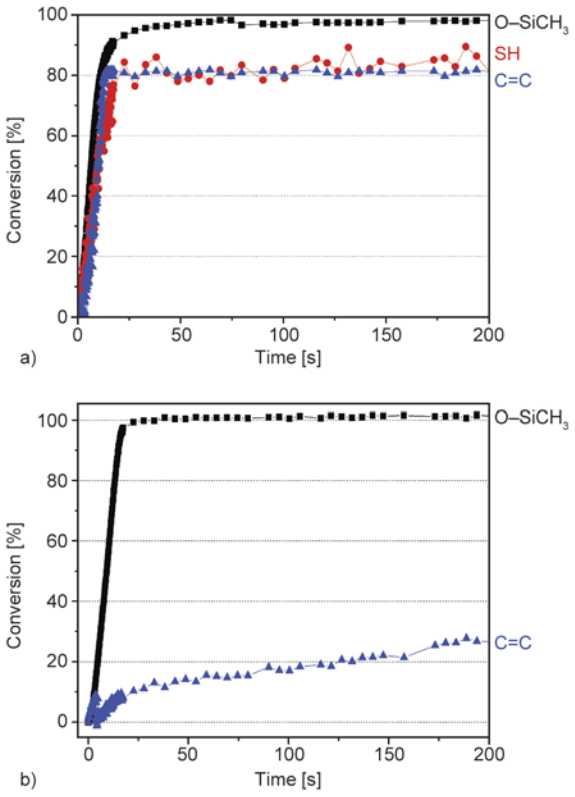

Figure 4. Temporal conversion in ene, thiol and methoxysilyl groups during the UV irradiation of **E$_2$-T** with a 1:1 thiol/ene stoichiometry (a). For comparison, kinetics of **E$_2$** homopolymerization/sol-gel reaction is given (b).

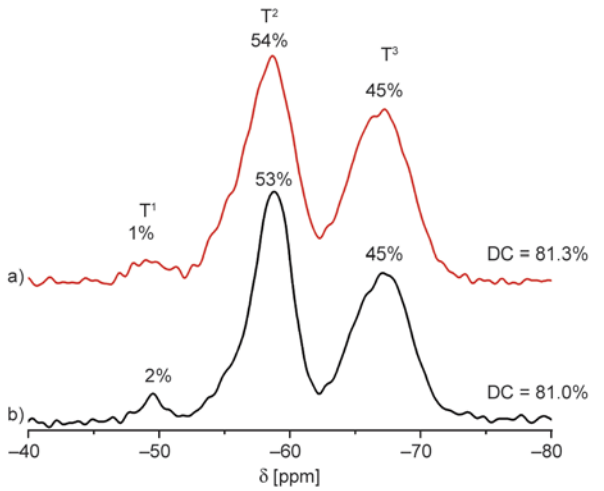

Figure 5. Solid-state ^{29}Si SPE MAS NMR spectra of UV crosslinked **E$_1$-T** (a) and **E$_2$-T** (b) thiol-ene hybrid films

3.2. Mechanical characterization

There is a vast array of work on the mechanical properties of thiol-ene networks [28–30]. However, the majority is focused on homogeneity in the network crosslink density reflected by a narrowing of the loss tangent peak measured via dynamic mechanical analysis [31]. In our case, the surface mechanical properties of the cured hybrid films have been emphasized by means of scratch tests. For the preparation of the specimens, larger surfaces (20×20 mm) were needed, and films were synthesized under a UV-conveyor (see experimental section). However, we checked that similar final conversions were obtained under these irradiation conditions. In order to evaluate the effect of thiol-ene coupling on film mechanical properties, **E_1-T** behavior was compared with **E_1** film, both having comparable inorganic content (27±2 wt%.) and level of condensation (81±2 mol%).

As described in a separate publication [27], the 'MicroVisioScratch' set-up comprises a diamond tip draining across the film under increasing stepwise load, and coupled with *in situ* optical microscope observation to study the mechanical behavior and damage mechanism which appears during scratching. Figure 6 displays a set of *in situ* photographs of the grooving tip taken during the scratch tests performed on these three films. The most relevant pictures are provided as well as the corresponding average contact pressure (i.e. the normal force contact surface ratio). For the thiol-ene hybrid film **E_1-T**, three canonical mechanical domains can be observed. Below a threshold pressure of 2058 MPa, the *elastic* regime is maintained in which the film undergoes only a reversible deformation, and there is consequently neither residual scratching track nor damage after the passage of the tip. In this domain, the lack of plasticity results in a contact area forming an undistorted disk matching exactly the spherical shape of the tip (Image **1**). Beyond 2058 MPa, appear consecutively the two usual forms of *cracking:* first *blistering* (Image **2**) with a fracture mechanism restricted to the substrate/film interface. Above 2823 MPa, *flaking* occurs (Image **3**) which reflects cohesive cracking within the film. By comparison, the film derived from single precursor **E_1** reveals no *elastic* domain but a very narrow *plastic region* (Image **1'**). In this *plastic domain*, the contact area becomes dissymmetric showing an apparent front pad and the second distinctive point is a partial recovery of the groove left on the surface (Image **2'**). For pressure greater than 115 MPa, *flak-*

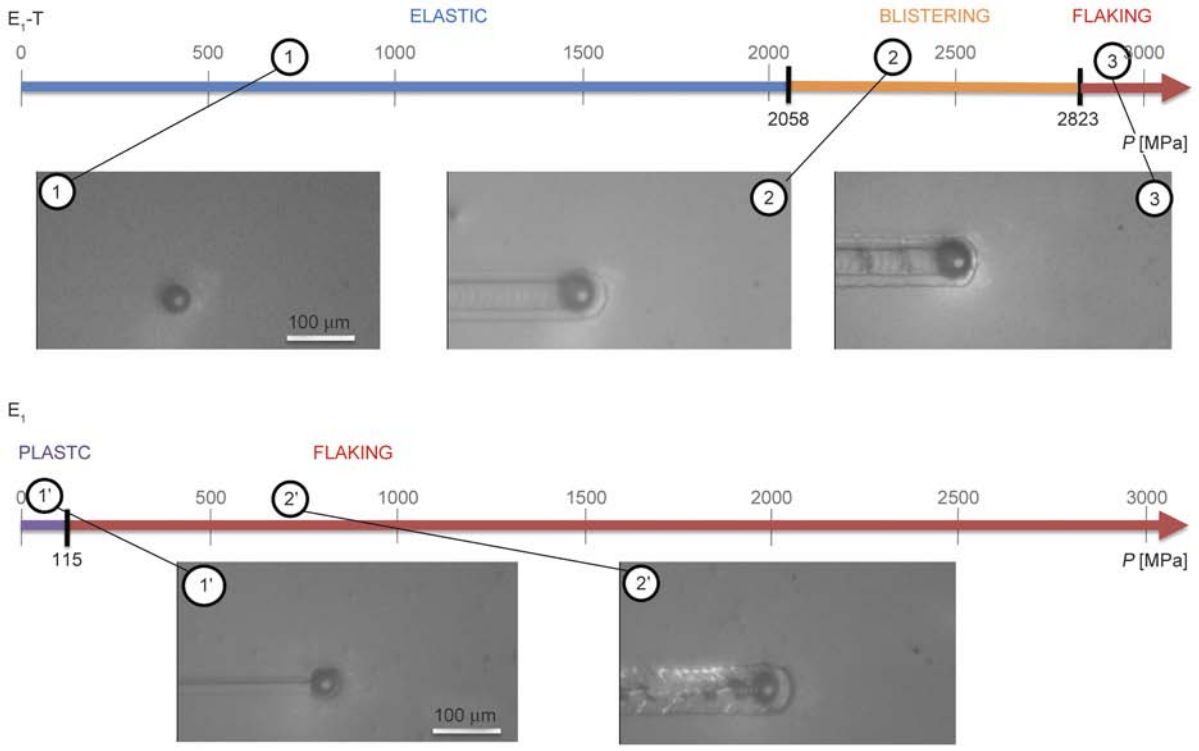

Figure 6. Difference of scratch resistance between thiol-ene coupled hybrid films (**E_1-T**) and homopolymer hybrid films (**E_1**) as a function of the average contact pressure (*P*). The different regimes (*elastic*, *blistering* and *cracking*) are reported.

ing takes place (Image **2'**). It is well-established that this critical pressure or load, generating the first damage in a scratch test, is representative of the behavior of a coating. As conclusion, this first methacrylate system (**E_1-T** *vs* **E_1**) shows thiol-ene as a very efficient approach for the formation of crosslinked materials with enhanced mechanical properties. In glassy silsesquioxane networks, the residual stress may be important and modes of dissipation are frozen out and unable to accommodate deformation without the formation of cracks. In the **E_1-T** thiol-ene system, we hypothesize that the introduction of flexible thioether bridges provides more molecular mobility and may balance the rigidity of the glassy siloxane network. While flexible connective organic groups are able to extent elasticity domain and retard cracking, rigid carbon-carbon single bonds and more crosslinked of polymethacrylate main chain (**E_1**) do not give the ability for polymer segments to move and dissipate energy deformation, thus causing mechanical failure at low loading.

The further advantage of the thiol-ene hybrid can be illustrated by varying the proportion between the two precursors: **E_1** and **T** as an easy means to modulate the proportion between ene homopolymerization and ene coupling. Where appropriate, Figure 7 shows the extent of the *elastic*, *blistering* and *flaking* domains as a function of the average contact pressure for six different hybrid films produced with different ene molar fractions: 0% (**T**), 20, 40,

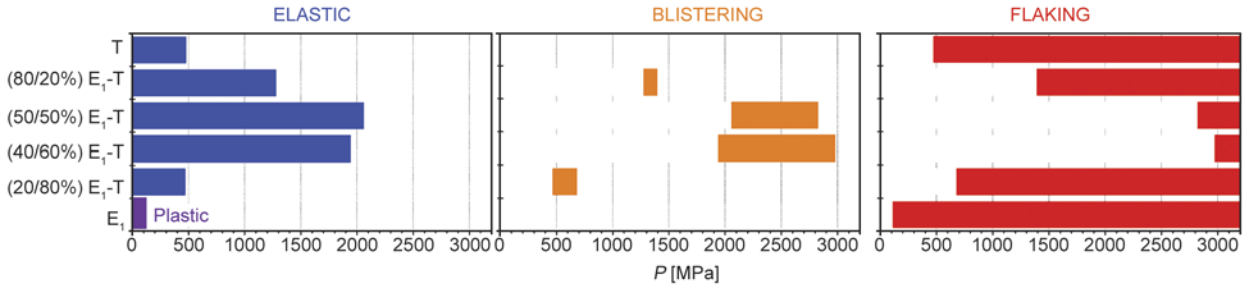

Figure 7. Effect of thiol and ene monomer proportion on *elasticity*, *blistering* and *flaking* of **E_1-T** hybrid films during scratch tests. Data are plotted as a function of the average contact pressure in MPa. (*x*/*y* [%]) **E_1-T** is associated with a hybrid film including *x* [%] of ene and *y* [%] of thiol groups.

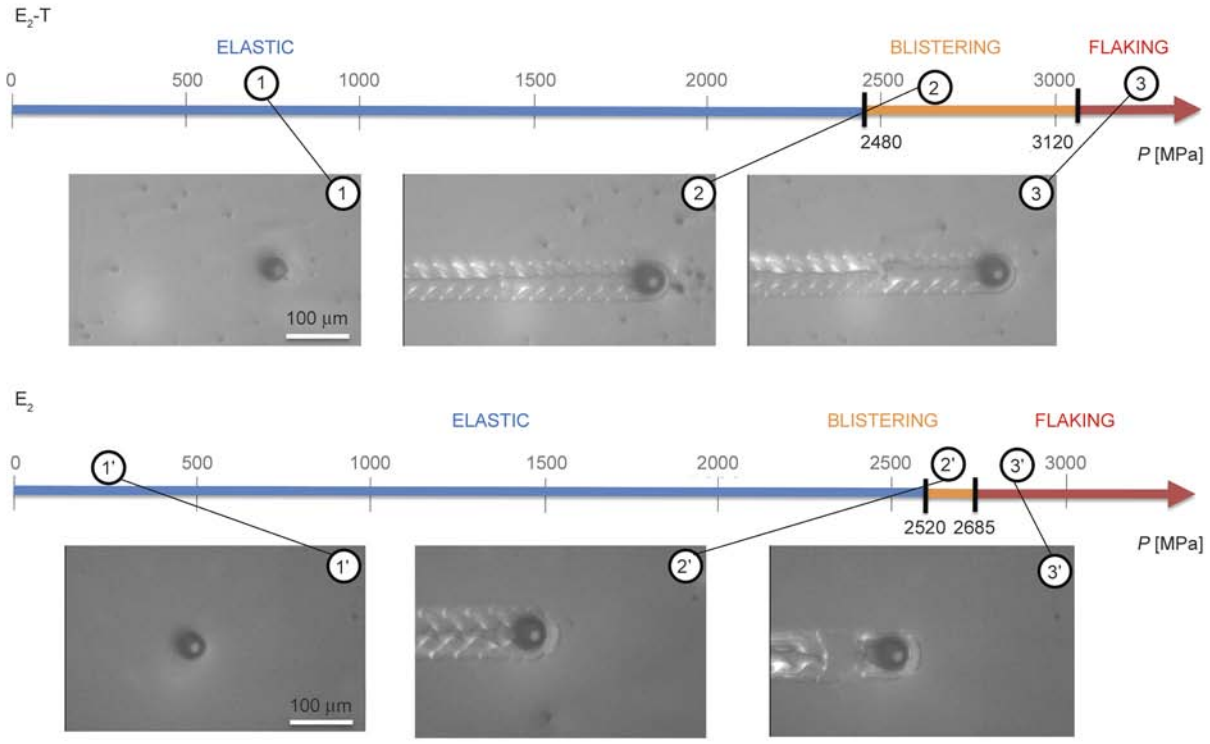

Figure 8. Difference of scratch behavior between thiol-ene hybrid films **E_2-T** and its homologue based on radical chain-growth polymerization **E_2** depending on average contact pressure (*P*)

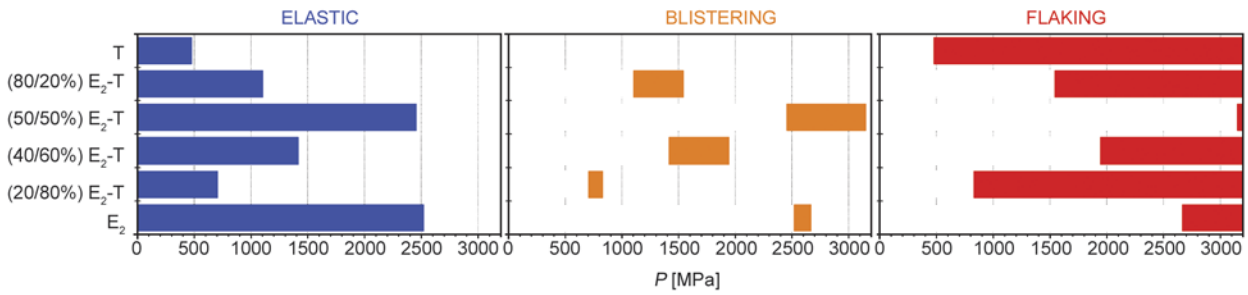

Figure 9. Extent of *elastic*, *blistering* and *flaking* domains in **E_2-T** hybrid films as a function of the thiol/ene molar proportions (*x*/*y* [mol%])

50% (**E_1-T_1**), 80 and 100 % (**E_1**). There is clearly a progressive extension of the *elastic* domain, and better resistance to cracking as the ratio of thiol and ene functions approximates 1 (**E_1-T_1**). The utility of forming thioether bridges within a silsesquioxane is thus demonstrated as a way to create a uniform, low-stress and flexible crosslinked hybrid structure. Moreover, there are clear indications that mechanical properties can be easily modulated. We see the versatility of the approach enabling to tune mechanical properties of polysulfide-crosslinked materials with varying the ratio of the two precursors.

Nevertheless, generalization of the findings of the **E_1-T** couple to other thiol-ene couples seems challenging. For example, the **E_2-T** thiol-ene film reveals somewhat similar elasticity, and cracking resistance compared to its homopolymerized homologue **E_2** (Figure 8). In this second system, we clearly see that the added value of a flexible thioether linkage is less obvious, because the polyacrylate formed in **E_2** has a much lower glass transition temperature than that of the polymethacrylate of **E_1**. This difference is attributed to stiffening of main chain of the polymer by the α-methyl substituent of the polymethacrylate. However, Figures 9 illustrates again how mechanical properties can be tailored by changing the proportion of the two precursors, with clearly the best performances achieved with the thiol-ene hybrid film having 1:1 thiol ene molar ratio.

4. Conclusions

An orthogonal coupling strategy was developed by combining thiol–ene and sol-gel photoinduced reactions, which was subsequently applied to the one-pot synthesis of uniform and low stress hybrid films. Starting from two bifunctional meth(acrylate) and thiol trimethoxysilane precursors, thiol-ene has proven to be an efficient ligation tool to bind the two resultant silsesquioxane networks together through a single coupled thioether product. In this approach the sol-gel process enables the formation of a rigid oxo-polymer siloxane network with high crosslink density, while the thiol-ene coupling imparts flexibility, thus improving elasticity and resistance to cracking of the final material. The interest of using (meth)acrylate organosilane precursors is that thiol-ene and conventional chain-growth polymerization can be combined with the ability to tailor mechanical response.

References

[1] Hoyle C. E., Lowe A. B., Bowman C. N.: Thiol-click chemistry: A multifaceted toolbox for small molecule and polymer synthesis. Chemical Society Reviews, **39**, 1355–1387 (2010).
DOI: 10.1039/b901979k

[2] Dénès F., Pichowicz M., Povie G., Renaud P.: Thiyl radicals in organic synthesis. Chemical Review, **114**, 2587–2693 (2014).
DOI: 10.1021/cr400441m

[3] Wong C-H., Zimmerman S. C.: Orthogonality in organic, polymer, and supramolecular chemistry: From Merrifield to click chemistry. Chemical Communications, **49**, 1679–1695 (2013).
DOI: 10.1039/c2cc37316e

[4] Hoyle C. E., Bowman C. N.: Thiol-ene click chemistry. Angewandte Chemie International Edition, **49**, 1540–1573 (2010).
DOI: 10.1002/anie.200903924

[5] Jasinski F., Lobry E., Tarablsi B., Chemtob A., Croutxé-Barghorn C., Le Nouen D., Criqui A.: Light-mediated thiol–ene polymerization in miniemulsion: A fast route to semicrystalline polysulfide nanoparticles. ACS Macro Letters, **3**, 958–962 (2014).
DOI: 10.1021/mz500458s

[6] DeForest C. A., Polizzotti B. D., Anseth K. S.: Sequential click reactions for synthesizing and patterning three-dimensional cell microenvironments. Nature Materials, **8**, 659–664 (2009).
DOI: 10.1038/nmat2473

[7] Stenzel M. H.: Bioconjugation using thiols: Old chemistry rediscovered to connect polymers with nature's building blocks. ACS Macro Letters, **2**, 14–18 (2013). DOI: 10.1021/mz3005814

[8] Brinker C. J., Scherer G. W.: Sol-gel science. Academic Press, San Diego (1990).

[9] Sangermano M., Colucci G., Fragale M., Rizza G.: Hybrid organic–inorganic coatings based on thiol-ene systems. Reactive and Functional Polymers, **69**, 719–723 (2009). DOI: 10.1016/j.reactfunctpolym.2009.05.008

[10] Moszner N., Schöb W., Rheinberger V.: Synthesis, characterization and thiol-ene polymerization of hydrolyzed/condensed norbornenyl silic acid ester. Polymer Bulletin, **37**, 289–295 (1996). DOI: 10.1007/bf00318060

[11] Kim J-S., Yang S., Park H., Bae B-S.: Photo-curable siloxane hybrid material fabricated by a thiol-ene reaction of sol-gel synthesized oligosiloxanes. Chemical Communications, **47**, 6051–6053 (2011). DOI: 10.1039/c1cc11297j

[12] Schreck K. M., Leung D., Bowman C. N.: Hybrid organic/inorganic thiol–ene-based photopolymerized networks. Macromolecules, **44**, 7520–7529 (2011). DOI: 10.1021/ma201695x

[13] Cole M. A., Bowman C. N.: Synthesis and characterization of thiol–ene functionalized siloxanes and evaluation of their crosslinked network properties. Journal of Polymer Science Part A: Polymer Chemistry, **50**, 4325–4333 (2012). DOI: 10.1002/pola.26245

[14] Kim J-S., Lee S., Hwang Y. H., Kim Y., Yoo S., Bae B-S.: Photo-curable sol-gel hybrid film as a dielectric layer by a thiol-ene reaction in air or N_2 for organic thin film transistors. Electrochemical and Solid-State Letters, **15**, G13–G15 (2012). DOI: 10.1149/2.021205esl

[15] Sparks B. J., Kuchera T. J., Jungman M. J., Richardson A. D., Savin D. A., Hait S., Lichtenhan J., Striegel M. F., Patton D. L.: Cyclic tetravinylsiloxanetetraols as hybrid inorganic–organic thiol-ene networks. Journal of Materials Chemistry, **22**, 3817–3824 (2012). DOI: 10.1039/c2jm15484f

[16] Igarashi Y., Kajihara K., Kanamura K.: Thiol-containing polysilsesquioxane liquid and photocurable sulfur-containing transparent organic–inorganic hybrid monoliths obtained *via* cosolvent-free hydrolytic polycondensation. Bulletin of the Chemical Society of Japan, **86**, 880–883 (2013). DOI: 10.1246/bcsj.20130053

[17] Peng S., Zeng Z., Zhao W., Li H., Chen J., Han J., Wu X.: Novel functional hybrid silica sol–gel coating for copper protection *via in situ* thiol–ene click reaction. RSC Advances, **4**, 15776–15781 (2014). DOI: 10.1039/c4ra00142g

[18] Clark T. S., Hoyle C. E., Nazarenko S.: Kinetics analysis and physical properties of photocured silicate-based thiol-ene nanocomposites: The effects of vinyl POSS ene on the polymerization kinetics and physical properties of thiol-triallyl ether networks. Journal of Coatings Technology and Research, **5**, 345–351 (2008). DOI: 10.1007/s11998-008-9092-x

[19] Li L., Liang R., Li Y., Liu H., Feng S.: Hybrid thiol–ene network nanocomposites based on multi(meth)acrylate POSS. Journal of Colloid and Interface Science, **406**, 30–36 (2013). DOI: 10.1016/j.jcis.2013.05.044

[20] Sangermano M., Gross S., Priola A., Rizza G., Sada C.: Thiol-ene hybrid organic/inorganic nanostructured coatings based on thiol-functionalized zirconium oxoclusters. Macromolecular Chemistry and Physics, **208**, 2560–2568 (2007). DOI: 10.1002/macp.200700323

[21] Esposito Corcione C., Striani R., Frigione M.: Sunlight curable hybrid organic–inorganic methacrylic-based coatings: Analysis of the cure mechanism and functional properties. Polymers for Advanced Technologies, **26**, 167–175 (2015). DOI: 10.1002/pat.3445

[22] Lowe A. B.: Thiol–ene 'click' reactions and recent applications in polymer and materials synthesis: A first update. Polymer Chemistry, **5**, 4820–4870 (2014). DOI: 10.1039/c4py00339j

[23] Bhagat S. D., Chatterjee J., Chen B., Stiegman A. E.: High refractive index polymers based on thiol–ene cross-linking using polarizable inorganic/organic monomers. Macromolecules, **45**, 1174–1181 (2012). DOI: 10.1021/ma202467a

[24] Chemtob A., Versace D-L., Belon C., Croutxé-Barghorn C., Rigolet S.: Concomitant organic-inorganic UV-curing catalyzed by photoacids. Macromolecules, **41**, 7390–7398 (2008). DOI: 10.1021/ma801017k

[25] De Paz H., Chemtob A., Croutxé-Barghorn C., Le Nouen S., Rigolet S.: Insights into photoinduced sol–gel polymerization: An *in situ* infrared spectroscopy study. Journal of Physical Chemistry B, **116**, 5260–5268 (2012). DOI: 10.1021/jp212386e

[26] Massiot D.: Sensitivity and lineshape improvements of MQ-MAS by rotor-synchronized data acquisition. Journal of Magnetic Resonance, Series A, **122**, 240–244 (1996). DOI: 10.1006/jmra.1996.0202

[27] Le Houérou V., Gauthier C., Schirrer R.: Mechanical analysis of the blistering of a thin film deposited on a glassy polymer. Tribology International, **43**, 129–135 (2010). DOI: 10.1016/j.triboint.2009.05.011

[28] Kasprzak S. E., Martin B., Raj T., Gall K.: Synthesis and thermomechanical behavior of (qua)ternary thiol-ene(/acrylate) copolymers. Polymer, **50**, 5549–5558 (2009).
DOI: 10.1016/j.polymer.2009.09.044

[29] McNair O. D., Janisse A. P., Krzeminski D. E., Brent D. E., Gould T. E., Rawlins J. W., Savin D. A.: Impact properties of thiol–ene networks. ACS Applied Materials and Interfaces, **5**, 11004–11013 (2013).
DOI: 10.1021/am403238g

[30] An S. Y., Lee D. G., Hwang J. W., Kim K. N., Nam J. H., Jung H. W., Noh S. M., Oh J. K.: Photo-induced thiol-ene polysulfide-crosslinked materials with tunable thermal and mechanical properties. Journal of Polymer Science Part A: Polymer Chemistry, **52**, 3060–3068 (2014).
DOI: 10.1002/pola.27353

[31] Senyurt A. F., Wei H., Phillips B., Cole M., Nazarenko S., Hoyle C. E., Piland S. G., Gould T. E.: Physical and mechanical properties of photopolymerized thiol–ene/acrylates. Macromolecules, **39**, 6315–6317 (2006).
DOI: 10.1021/ma060507f

eXPRESS Polymer Letters Vol.10, No.6 (2016) 450–461
Available online at www.expresspolymlett.com
DOI: 10.3144/expresspolymlett.2016.43

Electroactive polyurea/CNT composite-based electrode for detection of vitamin C

T. C. Huang[1], L. C. Yeh[2] , G. H. Lai[1], F. Y. Lai[1], T. I. Yang[3], Y. J. Huang[4], A. Y. Lo[1], J. M. Yeh[2]*

[1]Department of Chemical and Materials Engineering, National Chin-Yi University of Technology, 41170 Taichung, Taiwan, R. O. C.
[2]Department of Chemistry, Chung Yuan Christian University, 32023 Chung Li,Taiwan, R. O. C.
[3]Department of Chemical Engineering, Chung Yuan Christian University, 32023 Chung Li, Taiwan, R. O. C.
[4]Cellular and Behavioral Neuroscience, Texas A&M University, College Station, TX 77843, United States

Received 7 October 2015; accepted in revised form 27 December 2015

Abstract. The electrocatalytic oxidation of vitamin C at carbon paste electrode (CPE) modified with amino-functionalized multiwalled carbon nanotube/electroactive polyurea (AF-MWCNT/EPU) composite was investigated. We have synthesized novel electroactive polyurea composites containing MWCNTs functionalized with 4-aminobenzoyl groups by an oxidative coupling polymerization. Ultraviolet-Visible spectra and cyclic voltammetry studies confirmed the occurrence of efficient interaction between AF-MWCNT and EPU graft. Moreover, the electrocatalytic activity of vitamin C oxidation by utilizing aniline containing composites was evaluated, showing that the intrinsic electroactivity of AF-MWCNT/EPU-CPE had great potential application for detection of vitamin C. The detection limit and sensitivity of this sensor was 1.2 μM and 35.3 $\mu A \cdot mM^{-1}$, respectively.

Keywords: *polymer composites, electroactive polyurea, sensor, nanocomposites*

1. Introduction

Since their discovery in the 1950s, conducting polymers have been extensively studied and showed great promise in a variety of applications [1–7]. Among various conducting polymers, polyaniline (PANI) has attracted much attention due to its ease of synthesis, unique and controllable chemical, electrical properties and long-term stability in air. However, the PANI synthesized by chemical and electrochemical methods shows low solubility in common solvents. In addition, few synthesized PANIs have defined structures and precise oxidation-reduction states [8], which make it difficult to understand the electron transport mechanisms in PANI. For these reasons, aniline oligomers can be considered as good model compounds for researching specific behaviours of PANI [9]. Faul *et al*. [10] synthesized (tetra) aniline-alkyl diblock compounds which self-assembled into single-crystalline two dimensional microplates and further studied their conductivity property. Moreover, electroactive polymers incorporated with aniline oligomers have attracted research attention because of their superior properties such as good solvent solubility, mechanical strength, and the biodegradable properties [11, 12]. Other authors synthesized a series of electroactive polymers and studied their electrochromic behavior [13–15]. The multicolor of electroactive polymers could be controlled by changing pH values or the applied potential. Furthermore, a series of electroactive block copolymers with bioactive properties have also been synthesized [16, 17]. The conductivity of electroactive polymer could stimulate cell growth, especially in neural or cardiovascular cells, which are sen-

*Corresponding author, e-mail: juiming@cycu.edu.tw

sitive to electrical signals. Hardy *et al*. [18] synthesized electroactive polystyrene (EPS) and doped it using various acids. Experimental results exhibited that the dielectric properties of EPS doped with large, organic acids resulted in increases of up to an order of magnitude in permittivity and energy storage density relative to pure polystyrene, while maintaining a relatively low dielectric loss, especially in the high frequency range. Yeh and coworkers prepared many electroactive polymers such as electroactive polyimide [19], electroactive epoxy [20], electroactive polyamide [21, 22], electroactive polyurea [23] and electroactive poly(azine-azo) [24] as anticorrosion coating materials and photoactive materials. Recently, many researchers utilized electroactive polymers serving as sensing materials. The unique properties including acid-base doping/dedoping chemistry and redox behaviours make the electroactive polymers to be the potential candidates as chemical and fluorescent sensors [25–27].

Carbon nanotubes (CNTs) have attracted great attention in research since its discovery by Iijima [28] due to its unique physical and chemical properties, such as high mechanical strength, electrical, thermal stability and chemical stability [29]. CNTs are found mainly in two types: single walled carbon nanotubes and multi walled carbon nanotubes. Their characterization and properties have been comprehensively studied in the last two decades [30]. Recently, CNTs has been used as a filler to incorporate within the polymer matrix. The CNTs/polymer composites exhibit improved mechanical property, good barrier property and excellent electrical conductivity [28–33]. Many reports in literature suggest that CNTs/conducting polymer composites have great potential for use in vitamin C sensors [34, 35]. Vitamin C, an essential nutrient for human and certain animal species, is crucial for a range of metabolic reactions such as growth and tissue repair. It is also an antioxidant that prevents cell damage caused by free radicals [36].

In this study, vitamin C sensors were fabricated using hybrid materials that incorporated electroactive polyurea (EPU) covalently attached to amino-functionalized multiwalled carbon nanotubes (AF-MWCNTs) to improve the sensitivity and detection limit of obtained sensors. The as-prepared AF-MWCNTs are expected to provide reactive sites for obtaining co-oligomers by polymerization and hence improve the electrical conductivity of EPU. The ultraviolet-visible (UV-Vis) spectra revealed that the aniline oligomer segment on the EPU was able to interact with AF-MWCNTs. The results of the cyclic voltammetry (CV) studies indicated that AF-MWCNTs can enhance the current value of the AF-MWCNT/EPU composites. Most importantly, the electrical conductivity of the AF-MWCNT/EPU composites reached a value of $4.31 \cdot 10^{-3}$ S/cm at a MWCNT loading of 10 wt% in the composites, which was an increase of more than five orders of magnitude compared to the conductivity value of the neat EPU. The high conductivity and facilitation of the charge transfer processes between the AF-MWCNT and EPU significantly enhanced the sensitivity and the detection limit of the AF-MWCNT/EPU-CPE sensor for detecting vitamin C.

2. Experimental

2.1. Materials and instrumentation

N-Phenyl-p-phenylenediamine (NPPD, 98%, Aldrich), hexamethylene diisocyanate (HDI, 98%, Alfa), *p*-phenylenediamine (99%, Aldrich), Polyphosphoric acid (PPA, 83%, P_2O_5 assay), P_2O_5 (98%, Aldrich), 4-aminobenzoic acid (4-ABAD, 99%, Aldrich), ammonium persulfate (APS, 98%, Merck), tetrahydrofuran (THF, 99 , Merck), N,N-Dimethylacetamide (DMAc, 99%, Merck), N-methyl-2-pyrrolidone (NMP, 99%, Merck), L-ascorbic acid (vitamin C, reagent grade, Aldrich), phosphate buffered saline (PBS, Aldrich), hydrochloric acid (HCl, 37%, Riedel-deHaën), pristine MWCNTs (99.5%, P-MWCNTs, Golden Innovation Business Co., Ltd.), and acetone (99 , Acros) were used as received without further purification. All the chemicals used were reagent grade, unless stated otherwise. X-ray photoelectron spectroscopy (XPS, Kratos Axis Ultra DLD) was used to characterize the extent of functionalization on the surface of the MWCNTs. Fourier Transform Infrared (FTIR) spectra were collected at room temperature (on a Jasco FTIR-4100 spectrometer) from samples prepared as pellets with KBr. Mass spectrometry was carried out on a mass spectrometer (Bruker Daltonics IT, model: Esquire 2000, Leipzig, Germany) equipped with an electrospray ionization (ESI) source (Agilent, model: G1607-6001). The chemical structure of the oligoaniline was determined by ^{1}H nuclear magnetic resonance (^{1}H NMR) spectroscopy (on a Bruker 400 spectrometer), using deuterated dimethyl sulfoxide (d_6-DMSO) as the solvent. Samples were also

characterized with UV-Vis absorption spectroscopy (using Jasco V-650 spectrometer). Electroactive properties of the resulting composites were obtained using VoltaLab 21 with three-electrode electrochemical cell in a double-wall jacketed cell. Structural characterization was carried out with transmission electron microscopy (TEM on a JEOL 200FX, acceleration voltage: 120 kV). Conductivity values of the AF-MWCNT/EPU composites were obtained with a four-point probe connected to a Keithley 2400 voltmeter constant-current source system.

2.2. Functionalization of MWCNTs (AF-MWCNTs)

The AF-MWCNTs were synthesized according to the procedure reported in literature [37, 38]. 4-ABAD (10.0 g), MWCNTs (5.0 g), PPA (300.0 g), and P_2O_5 (75.0 g) were mixed using a mechanical stirrer under nitrogen atmosphere. The mixture was heated to 100 °C and allowed to react for 1 h at this temperature. Subsequently, the temperature was increased to 130 °C and the mixture was maintained at this temperature for 72 h under nitrogen atmosphere. Then, water was used to precipitate the dark homogeneous mixture. The precipitates were washed with water and methanol in a Soxhlet extractor. Subsequently, the samples were freeze-dried for 48 h to obtain the final product (7.84 g) as a dark black powder (with a yield of 52.3%).

2.3. Synthesis of EPU and AF-MWCNT/ EPU composites

2.3.1. Synthesis of co-oligomer

HDI (0.84 g, 5 mmol) was dissolved in 10 mL of THF. The resulting solution was added into a solution containing 1.84 g (10 mmol) of NPPD dissolved in 10 mL of THF over a period of 30 min. The resulting solution was stirred for 3 h and then the co-oligomer was precipitated using 200 mL of distilled water. The precipitated co-oligomer was washed with distilled water and dichloromethane and dried under dynamic vacuum at room temperature (25 °C). The as-prepared co-oligomer was obtained in a yield of ca. 90%. ^{1}H NMR (d_6-DMSO): δ = 8.18 (s, 2H, due to H_5), δ = 7.85 (s, 2H, due to H_8), δ = 7.27–7.23 (d, 4H, due to H_6), δ = 7.17–7.12 (t, 4H, due to H_{10}), δ = 6.98–6.90 (t, 8H, due to H_7, H_9), δ = 6.73–6.67 (t, 2H, due to H_{11}), δ = 6.05–5.97 (t, 2H, due to H_4), δ = 3.12–2.98 (d, 4H, due to H_3), δ =1.50–1.20 (8H, due to H_1, H_2).

2.3.2. Synthesis of EPU

EPU was prepared by simultaneously dissolving 0.536 g (1 mmol) of co-oligomer and 0.108 g (1 mmol) of 1,4-phenylenediamine into 30 mL of a stirring solution that contained 25 mL of NMP, 2.5 mL of distilled water, and 2.5 mL of concentrated hydrochloric acid. Subsequently, a solution containing 0.457 g of APS and 2 mL of 1.0 M aqueous HCl was added dropwise while stirring at room temperature. A black product was then precipitated by pouring the obtained solution into 300 mL of distilled water with continuous stirring for 12 h. The mixture was filtered and washed with distilled water and acetone several times. The dedoped state of EPU was achieved by dispersing into a 1.0 M aqueous ammonium hydroxide and stirred for 1 h. The as-obtained product was then dried under dynamic vacuum at 40 °C for 24 h.

2.3.3. Synthesis of AF-MWCNT/ EPU composites

The AF-MWCNTs were dispersed in 10 mL of NMP and ultrasonicated for 1 h. In addition, 1.07 g (2 mmol) of co-oligomer and 0.216 g (2 mmol) of *p*-phenylenediamine were dissolved in 25 mL of a solvent mixture containing 20 mL of NMP, 2.5 mL of distilled water, and 2.5 mL of concentrated HCl. Subsequently, the dispersion and the solution were mixed. A solution containing 0.913 g of APS and 5 mL of 1.0 M aqueous HCl was added dropwise into the above-prepared solution under stirring at room temperature. The resulting solution was allowed to react for 12 h. Then, the reaction mixture was dispensed into 300 mL of distilled water to precipitate the product. The dedoped state of composites was achieved by dispersing into a 1.0 M aqueous ammonium hydroxide and stirred for 1 h. The product was washed several times with distilled water and dried under vacuum at 40 °C.

2.4. Measurement of electrical conductivity

The EPU and AF-MWCNT/EPU samples were doped by immersing in 1 M HCl at room temperature for 24 h. The samples were collected by filtration, washed with distilled water, and freeze-dried for 48 h. The samples for the conductivity measurement were obtained by applying a pressure of $3.0 \cdot 10^3$ psi (20.96 mPa) to the EPU or AF-MWCNT/EPU samples to form a 0.1 cm thick pellet with a diameter of 1.3 cm.

2.5. Preparation of the CPE and modified CPE

The unmodified CPE was prepared by thoroughly mixing 30 mg of paraffin oil with 150 mg of graphite in a mortar to form a homogeneous carbon paste. A portion of the carbon paste was filled firmly into one end of a Teflon tube (of about 3.0 mm in diameter) and a copper wire was inserted through the opposite end to establish an electrical contact. Sufficient packing was achieved by pressing the surface of the samples at the end of the Teflon tube against a bond paper until a smooth surface was obtained. The modified CPEs were mixed with the 30 mg of paraffin oil, 150 mg of graphite, and 7.5 mg of each sample (EPU and AF-MWCNT/EPU) to form a homogeneous paste into the Teflon tube. The total mass of graphite and sample was set to 30 mg.

2.6. CV studies of the EPU and AF-MWCNT/EPU CPE

To study the redox behavior of EPU and AF-MWCNT/EPU, two representative CPEs were examined systematically by CV in 100 mL of 1.0 M H_2SO_4 and the potential ranging from –0.2 to 1.0 V.

3. Results and discussion

3.1. Characterization of AF-MWCNTs

AF-MWCNTs decorated with 4-aminobenzoyl moieties can act as reactive sites to graft aniline oligomers by oxidative coupling polymerization according to the reports in literature [37]. FTIR and XPS measurements were used to confirm the attachment of 4-aminobenzoyl moieties on the surface of the P-MWCNTs. As shown in Figure 1b, P-MWCNTs exhibited featureless FTIR spectrum. Nevertheless, there are clear differences of the spectrum between P-MWCNTs and AF-MWCNTs. The spectrum of AF-MWCNTs exhibits an clearly aromatic carbonyl (C=O) peak at 1640 cm^{-1}, which was shifted from the carbonyl peak of carboxylic acid at 1666 cm^{-1} in 4-ABAD. This result may indicate the 4-aminobenzoyl moieties on the AF-MWCN structure.

XPS spectra of P-MWCNTs and AF-MWCNTs were shown in Figure 2. Surface elemental composition of pristine and AF-MWCNTs were analyzed by XPS, which is one of the best surface analytical techniques, providing useful information on the nature of the functional groups and also the defects on the surface of the sample. Figure 2a showed a significant increased intensity of the O1s peak and N1s peak in AF-MWCNTs as compared to the P-MWCNT samples. The increased intensity of these peaks could be attributed to the grafting reaction with 4-ABAD. The de-convoluted C1s peak of the MWCNTs showed a major C1s peak occurring at 284.4 eV and a minor peak occurring at 285.2 eV (Figure 2b). The former peak was assigned to the sp^2 carbon atoms of the graphene sheets, and the latter peak was ascribed to the defects on the CNT walls [39]. As shown in Figure 2c, in the case of AF-MWCNTs, the XPS spectrum showed new peaks occurring at 285.6 and 287.2 eV correspond to carbon in C–NH_2 and >C=O, respectively [40, 41]. The presence of these peaks confirms the 4-aminobenzoyl moieties on the side walls of the AF-MWCNTs.

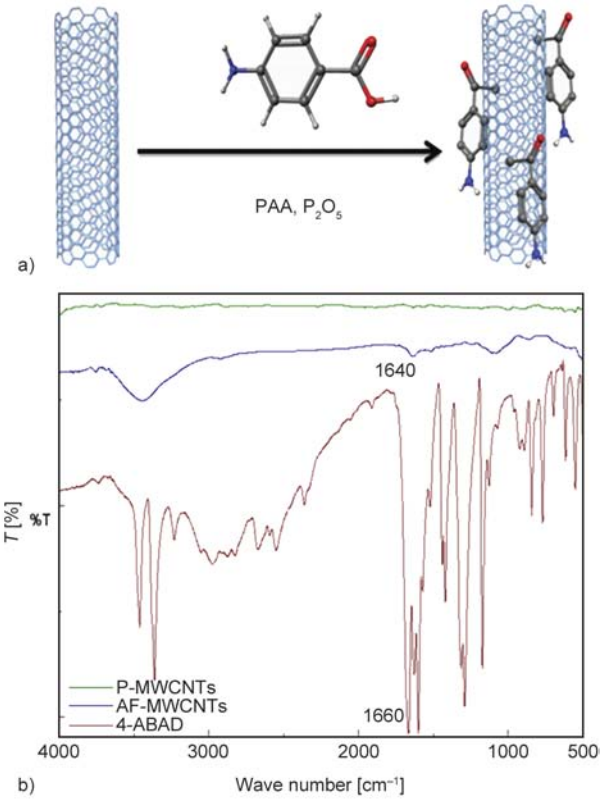

Figure 1. (a) Functionalization of MWCNTs by using 4-ABAD to obtain AF-MWCNTs. (b) Representative FTIR spectra of P-MWCNTs, AF-MWCNTs, and 4-ABAD.

3.2. Characterization of co-oligomer and EPU

The synthesis routes for the preparation of co-oligomer, EPU and AF-MWCNT/EPU composites were shown in Figure 3. The mass spectrum and 2D ^1H–^1H correlation spectroscopy (cosy) spectrum of the co-oligomer were shown in Figurr 4. In Figure 4a, the mass to charge ratio (*m*/*e*) for $C_{32}H_{36}N_6O_2$ was 536.7. Found 535.7 $(M–H)^+$. Figure 4b showed the ^1H–^1H cosy spectrum confirming the structure of

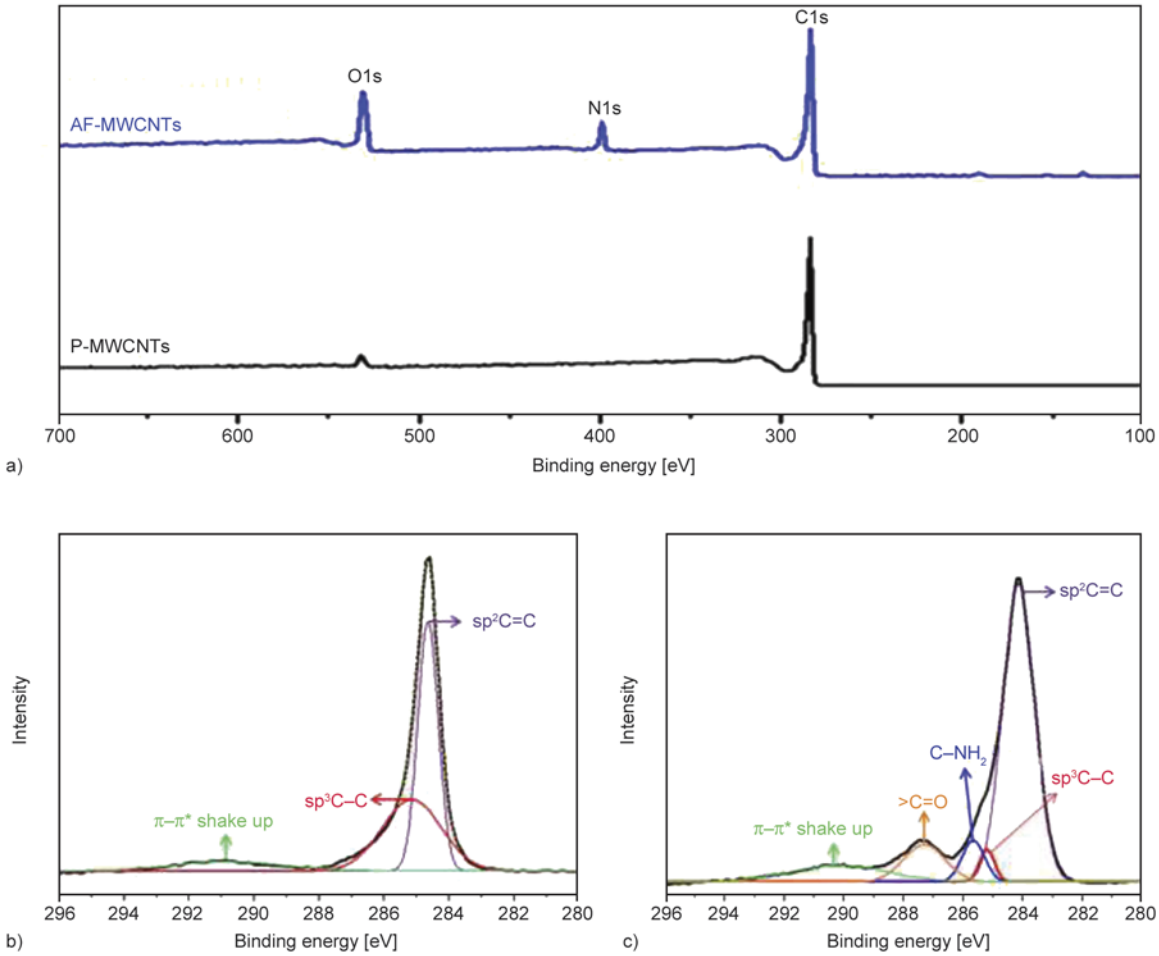

Figure 2. (a) Wide scan profiles of P-MWCNTs and AF-MWCNTs by XPS analysis. Curve fitting of C1s peaks originating from (b) P-MWCNTs and (c) AF-MWCNTs.

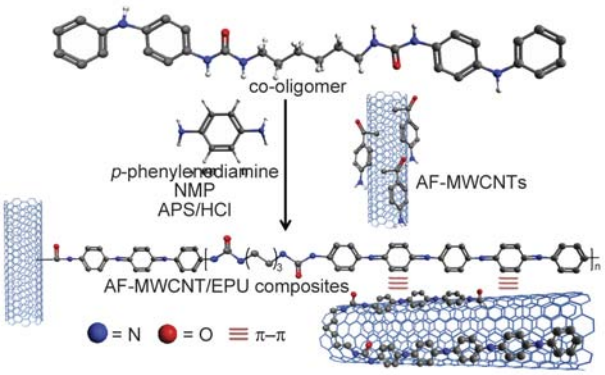

Figure 3. Synthesis route of the AF-MWCNT/EPU composites

the co-oligomer. The signals at 8.17, 7.38, and 6.03–5.99 ppm can be assigned to the amino protons and the signals at 7.27–7.24, 7.17–7.12, 6.97–6.91, and 6.72–6.67 ppm were attributed to the aromatic protons in the co-oligomer, and the signals at 3.07–3.05 and 1.42–1.30 ppm were due to the alkyl protons.

3.3. Characterization by UV-Vis spectroscopy

The UV-Vis absorption spectra of EPU and AF-MWCNT/EPU in NMP solution were utilized to examine the interaction between the electroactive polyurea and AF-MWCNT, as shown in Figure 5. The EPU showed two distinctive absorption bands at 300 and 593 nm. The peak at 300 nm can be assigned to the π-π* transition of the benzenoid rings and the peak at 593 nm can be attributed to the π-π* transition of the quinoid rings along the backbone of the EPU chain. In contrast, the characteristic peak assigned to the π-π* transition band of the benzenoid rinds showed a blue shift from 300 nm for pure EPU to 296 nm for the AF-MWCNT/EPU composites. Moreover, the intensity of the peaks related to the π-π* transition of the quinoid rings was reduced in the AF-MWCNT/EPU solution. This is because the quinoid units were stabilized by the strong π-π interaction between MWCNTs and EPU and the charge transfer from the polymer chain to MWCNTs [42, 43].

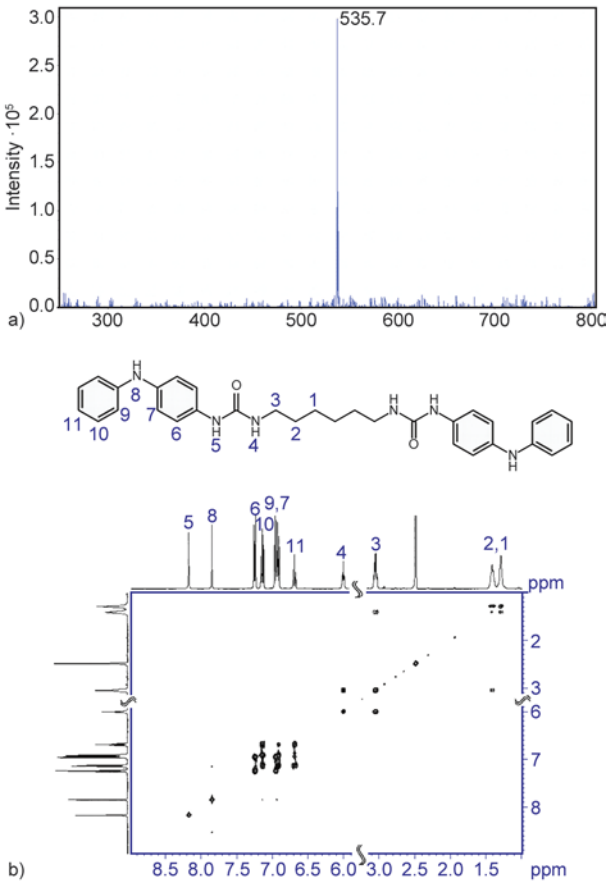

Figure 4. (a) Mass spectrum and (b) ^{1}H–^{1}H cosy spectrum of co-oligomer

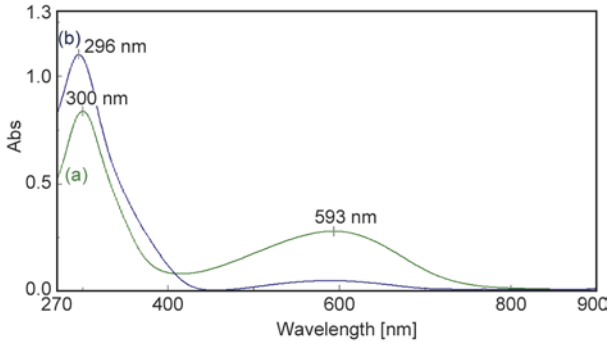

Figure 5. UV-Vis absorption spectra of (a) EPU and (b) AF-MWCNT/EPU composites

3.4. TEM characterization

TEM images were used as a tool to confirm that EPU caused the change of the morphology on carbon nanotube surface and that the AF-MWCNT surface remained intact during the preparation of the AF-MWCNT/EPU composites. For preparing the TEM sample, AF-MWCNT/EPU composites was dispersed and ultrasonicated in water for 1 h. Subsequently, AF-MWCNT/EPU solution was then dropped on the copper grid and dried at room temperature. The surface of AF-MWCNTs is smooth, indicating that the surface of the MWCNT was intact after modification, as shown in Figure 6a. In contrast, the surface of AF-MWCNT/EPU was not smooth anymore, which can be attributed to the presence of the electroactive polymers on its surface, as shown in Figure 6b. These results confirmed that the AF-MWCNTs can be covered with EPU or other electroactive polymers by utilizing the oxidative coupling reaction [44].

3.5. Conductivity measurement

The conductivity of aniline-based electroactive polymers is lower than PANI, ranging between 10^{-7} to 10^{-4} S/cm [38]. This is because that the aniline oligomers incorporated with nonconducting component to form electroactive polymers and there was little opportunity for the aniline oligomers to establish a channel for electron transport, leading to the low conductivities of the electroactive polymers. In

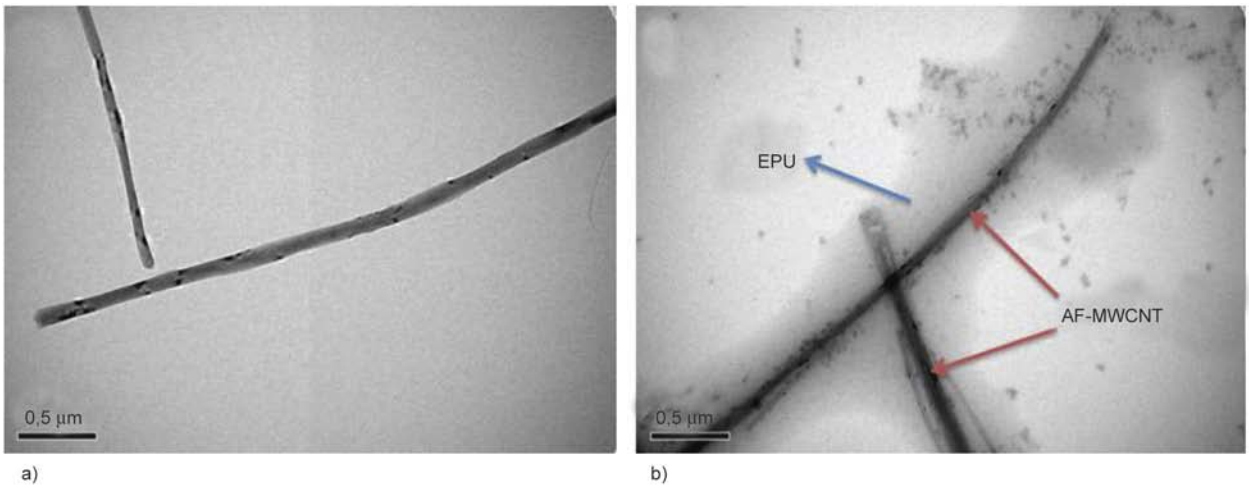

Figure 6. TEM images of (a) AF-MWCNTs and (b) nanotubes present in the AF-MWCNT/EPU composites

Table 1. The conductivity of AF-MWCNT/EPU

AF-MWCNTs Loading [wt%]	Conductivity [S/cm]
0	$4.78 \cdot 10^{-8}$
1	$7.19 \cdot 10^{-7}$
3	$3.70 \cdot 10^{-6}$
5	$2.36 \cdot 10^{-5}$
10	$4.31 \cdot 10^{-3}$
15	$9.23 \cdot 10^{-3}$

this study, we utilized AF-MWCNTs to improve the conductivity of the electroactive polymer. The electrical conductivity of AF/MWCNT/EPU composites increased five orders from $4.78 \cdot 10^{-8}$ to $4.31 \cdot 10^{-3}$ S/cm with increasing the amount of AF-MWCNTs from 0 to 10 wt% (Table 1). This result can be explained by the dopant effect, which involves an efficient charge transfer from the quinoid unit of EPU to AF-MWCNTs. CNTs are relatively good electron acceptors [45], while aniline oligomers in the EPU main chain could be considered as good electron donors. This donor-acceptor combination in the composites facilitates electron transfer, owing to the reduction of the energy barrier for electron transfer to occur from the valence band to the conduction band [46]. Therefore, the conductivity of the resulting AF-MWCNT/EPU composites could be significantly improved by introducing AF-MWCNTs into the EPU matrix.

3.6. CV studies

Figure 7 (a) showed the CV of the EPU and AF-MWCNT/EPU composites. Both EPU and AF-MWCNT/EPU composites showed three distinct pairs of redox peaks. The CV results could be attributed to the change of molecular structure of EPU. Three redox pairs originate from the transitions between Leucoemeraldine to Emeraldine I, Emeraldine I to Emeraldine II and Emeraldine II to Pernigraniline of the aniline oligomer in the main chain of EPU. Furthermore, with the MWCNTs acting as electrically conductive bridges inside the AF-MWCNT/EPU composite, the diffusion length of the electrolyte ions was greatly reduced, resulting in an enhanced current compared to that of the neat electroactive polymers [45]. The CV responses for the AF-MWCNT/EPU-CPE were recorded at different scan rates ranging from 25 to 200 mV/s, as shown in Figure 7b. As higher scan rates were applied, the oxidative peak potentials shifted to positive potential, and the reductive peak potentials shifted toward negative potential. Moreover, linear relationships between the peak currents and the square root of the scan rates with a square of regression coefficient (R^2) of 0.99 for the sensor were observed, indicating that the electron transfer process of the electrode was a diffusion-controlled process [47].

3.7. Electrochemical response of AF-MWCNT/EPU-CPE toward vitamin C

The prepared AF-MWCNT/EPU-CPE exhibited the current responses toward vitamin C as shown in Figure 8. Moreover, the oxidation current which occurred at 0.40 V versus Ag/AgCl would continuously increase with increasing concentration of vitamin C from 0.0 to 8.0 mM. This result indicated that the aniline oligomer in AF-MWCNT/EPU-CPE has direct electrocatalytic properties to the oxidation of vitamin C. The redox reaction process could be described by the following steps. Vitamin C in the solution diffused toward the polymer modified elec-

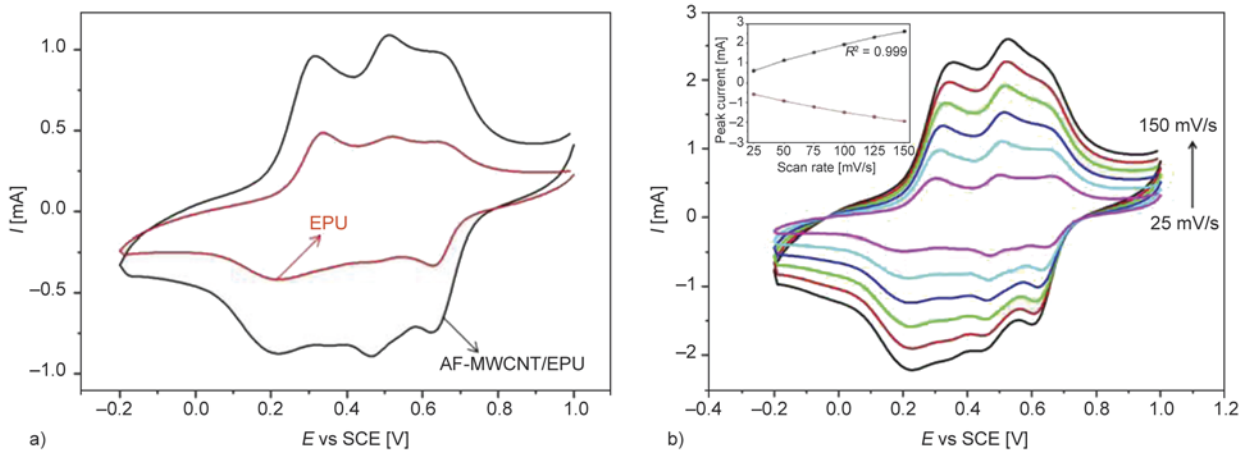

Figure 7. CV curves of (a) EPU and AF-MWCNT/EPU CPE and (b) AF-MWCNT/EPU-CPE in 1 M H_2SO_4 at different potential scan rates: 25, 50, 75, 100, 125 and 150 mV/s. Inset: plot of peak current versus square root of the scan rate.

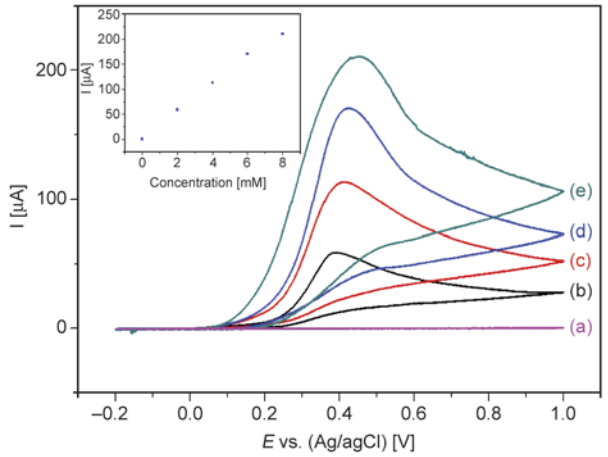

Figure 8. CV curves of AF-MWCNT/EPU-CPE with (a) 0.0 mM, (b) 2.0 mM, (c) 4.0 mM, (d) 6.0 mM and (e) 8.0 mM vitamin C concentrations

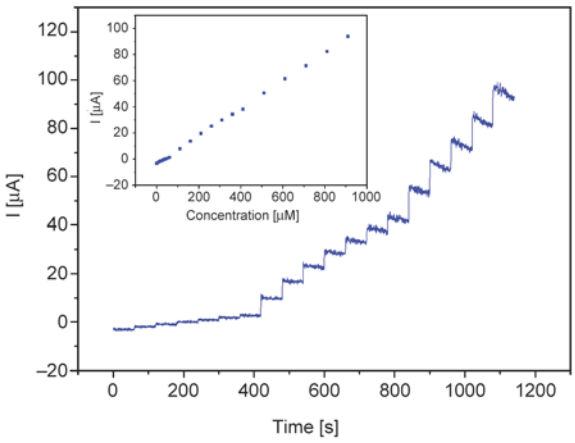

Figure 9. Amperometric current responses of AF-MWCNT/EPU-CPE for successive addition of vitamin C into a 30 mL PBS solution stirred constantly. Inset shows the calibration curve between the current and the concentration of vitamin C.

trode surface and reacted with the oxidized state of EPU, which led to the increase of the reduced state of EPU. This increase of the reduced state of EPU resulted in the increase of the oxidation currents [48, 49]. The inset shows the peak currents plotted as a function of the amount of vitamin C added. A linear relationship with the vitamin C concentration in the range from 0.0 to 8.0 mM (R^2 = 0.996, n = 5) was observed.

At an applied potential of 0.40 V, the successive addition of vitamin C from 10 μM to 910 μM in 0.1 M PBS to the AF/MWCNT/EPU-CPE increased the current successively. This phenomenon occurred in 1.46 s. The rapidity of the detection was attributed to the oxidation and reduction reactions occurring directly as shown in Figure 9. There was a linear relationship between the concentration of vitamin C added and the peak current obtained, as evidenced by the linear calibration curve of the amperometric response of the sensor to the concentration of vitamin C provided in the inset (R^2 = 0.999 for AF-MWCNT/EPU-CPE). The detection limit of the AF-MWCNT/EPU-CPE vitamin C sensor was 1.2 μM at *S/N* (signal to noise ratio) of 3 and the sensitivity was 35.3 μA·mM^{-1}. The detection range, the sensitivity and the detection limit of the AF-MWCNT/EPU-CPE comparable to those of most modified electrodes reported in literature (Table 2). The sensitivity and the detection limit observed in the present study were higher than that observed in most other reports in literature. There was also a great improvement in sensitivity and detection limit compared to previously reported studies [52]. To further study the stability of AF-MWCNT/EPU-CPE, the electrode was well preserved at PBS solution (4 °C) and detected at different times. In Figure 10, the current response did not significantly decay in the first week. After two weeks, the current response of the same electrode still reached 91.2% of the original

Table 2. A comparison of various types of ascorbate biosensors

Modified electrode	Detection limit [μM]	Sensitivity [μA·mM^{-1}]	Applied potential (vs. Ag/AgCl) [V]	Linear range [mM]	Optimum pH	R^2	Reference
EPI/CPE	9.6	[a]NR	0.4	[a]NR	7	0.996	[27]
PANI/GCE	0.4	[a]NR	0.1–0.3	0.0004–2	6–7	0.999	[50]
PANI/[b]OAA/PT	500	[a]NR	0.34	5–60	7	[a]NR	[51]
EPU/CPE	6.1	15.4	0.42	0.05–0.5	7	0.996	[52]
PANI/ITO	18.0	12.0	–0.135	0.05–0.4	7	0.999	[53]
MWNT-*g*-poly(2,5-dimethoxyaniline)/ITO	0.1	12.78	0.32	1.0–5.0	7	0.999	[54]
[c]pAPTT/GCE	1.4	10.0	0.3	0.01–0.2	4	0.998	[55]
AF-MWCNT/EPU/CPE	1.2	35.3	0.4	0.01–0.91	7	0.999	This work

[a]NR= Not reported
[b]OAA= orthanilic acid
[c]pAPTT = poly-3′-(2-aminopyrimidyl)-2,2′:5′,2′-terthiophene

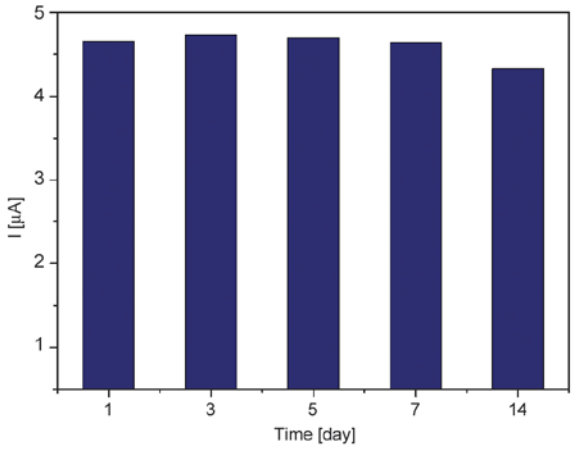

Figure 10. The relationship between the respond current of 100 μM vitamin C and time

current. These results revealed the developed AF-MWCNT/EPU-CPE is an electrode with excellent reliability for sensing vitamin C.

4. Conclusions

The electroactive polyurea incorporated with AF-MWCNTs was prepared to modify the CPE and the resulting AF-MWCNT/EPU-CPE was utilized to detect vitamin C. UV-Vis and CV tests confirmed that the AF-MWCNT/EPU composite was successfully synthesized and hence led to effective site-selective interactions between the quinoid ring of EPU and AF-MWCNTs, facilitating charge-transfer processes between the two components. Furthermore, the conductivityy of EPU was improved by five orders when incorporating AF-MWCNTs. Therefore, the electrocatalytic property of AF-MWCNT/EPU composites toward the oxidation of vitamin C was significantly enhanced. The detection limit and sensitivity of AF-MWCNT/EPU-CPE for detecting vitamin C was 1.2 μM at *S*/*N* of 3 and 35.3 $\mu A \cdot mM^{-1}$, respectively. The prepared AF-MWCNT/EPU carbon paste modified electrode showed excellent sensitivity and detection limit for determination of vitamin C. We are confident that the results of this study will significantly contribute to the advance of polymer composite sensors.

Acknowledgements

This research was supported by the Ministry of Science and Technology, R. O. C. (MOST-103-2221-E-167-037-MY3 and 104-2811-E-167-001). We thank Mr Chun-An Chen for the schematic design.

References

[1] Virji S., Huang J., Kaner R. B., Weiller B. H.: Polyaniline nanofiber gas sensors: Examination of response mechanisms. Nano Letters, **4**, 491–496 (2004). DOI: 10.1021/nl035122e

[2] Maiti S., Khatua B. B.: Polyaniline integrated carbon nanohorn: A superior electrode materials for advanced energy storage. Express Polymer Letters, **8**, 895–907 (2014). DOI: 10.3144/expresspolymlett.2014.91

[3] Tian Z., Yu H., Wang L., Saleem M., Ren F., Ren P., Chen Y., Sun R., Sun Y., Huang L.: Recent progress in the preparation of polyaniline nanostructures and their applications in anticorrosive coatings. RSC Advances, **4**, 28195–28208 (2014). DOI: 10.1039/C4RA03146F

[4] Shahhosseini L., Nateghi M. R., SheikhSivandi S.: Electrochemical synthesis of polymer based on 4-(2-thienyl) benzenamine in aqueous solutions: Electrochemical properties, characterization and application. Synthetic Metals, **211**, 66–74 (2016). DOI: 10.1016/j.synthmet.2015.11.015

[5] Sudha J. D., Sivakala S., Chandrakanth C. K., Neethu K. S., Rohini K. N., Ramakrishnan R.: Percolated conductive polyaniline-clay nanocomposite in polyvinyl chloride through the combined approach porous template and self-assembly. Express Polymer Letters, **8**, 107–115 (2014). DOI: 10.3144/expresspolymlett.2014.13

[6] Luo Y., Wang X., Guo W., Rohwerder M.: Growth behavior of initial product layer formed on Mg alloy surface induced by polyaniline. Journal of the Electrochemical Society, **162**, C294–C301 (2015). DOI: 10.1149/2.1101506jes

[7] Sim B., Chae H. S., Choi H. J.: Fabrication of polyaniline coated iron oxide hybrid particles and their dual stimuli-response under electric and magnetic fields. Express Polymer Letters, **9**, 736–743 (2015). DOI: 10.3144/expresspolymlett.2015.68

[8] Wang L. X., Soczka-Guth T., Havinga E., Müllen K.: Poly(phenylenesulfidephenylenamine) (PPSA) – The 'compound' of polyphenylenesulfide with polyaniline. Angewandte Chemie International Edition, **35**, 1495–1497 (1996). DOI: 10.1002/anie.199614951

[9] Wei Y., Yang C., Wei G., Feng G.: A new synthesis of aniline oligomers with three to eight amine units. Synthetic Metals, **84**, 289–291 (1997). DOI: 10.1016/S0379-6779(97)80756-4

[10] Shao Z., Yu Z., Hu J., Chandrasekaran S., Lindsay D. M., Wei Z., Faul C. F. J.: Block-like electroactive oligo (aniline)s: Anisotropic structures with anisotropic function. Journal of Materials Chemistry, **22**, 16230–16234 (2012). DOI: 10.1039/C2JM32278A

[11] Kim T-G., Park J-W.: Synthesis of poly(oligoaniline)s with structures controlled over three different oxidation states. Journal of Polymer Science Part A: Polymer Chemistry, **50**, 1851–1860 (2012).
DOI: 10.1002/pola.25960

[12] Qu G., Li F., Berda E. B., Chi M., Liu X., Wang C., Chao D.: Electroactive polyurea bearing oligoaniline pendants: Electrochromic and anticorrosive properties. Polymer, **58**, 60–66 (2015).
DOI: 10.1016/j.polymer.2014.12.033

[13] Li F., Zhou M., Wang J., Liu X., Wang C., Chao D.: Synthesis and electrochemical properties of electroactive hyperbranched poly(aryl ether ketone) bearing oligoaniline segments. Synthetic Metals, **205**, 42–47 (2015).
DOI: 10.1016/j.synthmet.2015.03.019

[14] Wang S., Chao D., Berda E. B., Jia X., Yang R., Wang C.: Multicolor electrochromic performance of electroactive poly(amic acid) containing pendant oligoaniline, azobenzene and sulfonic acid groups. Electrochimica Acta, **89**, 594–599 (2013).
DOI: 10.1016/j.electacta.2012.10.149

[15] Huang L., Zhuang X., Hu J., Lang L., Zhang P., Wang Y., Chen X., Wei Y., Jing X.: Synthesis of biodegradable and electroactive multiblock polylactide and aniline pentamer copolymer for tissue engineering applications. Biomacromolecules, **9**, 850–858 (2008).
DOI: 10.1021/bm7011828

[16] Gharibi R., Yeganeh H., Gholami H., Hassan Z. M.: Aniline tetramer embedded polyurethane/siloxane membranes and their corresponding nanosilver composites as intelligent wound dressing materials. RSC Advances, **4**, 62046–62060 (2014).
DOI: 10.1039/C4RA11454J

[17] Huang L., Hu J., Lang L., Wang X., Zhang P., Jing X., Wang X., Chen X., Lelkes P. I., MacDiarmid A. G., Wei Y.: Synthesis and characterization of electroactive and biodegradable ABA block copolymer of polylactide and aniline pentamer. Biomaterials, **28**, 1741–1751 (2007).
DOI: 10.1016/j.biomaterials.2006.12.007

[18] Hardy C. G., Islam M. S., Gonzalez-Delozier D., Morgan J. E., Cash B., Benicewicz B. C., Ploehn H. J., Tang C.: Converting an electrical insulator into a dielectric capacitor: End-capping polystyrene with oligoaniline. Chemistry of Materials, **25**, 799–807 (2013).
DOI: 10.1021/cm304057f

[19] Huang T-C., Yeh T-C., Huang H-Y., Ji W-F., Chou Y-C., Hung W-I., Yeh J-M., Tsai M-H.: Electrochemical studies on aniline-pentamer-based electroactive polyimide coating: Corrosion protection and electrochromic properties. Electrochimica Acta, **56**, 10151–10158 (2011).
DOI: 10.1016/j.electacta.2011.08.114

[20] Huang T-C., Su Y-A., Yeh T-C., Huang H-Y., Wu C-P., Huang K-Y., Chou Y-C., Yeh J-M., Wei Y.: Advanced anticorrosive coatings prepared from electroactive epoxy–SiO_2 hybrid nanocomposite materials. Electrochimica Acta, **56**, 6142–6149 (2011).
DOI: 10.1016/j.electacta.2011.04.053

[21] Huang H-Y., Lee Y-T., Yeh L-C., Jian J-W., Huang T-C., Liang H-T., Yeh J-M., Chou Y-C.: Photoactively electroactive polyamide with azo group in the main chain *via* oxidative coupling polymerization. Polymer Chemistry, **4**, 343–350 (2013).
DOI: 10.1039/C2PY20374J

[22] Huang T-C., Yeh T-C., Huang H-Y., Ji W-F., Lin T-C., Chen C-A., Yang T-I., Yeh J-M.: Electrochemical investigations of the anticorrosive and electrochromic properties of electroactive polyamide. Electrochimica Acta, **63**, 185–191 (2012).
DOI: 10.1016/j.electacta.2011.12.087

[23] Yeh T-C., Huang T-C., Huang H-Y., Huang Y-P., Cai Y-T., Lin S-T., Wei Y., Yeh J-M.: Electrochemical investigations on anticorrosive and electrochromic properties of electroactive polyurea. Polymer Chemistry, **3**, 2209–2216 (2012).
DOI: 10.1039/C2PY20061A

[24] Huang H-Y., Jian J-W., Lee Y-T., Li Y-T., Huang T-C., Chang J-H., Yeh L-C., Yeh J-M.: Effect of photoisomerization on the electroactivity and electrochromic behavior of aniline pentamer-based polymers with azo chromophore as reversibly switchable pendant group. Polymer, **53**, 4967–4976 (2012).
DOI: 10.1016/j.polymer.2012.09.003

[25] Wang S., Chao D., Berda E. B., Jia X., Yang R., Wang X., Jiang T., Wang C.: Fabrication of electroactive oligoaniline functionalized poly(amic acid) nanofibers for application as an ammonia sensor. RSC Advances, **3**, 4059–4065 (2013).
DOI: 10.1039/C3RA00056G

[26] Wang S., Berda E. B., Lu X., Li X., Wang C., Chao D.: Tuning the fluorescent response of a novel electroactive polymer with multiple stimuli. Macromolecular Rapid Communications, **34**, 1648–1653 (2013).
DOI: 10.1002/marc.201300448

[27] Huang T-C., Lin S-T., Yeh L-C., Chen C-A., Huang H-Y., Nian Z-Y., Chen H-H., Yeh J-M.: Aniline pentamer-based electroactive polyimide prepared from oxidation coupling polymerization for electrochemical sensing application. Polymer, **53**, 4373–4379 (2012).
DOI: 10.1016/j.polymer.2012.07.064

[28] Iijima S.: Helical microtubules of graphitic carbon. Nature, **354**, 56–58 (1991).
DOI: 10.1038/354056a0

[29] Belin T., Epron F.: Characterization methods of carbon nanotubes: A review. Materials Science and Engineering: B, **119**, 105–118 (2005).
DOI: 10.1016/j.mseb.2005.02.046

[30] Park S., Vosguerichian M., Bao Z.: A review of fabrication and applications of carbon nanotube film-based flexible electronics. Nanoscale, **5**, 1727–1752 (2013).
DOI: 10.1039/C3NR33560G

[31] Pradhan A. K., Prusty G., Swain S. K.: Characterization of polyacrylonitrile nanocomposites by reinforcement of functionalized single-walled carbon nanotubes. Polymer-Plastics Technology and Engineering, **53**, 784–789 (2014).
DOI: 10.1080/03602559.2014.886042

[32] Prusty G., Das R., Swain S. K.: Influence of functionalized single-walled carbon nanotubes on morphology, conducting and oxygen barrier properties of poly(acrylonitrile-*co*-starch). Composites Part B: Engineering, **62**, 236–241 (2014).
DOI: 10.1016/j.compositesb.2014.03.006

[33] Pradhan A. K., Swain S. K.: Oxygen barrier of multiwalled carbon nanotube/polymethyl methacrylate nanocomposites prepared by *in situ* method. Journal of Materials Science and Technology, **28**, 391–395 (2012).
DOI: 10.1016/S1005-0302(12)60073-5

[34] Chauhan N., Narang J., Pundir C. S.: Fabrication of multiwalled carbon nanotubes/polyaniline modified Au electrode for ascorbic acid determination. Analyst, **136**, 1938–1945 (2011).
DOI: 10.1039/C0AN00218F

[35] Zhang X., Lai G., Yu A., Zhang H.: A glassy carbon electrode modified with a polyaniline doped with silicotungstic acid and carbon nanotubes for the sensitive amperometric determination of ascorbic acid. Microchimica Acta, **180**, 437–443 (2013).
DOI: 10.1007/s00604-013-0939-1

[36] Padayatty S. J., Katz A., Wang Y., Eck P., Kwon O., Lee J-H., Chen S., Corpe C., Dutta A., Dutta S. K., Levine M.: Vitamin C as an antioxidant: Evaluation of its role in disease prevention. Journal of the American College of Nutrition, **22**, 18–35 (2003).
DOI: 10.1080/07315724.2003.10719272

[37] Jeon I-Y., Tan L-S., Baek J-B.: Synthesis and electrical properties of polyaniline/polyaniline grafted multiwalled carbon nanotube mixture *via in situ* static interfacial polymerization. Journal of Polymer Science Part A: Polymer Chemistry, **48**, 1962–1972 (2010).
DOI: 10.1002/pola.23963

[38] Huang T-C., Yeh L-C., Huang H-Y., Nian Z-Y., Yeh Y-C., Chou Y-C., Yeh J-M., Tsai M-H.: The use of a carbon paste electrode mixed with multiwalled carbon nanotube/electroactive polyimide composites as an electrode for sensing ascorbic acid. Polymer Chemistry, **5**, 630–637 (2014).
DOI: 10.1039/C3PY00787A

[39] Okpalugo T. I. T., Papakonstantinou P., Murphy H., McLaughlin J., Brown N. M. D.: High resolution XPS characterization of chemical functionalised MWCNTs and SWCNTs. Carbon, **43**, 153–161 (2005).
DOI: 10.1016/j.carbon.2004.08.033

[40] Yang S-Y., Lin W-N., Huang Y-L., Tien H-W., Wang J-Y., Ma C-C. M., Li S-M., Wang Y-S.: Synergetic effects of graphene platelets and carbon nanotubes on the mechanical and thermal properties of epoxy composites. Carbon, **49**, 793–803 (2011).
DOI: 10.1016/j.carbon.2010.10.014

[41] He X., Zhang F., Wang R., Liu W.: Preparation of a carbon nanotube/carbon fiber multi-scale reinforcement by grafting multi-walled carbon nanotubes onto the fibers. Carbon, **45**, 2559–2563 (2007).
DOI: 10.1016/j.carbon.2007.08.018

[42] Swain S. K., Pradhan A. K., Sahu H. S.: Synthesis of gas barrier starch by dispersion of functionalized multiwalled carbon nanotubes. Carbohydrate Polymers, **94**, 663–668 (2013).
DOI: 10.1016/j.carbpol.2013.01.056

[43] Zhang H., Li H. X., Cheng H. M.: Water-soluble multiwalled carbon nanotubes functionalized with sulfonated polyaniline. The Journal of Physical Chemistry B, **110**, 9095–9099 (2006).
DOI: 10.1021/jp060193y

[44] Sun Y., Wilson S. R., Schuster D. I.: High dissolution and strong light emission of carbon nanotubes in aromatic amine solvents. Journal of the American Chemical Society, **123**, 5348–5349 (2001).
DOI: 10.1021/ja0041730

[45] Dhand C., Arya S. K., Singh S. P., Singh B. P., Datta M., Malhotra B. D.: Preparation of polyaniline/multiwalled carbon nanotube composite by novel electrophoretic route. Carbon, **46**, 1727–1735 (2008).
DOI: 10.1016/j.carbon.2008.07.028

[46] Zhao H., Yuan W. Z., Tang L., Sun J. Z., Xu H., Qin A., Mao Y., Jin J. K., Tang B. Z.: Hybrids of triphenylamine-functionalized polyacetylenes and multiwalled carbon nanotubes: High solubility, strong donor–acceptor interaction, and excellent photoconductivity. Macromolecules, **41**, 8566–8574 (2008).
DOI: 10.1021/ma8014323

[47] Zhai D., Liu B., Shi Y., Pan L., Wang Y., Li W., Zhang R., Yu G.: Highly sensitive glucose sensor based on Pt nanoparticle/polyaniline hydrogel heterostructures. ACS Nano, **7**, 3540–3546 (2013).
DOI: 10.1021/nn400482d

[48] Ambrosi A., Morrin A., Smyth M. R., Killard A. J.: The application of conducting polymer nanoparticle electrodes to the sensing of ascorbic acid. Analytica Chimica Acta, **609**, 37–43 (2008).
DOI: 10.1016/j.aca.2007.12.017

[49] Chen S., Xu L., Yang Y., Li B., Hou J.: Improved electrocatalytic behavior of ascorbic acid by crosslinked polyaniline with enhanced conductivity. Analytical Methods, **3**, 2374–2378 (2011).
DOI: 10.1039/C1AY05310H

[50] O'Connell P. J., Gormally C., Pravda M., Guilbault G. G.: Development of an amperometric L-ascorbic acid (Vitamin C) sensor based on electropolymerised aniline for pharmaceutical and food analysis. Analytica Chimica Acta, **431**, 239–247 (2001).
DOI: 10.1016/S0003-2670(00)01330-1

[51] Zhang L.: Electrochemical synthesis of self-doped polyaniline and its use to the electrooxidation of ascorbic acid. Journal of Solid State Electrochemistry, **11**, 365–371 (2007).
DOI: 10.1007/s10008-006-0151-x

[52] Yeh L-C., Huang T-C., Huang Y-P., Huang H-Y., Chen H-H., Yang T-I., Yeh J. M.: Synthesis electroactive polyurea with aniline-pentamer-based in the main chain and its application in electrochemical sensor. Electrochimica Acta, **94**, 300–306 (2013).
DOI: 10.1016/j.electacta.2013.01.073

[53] Roy A. K., Nisha V. S., Dhand C., Malhotra B. D.: Molecularly imprinted polyaniline film for ascorbic acid detection. Journal of Molecular Recognition, **24**, 700–706 (2011).
DOI: 10.1002/jmr.1104

[54] Ragupathy D., Park J. J., Lee S. C., Kim J. C., Gomathi P., Kim M. K., Lee S. M., Ghim H. D., Rajendran A., Lee S. H., Jeon K. M.: Electrochemical grafting of poly(2,5-dimethoxy aniline) onto multiwalled carbon nanotubes nanocomposite modified electrode and electrocatalytic oxidation of ascorbic acid. Macromolecular Research, **19**, 764–769 (2011).
DOI: 10.1007/s13233-011-0802-3

[55] Abdelwahab A. A., Kim D-M., Halappa N. M., Shim Y-B.: A selective catalytic oxidation of ascorbic acid at the aminopyrimidyl functionalized-conductive polymer electrode. Electroanalysis, **25**, 1178–1184 (2013).
DOI: 10.1002/elan.201200650

eXPRESS Polymer Letters Vol.10, No.6 (2016) 462–469
Available online at www.expresspolymlett.com
DOI: 10.3144/expresspolymlett.2016.44

A new insight into foaming mechanisms in injection molding via a novel visualization mold

*V. Shaayegan, L. H. Mark, A. Tabatabaei, C. B. Park**

Microcellular Plastics Manufacturing Laboratory, Department of Mechanical and Industrial Engineering, University of Toronto, M5S 3G8, Toronto, Ontario, Canada

Received 21 October 2015; accepted in revised form 27 December 2015

Abstract. The complex mechanisms of bubble nucleation and dynamics in foam injection molding have not been uncovered despite many previous efforts due to the non-steady stop-and-flow nature of injection molding and the non-uniform temperature and pressure distributions in the mold. To this end, a new visualization mold was designed and manufactured for the direct observation of bubble nucleation and growth/collapse in foam injection molding. A reflective prism was incorporated into the stationary part of the injection mold with which the nucleation and growth behaviors of bubbles were successfully observed. The mechanisms of bubble nucleation in low- and high-pressure foam injection molding, with and without the application of gas-counter pressure, was investigated. We identified how the inherently non-uniform cell structure is developed in low-pressure foam injection molding with gate-nucleated bubbles, and when and how cell nucleation occurs in high-pressure foam injection molding with a more uniform pressure drop.

Keywords: *processing technologies, nucleation mechanism, foam injection molding, in-situ visualization, polystyrene*

1. Introduction

Foam injection molding (FIM) is an encouraging manufacturing method, owing to its capability to produce lightweight products by using less material and consuming less energy at fast production rates. In addition, recent studies have demonstrated that the formation of the cellular structure in FIM can improve mechanical and physical properties of the foamed parts [1–3]. However, most of the underlying mechanism(s), contributing to the cellular structure development, are not fully understood in this technology. The absence of a comprehensive understanding of bubble nucleation mechanisms, bubble dynamics, and mutual interactions of growing bubbles and fillers not only limits any structural improvement to empirical trial and errors, also hinders new material designs for enhancement of specific properties in products.

Although extensive research has been conducted to interpret the foaming phenomena in FIM, characterization was performed on the final structure after the samples were stabilized [4]. Therefore, the foaming phenomena were not tracked during the process. Additionally, most of hypotheses or theoretical simulations were not experimentally verified [5, 6]. In this context, the in-situ observation of foaming phenomena drew significant attention amongst researchers [7–10]. Villamizar and Han [7] designed a rectangular visualization mold with transparent quartz walls to investigate the bubbles' dynamics in conventional structural FIM. Mahmoodi *et al*. [8] used a visualization setup in which one side of the mold cavity was replaced with a multi-layer glass block in the moving part of the mold. They conducted full-shot FIM experiments using polystyrene (PS)/carbon dioxide (CO_2) system to visualize cell growth and

*Corresponding author, e-mail: park@mie.utoronto.ca

collapse during non-isothermal mold filling. Ishikawa and Ohshima [9] designed a visualization mold in which a glass prism targeted the far end of the mold cavity to investigate the foaming behaviour of polypropylene (PP) blown with CO_2 during mold opening. Ishikawa *et al*. [10] extended their study to compare the nucleation effectiveness of nitrogen (N_2) with that of CO_2. Yamada *et al*. [11] observed a multilayer core structure in FIM experiments of PS blown with N_2, and justified this phenomenon by the local cavity pressure.

Our study explains the development of a new visualization mold for online observation of bubble nucleation and growth dynamics in FIM, compatible with laboratory-scale and small size injection molding machines. Compared with previous designs, ours provides novel features such as visual accessibility to critical locations in the mold, *i.e*., near the gate, far from the gate, and the area in-between them, while measuring the pressures at the visualized locations. Another unique component of our design is the gate pressure transducer, which can be used, along with other pressure transducers across the mold cavity, to measure the pressure difference before and after the gate. In our previous study, it was demonstrated that the pressure distributions before the gate and along the mold cavity provide critical information about the foaming dynamics during filling [4]. Nevertheless, most bubble nucleation and growth phenomena had to be theorized based on the pressure data because of the lack of visualization data. On the other hand, the visualized foaming results in the literature could not be properly interpreted due to the lack of pressure distributions in the cavity. The earlier researchers used a pressure transducer either at the end of the cavity [7], near the end [9], or near the gate [11]. Although the measured pressure was used for the interpretation of their data, the local pressure and visualized data could not describe the entire foaming phenomena in the mold cavity as the pressure profile changes along the mold cavity.

Unlike most available designs, the selection of small transparent windows in our design minimizes the effective polymer/glass interface, simulating a more realistic FIM process in terms of the heat transfer and the rheological implications on the cavity surface (Figure 1). Also, it reduces the probability of any thermal shock, or mechanical damage under high packing pressures. The location of the viewing windows in the fixed plate, on the opposite side of the mold cavity, makes it possible to perform various experiments by simply changing the mold insert, some of which includes, but is not limited to, gas-assisted FIM studies, shear/extension induced FIM, and the study of flow in various channels. Also, the mold can be utilized to investigate other FIM technologies such as gas-counter pressure (GCP) [12, 13] and mold opening (core back) [9, 10, 14, 15]. The designed mold can be utilized to further investigate the mechanisms of bubble nucleation/growth, interaction between bubbles and fillers [16, 17], the effect of formed crystals on foaming [18], weld-line studies [19], defects [20], and model verifications [21]. Since no commercial software can accurately describe the microcellular *MuCell* or structural FIM technologies, the use of the designed visualization mold will elucidate the details of the bubble nucleation mechanisms in FIM, and will provide reliable experimental data for model verification and software validation.

In this article, we demonstrate the dominant bubble nucleation mechanisms in low- and high-pressure FIM technologies by means of in-situ visualization. Polystyrene/CO_2 mixtures have been used as a case example.

2. System development

A detailed sketch of the designed visualization mold is shown in Figure 1. A prism-insert was designed and manufactured at which a right-angle glass prism was mounted to reflect the cavity images to a camera. The prism was a pure non-crystalline fused silica 7980 from Meller Optics Inc., with low refractive index variations, low birefringence values, and a low thermal expansion coefficient. The view surfaces of the prism were optically polished, and its hypotenuse was silver-coated in order to provide mirror action. The physical and optical properties of the prism are summarized in Table 1.

The reflective prism was precisely encased in a 4-piece prism-insert (Figure 1a). An insert pocket was then cut into a block of P20 mold steel and the prism-insert was fixed inside the mold. Three round, fused silica windows were provided from BMV Optical and mounted in a metallic frame. To ensure that the pressure readings represented the local pressure of the visualized spot, each window was carefully located in front of each of the cavity pressure transducers on the opposite side of the cavity. To measure the pressure before the gate, a Dynisco pressure

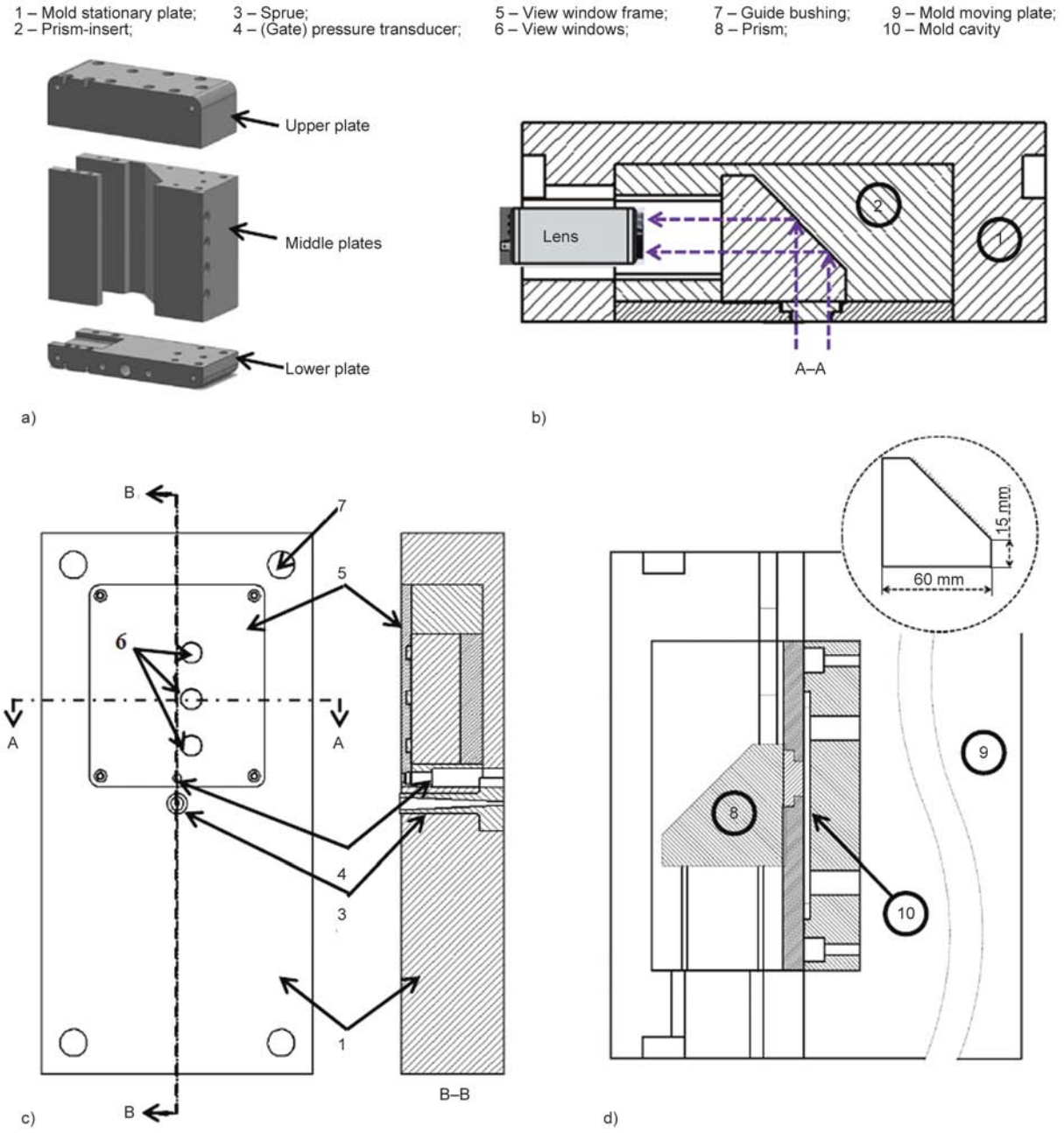

Figure 1. a) Prism-insert; b) top sectional view of the visualization mold stationary plate, the principle of the reflective prism, and the location of view windows; c) detailed design of the visualization mold stationary plate; d) top sectional view of the complete visualization mold

Table 1. Properties of fused silica

Part	Grade	Birefringence [nm/cm]	Shear Modulus* [GPa]	Bulk modulus* [GPa])	Surface finish [scratch/dig]	Surface flatness [wave]	Density [g/cm^3]
Prism	7980 Standard	≤5	31.0	35.9	40–10	1	2.20
Window	7980 KrF	≤1	31.4	35.4	40–10	1	2.20

*Properties measured at 25 °C

transducer (Franklin, USA) was incorporated into the mold and its sensor surface was flush-mounted. The complete assembly of the visualization mold with a detailed view of the assembly section is shown in Figure 2.

3. Materials and equipment

A grade of PS from Americas Styrenics (The Woodlands, TX), MC3650, with MFI = 13.0 g/10 min, was blown using CO_2 from Linde Gas Canada (Toronto, Canada). Nitrogen from Linde Gas Canada (Toronto,

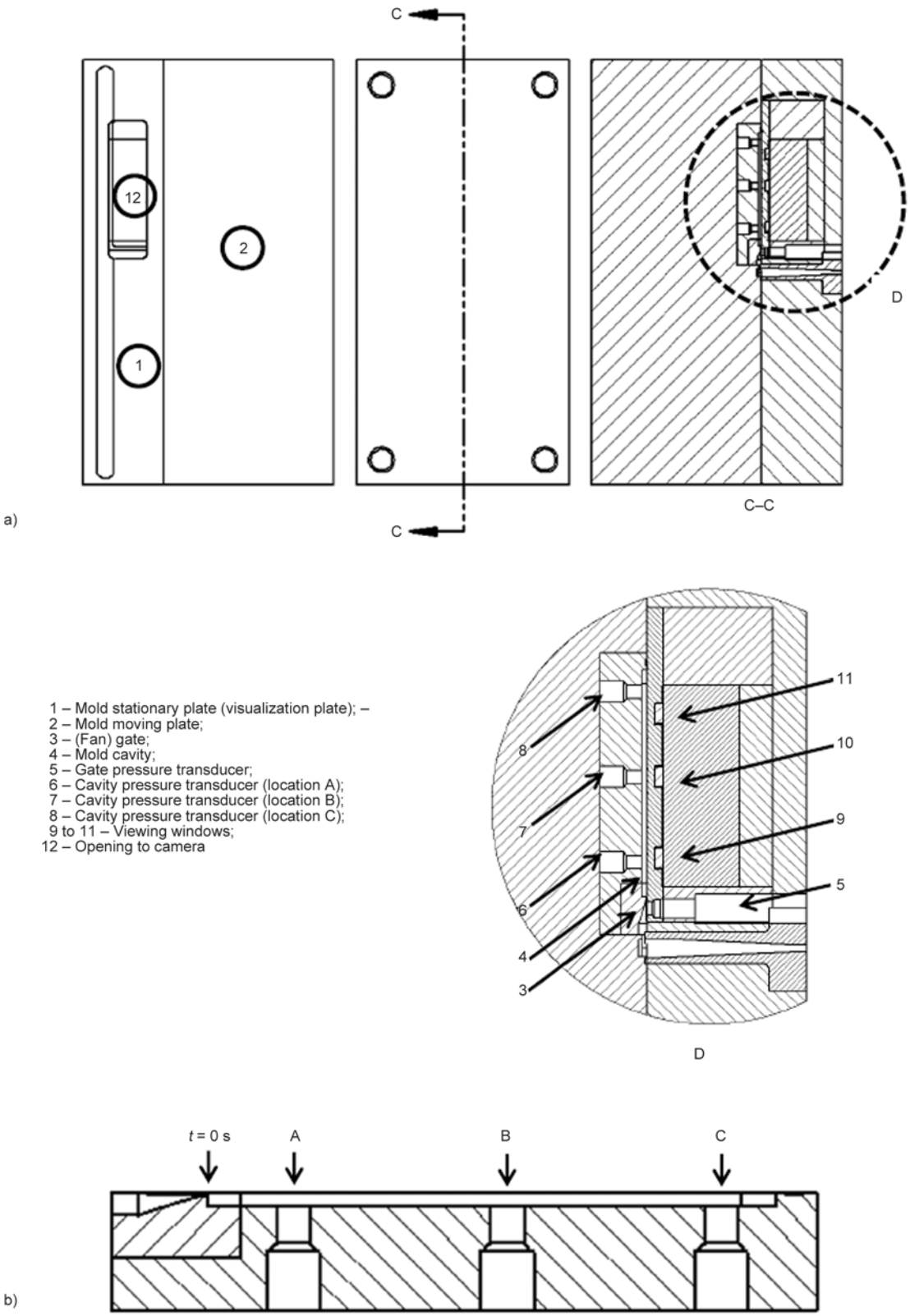

Figure 2. a) Visualization mold assembly and detailed location of the pressure transducers; b) gate and cavity cross section with identified locations (t = 0 s at the entrance of the cavity)

Canada) was used as the GCP medium. A 50 ton Arburg ALLROUNDER 270C injection molding machine equipped with a Trexel MuCell SCF delivery system was used to perform FIM experiments. A rectangular mold cavity with nominal dimensions of 135 mm×111 mm×3.2 mm, fed by a fan gate, was

Table 2. Processing parameters (in all experiments: T_{melt} = 230 °C; T_{Mold} = 25–30°C).

Process	Shot size [cm^3]	CO_2 [wt%]	Packing pressure [MPa]	Packing duration [s]	Injection speed [cm^3/s]	GCP [MPa]	Barrel pressure [MPa]
Low-pressure FIM (~20% void fraction)	50	2	0	None	50	None	17
Low-pressure FIM (≤5% void fraction)	58	2	0	None	50	None	17
High-pressure FIM	62	2	16	1	50	None	17
Near full-shot FIM + GCP	60	1	0	None	50	3.5	17

used to mold the samples. The imaging system consisted of a CV M10 camera from JAI and a magnifying lens from Navitar connected to a computer.

To investigate the governing bubble nucleation mechanisms in FIM, three types of experiments were carried out, namely low-pressure FIM [4], high-pressure FIM [3], and (almost) full-shot FIM using GCP [3]. The processing parameters for the FIM experiments are listed in Table 2. This should be noted that three *critical* locations were identified for the visualization of the mold cavity, such that Location A was near the gate, Location C was far from the gate and close to the end of the mold cavity, and Location B was in between Locations A and C (Locations A to C correspond to each view window illustrated in Figure 1c). The visual observations demonstrated in this research were carried out at Location B, and the time reference (i.e. t = 0 s) is set as the moment the melt/gas mixture enters the cavity (see Figure 2b).

4. Results and discussion

In FIM processing, a physical or chemical blowing agent (BA) is homogeneously mixed with the polymer melt, followed by a thermodynamic instability to induce bubble nucleation to the system [4]. The bubble nucleation mechanism and the final cellular structure are a strong function of the acquired thermodynamic instability, *via* the pressure drop, which in turn depends on the type of the FIM process.

In low-pressure FIM, the mold cavity was partially filled with the melt/gas mixture [22]. In this scheme, the pressure of the melt/gas mixture dropped below the solubility pressure of the dissolved BA once it entered the mold cavity; therefore, a myriad of cells (i.e. gate-nucleated bubbles) nucleate at the gate. Figure 3a schematically shows the cell nucleation and free-expansion growth in low-pressure FIM. As illustrated, gate-nucleated bubbles grow, get sheared and elongated, and coalesce during their travel along the mold cavity. Figure 3b shows the successive snapshots of the cavity visualization for a low-pressure FIM with 20% void fraction. Because of the large void fraction, the cavity pressure remained below the solubility pressure of the BA; hence a large number of cells were nucleated at the gate under a fast pressure drop rate, and the (foggy) melt front was associated with fast cell nucleation and gas escape. In this case, the nucleated bubbles could not be visually detected. In order to visualize the behaviour of bubbles, we increased the shot size (i.e. smaller void fraction) such that the increased cavity pressure suppressed the cell nucleation at the gate to a large extent. Therefore, a smaller number of cells were induced during filling, and a clear image

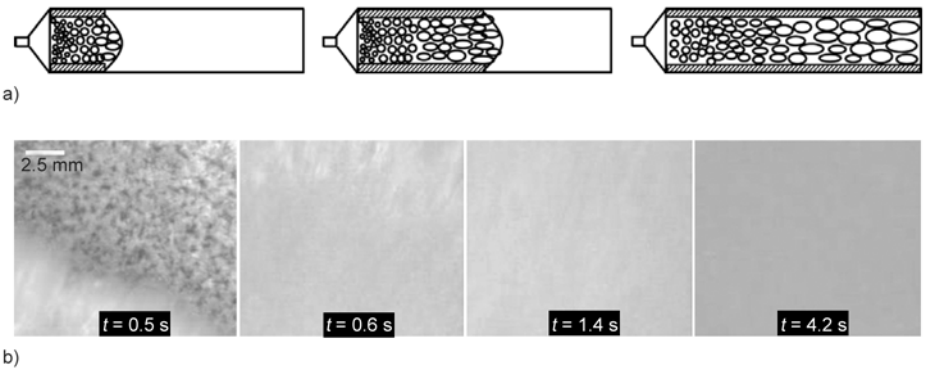

Figure 3. a) Schematic of low-pressure FIM (formation and growth of gate-nucleated bubbles, which get sheared and coalesced during mold filling and free expansion; the hatched area shows the formed skin layer); b) successive snapshots for low-pressure FIM experiments of PS-2% CO_2 with 20% void fraction. (Injection Speed = 50 cm^3·s^{-1}; T_{melt} = 230 °C; Visualization location = B. The time was set to zero at the moment when the melt entered the mold cavity.)

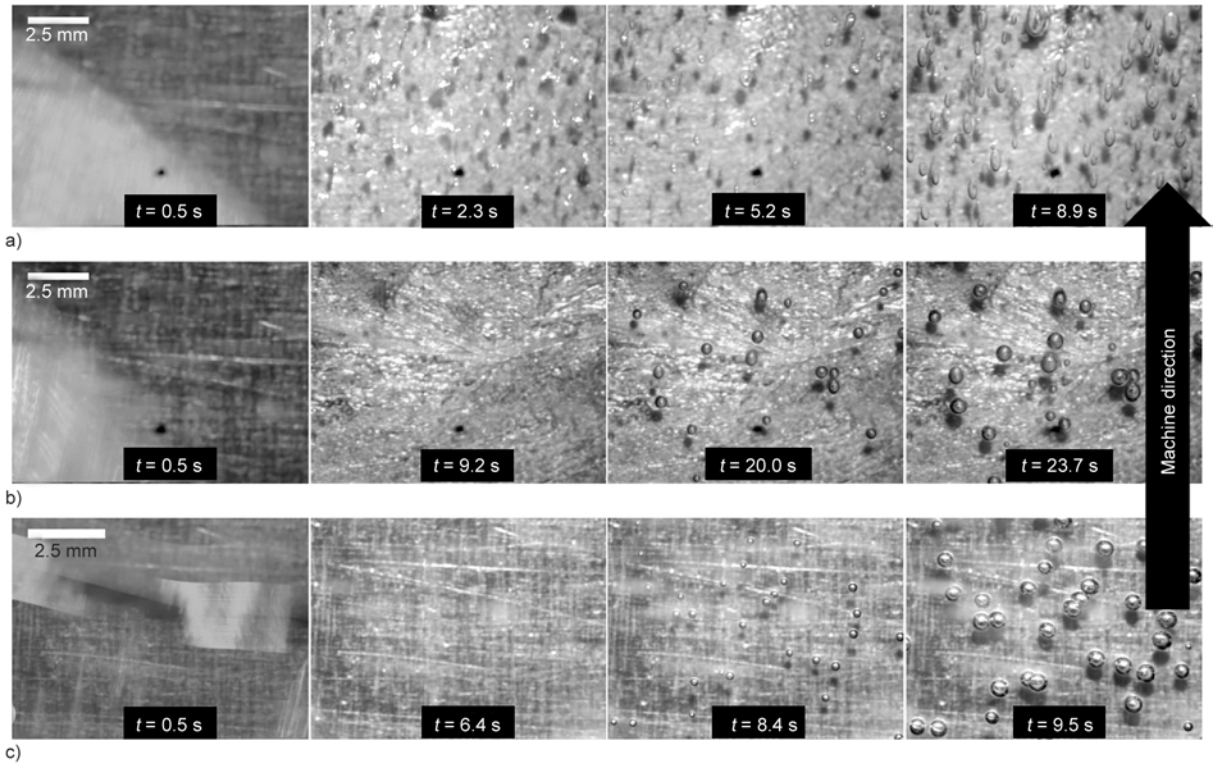

Figure 4. Mechanism of bubble nucleation in FIM: a) Low-pressure FIM, CO_2 = 2%; void fraction ≤5%; b) high-pressure FIM, CO_2 = 2%, pack pressure = 16 MPa, packing time = 1 s; c) foam injection molding using GCP, CO_2 = 1%, GCP removal time = 7 s (Injection speed = 50 $cm^3 \cdot s^{-1}$; T_{melt} = 230 °C; Visualization location = B. The time was set to zero at the moment when the melt entered the mold cavity.)

was obtained, as shown in Figure 4a. The bubble nucleation occurred very quickly as a result of the pressure drop obtained over the gate (where the time was set to zero). As the melt flowed along the cavity, the gate-nucleated bubbles grew as a sensitive function of the mold pressure by the diffusion of the remaining gas molecules into the nucleated bubbles, as shown for t = 2.3 to 8.9 s in Figure 4a. Because of the pressure gradient across the mold cavity and bubble coalescence, considerable inhomogeneity in the foam morphology is typically developed at different locations of the mold.

In high-pressure FIM, on the other hand, a full shot was used to completely fill out the mold cavity. As in the case of low-pressure FIM, foaming occurred upon the entry of the melt/gas mixture into the mold cavity. However, all the gate-nucleated bubbles are to re-dissolve into the melt under the cavity pressure in this method. If the cavity pressure does not suffice for dissolution of gate-nucleated bubbles, then the melt packing pressure can be continuously applied. The pressure drop, responsible for bubble nucleation, is then attainable during melt solidification and shrinkage. As shown in Figure 4b, foaming started upon the entry of the melt/gas mixture into the cavity, and the melt front advancement was associated with bubble nucleation, foaming, and gas-escape. However, the gate-nucleated bubbles disappeared under the cavity pressure and new bubbles eventually nucleated, after about 9 seconds, during solidification. Therefore, the main difference between the nucleation mechanism in low-pressure and high-pressure FIM schemes was the source of the pressure drop, which induced bubble nucleation.

In order to increase the surface quality and structural homogeneity of FIM parts, the FIM process was performed using GCP [12, 13]. In this method, the mold cavity was charged with GCP, higher than the solubility pressure of the dissolved BA, prior to the filling step. This high-pressure gas was then exhausted as the injection proceeded. Figure 4c illustrates successive snapshots from visualization results of FIM experiments using GCP. As demonstrated, the GCP prevented foaming and gas-scape, evidenced by a smooth and transparent melt front, and postponed the bubble nucleation moment till the end of the filling stage. Once the GCP was removed, bubble nucleation occurred.

The cavity pressure profiles, at Locations A and B, corresponding to the aforementioned experiments

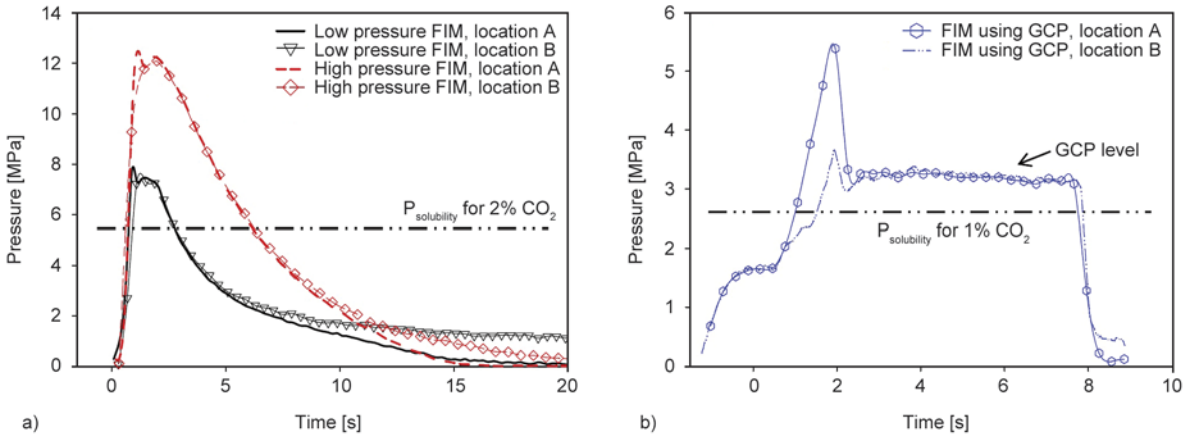

Figure 5. Pressure profiles in FIM experiments at 50 $cm^3 \cdot s^{-1}$ a) low- and high-pressure FIM; b) FIM+GCP (The time reference is the moment of the melt entry into the mold cavity.)

are shown in Figure 5. The cavity pressures in high-pressure FIM were higher than those in low-pressure FIM, due to the application of melt packing. Further, while a discrepancy was observed in pressure-decay profiles recorded at Locations A and B in low-pressure FIM, the pressure profiles almost coincided in the cases of high-pressure FIM and FIM experiments using GCP. Compared with the high-pressure case, a greater discrepancy in the pressure-decay profiles recorded at Locations A and B of low-pressure experiments indicated on bigger bubbles at Location B and a larger structural heterogeneity. The study of pressure profiles in experiments using GCP revealed that a very rapid pressure drop, but similar, was obtained at both Locations A and B upon the GCP release, enhancing the bubble nucleation rate and improving the structural uniformity.

5. Conclusions

An innovative visualization mold was successfully designed and used to investigate bubble nucleation and growth in foam injection molding. Visualization results revealed that the prevailing nucleation mechanisms in low-pressure foam injection molding is the one occurring as a result of the pressure drop obtained at the gate. In high-pressure foam injection molding, in contrast, the gate-nucleated bubbles disappeared under the high pressure of the mold cavity using melt packing, and the nucleation of new bubbles, happening during melt solidification and shrinkage, governed the ultimate cellular structure. The pressure profiles recorded at visualized spots indicated on a higher cavity pressure, required for the dissolution of gate-nucleated bubbles in high-pressure foam injection molding. By the application of gas-counter pressure, bubble nucleation was prevented till the end of the mold filling, and initiated upon the gas-counter pressure removal. By combining the information from *in-situ* visualization and cavity pressure, proper processing conditions can be effectively derived for each processing scheme.

Acknowledgements

This work was supported by the Natural Science and Engineering Research Council of Canada (NSERC 154279-2010). The authors are grateful to the Consortium of Cellular and Micro-Cellular Plastics (CCMCP) for their financial support. The polystyrene used in this research was provided by Americas Styrenics, TX, United States. Special thanks to Ryan Mendell, Machine Shop Manager, and Gordon Boudreau and Jeff Sansome, Machine Shop specialists, in the Department of Mechanical and Industrial Engineering of the University of Toronto, for their professional advice and constant support.

References

[1] Ameli A., Jung P. U., Park C. B.: Electrical properties and electromagnetic interference shielding effectiveness of polypropylene/carbon fiber composite foams. Carbon, **60**, 379–391 (2013).
DOI: 10.1016/j.carbon.2013.04.050

[2] Ameli A., Wang S., Kazemi Y., Park C. B., Pötschke P.: A facile method to increase the charge storage capability of polymer nanocomposites. Nano Energy, **15**, 54–65 (2015).
DOI: 10.1016/j.nanoen.2015.04.004

[3] Ameli A., Jahani D., Nofar M., Jung P. U., Park C. B.: Development of high void fraction polylactide composite foams using injection molding: Mechanical and thermal insulation properties. Composites Science and Technology, **90**, 88–95 (2014).
DOI: 10.1016/j.compscitech.2013.10.019

[4] Lee J. W. S., Wang J., Yoon J. D., Park C. B.: Strategies to achieve a uniform cell structure with a high void fraction in advanced structural foam molding. Industrial and Engineering Chemistry Research, **47**, 9457–9464 (2009).
DOI: 10.1021/ie0707016

[5] Arefmanesh A., Advani S. G., Michaelides E. E.: A numerical study of bubble growth during low pressure structural foam molding process. Polymer Engineering and Science, **30**, 1330–1337 (1990).
DOI: 10.1002/pen.760302011

[6] Ramesh N. S., Rasmussen D. H., Campbell G. A.: Numerical and experimental studies of bubble growth during the microcellular foaming process. Polymer Engineering and Science, **31**, 1657–1664 (1991).
DOI: 10.1002/pen.760312305

[7] Villamizar C. A., Han C. D.: Studies on structural foam processing II. Bubble dynamics in foam injection molding. Polymer Engineering and Science, **18**, 699–710 (1978).
DOI: 10.1002/pen.760180905

[8] Mahmoodi M., Behravesh A. H., Rezavand S. A. M., Pashaei A.: Visualization of bubble dynamics in foam injection molding. Journal of Applied Polymer Science, **116**, 3346–3355 (2010).
DOI: 10.1002/app.31839

[9] Ishikawa T., Ohshima M.: Visual observation and numerical studies of polymer foaming behavior of polypropylene/carbon dioxide system in a core-back injection molding process. Polymer Engineering and Science, **51**, 1617–1625 (2011).
DOI: 10.1002/pen.21945

[10] Ishikawa T., Taki K., Ohshima M.: Visual observation and numerical studies of N_2 vs. CO_2 foaming behavior in core-back foam injection molding. Polymer Engineering and Science, **52**, 875–883 (2012).
DOI: 10.1002/pen.22154

[11] Yamada T., Murata Y., Yokoi H.: Visualization analysis of a multilayer foam development process in microcellular injection molding. International Polymer Processing, **27**, 299–309 (2012).
DOI: 10.3139/217.2443

[12] Chen S-C., Liao W-H., Chien R-D.: Structure and mechanical properties of polystyrene foams made through microcellular injection molding *via* control mechanisms of gas counter pressure and mold temperature. International Communications in Heat and Mass Transfer, **39**, 1125–1131 (2012).
DOI: 10.1016/j.icheatmasstransfer.2012.06.015

[13] Chen S-C., Hsu P-S., Hwang S-S.: The effects of gas counter pressure and mold temperature variation on the surface quality and morphology of the microcellular polystyrene foams. Journal of Applied Polymer Science, **127**, 4769–4776 (2013).
DOI: 10.1002/app.37994

[14] Spörrer A. N. J., Altstädt V.: Controlling morphology of injection molded structural foams by mold design and processing parameters. Journal of Cellular Plastics, **43**, 313–330 (2007).
DOI: 10.1177/0021955X07079043

[15] Stumpf M., Spörrer A., Schmidt H. W., Altstädt V.: Influence of supramolecular additives on foam morphology of injection-molded i-PP. Journal of Cellular Plastics, **47**, 519–534 (2011).
DOI: 10.1177/0021955X11408769

[16] Ameli A., Nofar M., Wang S., Park C. B.: Lightweight polypropylene/stainless-steel fiber composite foams with low percolation for efficient electromagnetic interference shielding. ACS Applied Materials and Interfaces, **6**, 11091–11100 (2014).
DOI: 10.1021/am500445g

[17] Ameli A., Nofar M., Park C. B., Pötschke P., Rizvi G.: Polypropylene/carbon nanotube nano/microcellular structures with high dielectric permittivity, low dielectric loss, and low percolation threshold. Carbon, **71**, 206–217 (2014).
DOI: 10.1016/j.carbon.2014.01.031

[18] Nofar M., Park C. B.: Poly (lactic acid) foaming. Progress in Polymer Science, **39**, 1721–1741 (2014).
DOI: 10.1016/j.progpolymsci.2014.04.001

[19] Fathi S., Behravesh A. H.: Visualization analysis of flow behavior during weld-line formation in injection molding process. Polymer-Plastics Technology and Engineering, **47**, 666–672 (2008).
DOI: 10.1080/03602550802129536

[20] Yokoi H., Masuda N., Mitsuhata H.: Visualization analysis of flow front behavior during filling process of injection mold cavity by two-axis tracking system. Journal of Materials Processing Technology, **130–131**, 328–333 (2002).
DOI: 10.1016/S0924-0136(02)00742-2

[21] Leung S. N., Park C. B., Xu D., Li H., Fenton R. G.: Computer simulation of bubble-growth phenomena in foaming. Industrial and Engineering Chemistry Research, **45**, 7823–7831 (2006).
DOI: 10.1021/ie060295a

[22] Ameli A., Nofar M., Jahani D., Rizvi G., Park C. B.: Development of high void fraction polylactide composite foams using injection molding: Crystallization and foaming behaviors. Chemical Engineering Journal, **262**, 78–87 (2015).
DOI: 10.1016/j.cej.2014.09.087

eXPRESS Polymer Letters Vol.10, No.6 (2016) 470–478
Available online at www.expresspolymlett.com
DOI: 10.3144/expresspolymlett.2016.45

A facile strategy for the reduction of graphene oxide and its effect on thermal conductivity of epoxy based composites

F. Xie, S. H. Qi[*]*, D. Wu*

Department of Applied Chemistry, School of Science, Northwestern Polytechnical University, 710072 Xi'an, China

Received 16 October 2015; accepted in revised form 30 December 2015

Abstract. A facile and efficient approach to reduce graphene oxide with Al particles and potassium hydroxide was developed at moderate temperature and the graphene/epoxy composite was prepared by mould casting method. The as-prepared graphene has been confirmed by Transmission electron microscopy, Fourier transform infrared spectrometer, Raman spectroscopy, X-ray diffraction, X-ray photoelectron spectroscopy and Thermal gravimetric analysis. This provides a new green way to synthesize graphene with high surface area and opens another opportunity for the production of graphene. Effects of graphene on thermal conductivity, thermal stability and microstructures of the epoxy-based composite were also investigated. The results showed that thermal conductivity of the composite exhibited a remarkable improvement with increasing content of graphene and thermal conductivity could reach 1.192 W/(m·K) when filled with 3 wt% graphene. Moreover, graphene/epoxy composite exhibits good thermal stability with 3 wt% graphene.

Keywords: *polymer composites, oxidation, graphene, graphene oxide, thermal conductivity*

1. Introduction

Epoxy resin has gained broad attention in various occasions such as printed circuit board, heat exchanger, thermal interface material [1] due to its good adhesion, corrosion resistance, mechanical properties, chemical stability, electrical insulation, low shrinkage and easy processing etc. [2, 3]. However, brittleness [4, 5] and low intrinsic thermal conductivity of epoxy based composites limit their potential applications. With further miniaturization of microelectronics, thermal conductivity of polymer material could not meet the requirement of desirable thermal conductance in some special cases [6]. Moreover, integration of transistors has resulted in the escalation of power dissipation as well as an increase in heat flux on the devices. In general, the lifespan of high performance device depends on the heat dissipation capability to some extent [7, 8]. Therefore, it is essential for the heat generated from the devices to dissipate as effectively as possible. Many ceramic fillers with high thermal conductivity, such as aluminum nitride [9–12], alumina [13, 14], boron nitride [15] and silicon nitride [16] have been reported to improve the thermal conductivity of polymers. Although many researches have been focused on this issue, it still remains unsolved plus some restrictions such as high loading amount and the poor adhesion between filler and matrix.

Graphene emerges as a fascinating material in many technical applications like electronic [17], capacitor [18] and sensor [19] due to its extraordinary electric, thermal and mechanical properties and can be a desirable candidate as thermally conductive filler. Many different approaches for the preparation of graphene have been reported [20–22]. However, the large-scale fabrication of graphene is still a great challenge, which restricts its further applications. Kim *et al*. [20] reported a large-scale pattern growth

[*]Corresponding author, e-mail: qishuhuanwpu@163.com

of graphene films for stretchable transparent electrodes via chemical vapor deposition (CVD) on thin nickel layers and Li [21] grew large-area graphene on copper substrates by CVD using methane. However these approaches have not been expanded broadly because of the high cost and complicated preparation technology. Chemical reduction [23, 24] of graphene oxide (OG) is also considered as an efficient technique to produce graphene on a large scale in spite of its unclear mechanism. Unfortunately, commonly used chemical method is complicated and the reducing agents such as hydrazine [25], sodium borohydride [26], hydroquinone and dimethylhydrazine [27] are hazardous. Besides, some non-carbon impurities can be inevitably introduced into the graphene due to the remaining oxygen atoms. Therefore, a green and efficient method to produce graphene is urgently needed.

Herein, a facile approach is developed to get reduced graphene oxide (RGO) by chemical reduction of OG, which can be conducted using aluminum powder as the reducing agent under alkaline conditions. This approach provides enhanced reducing strength compared with the previous work of Xiaobin [28] and Zhuangjun [29]. Moreover, the obtained graphene suspension is stable within several weeks. Effects of graphene on thermal conductivity, thermal stability and microstructures of the RGO/epoxy composite were also investigated.

2. Experimental

2.1. Materials

As-received purified natural graphite was supplied by Qingdao Zhong Tian Company. Epoxy resin utilized in this study was a nominally difunctional epoxy resin, bisphenol-A glycidol ether epoxy resin (DGEBA) with an epoxy equivalent of 196 and an average molecular weight of 300 to 400, which was supplied by Lan Xing New Material Wuxi Resin Co. 2-ethyl-4-methylimidazole (EMI-2, 4) served as a curing agent and was provided by Sino pharm Chemical Reagent Co., Ltd. Acetone, potassium hydroxide (KOH) and hydrochloric acid (HCl) were received from Tianjin Fu Yu Fine Chemical Co., Ltd. Concentrated sulfuric acid (H_2SO_4, AR, 96~98%) was purchased from Daxing District Industrial. Potassium permanganate ($KMnO_4$) and hydrogen peroxide (H_2O_2) were supplied by West Long Chemical Co., Ltd. Shantou. Aluminum powder with a diameter of 8~10 μm was purchased from Henan Yuanyang Aluminum industry Co., Ltd. The reagents and materials were directly used without further purification unless otherwise indicated.

2.2. Chemical reduction of OG

The OG was prepared by modified Hummers' method [30, 31] with purified natural graphite. Typically, OG suspension was obtained by dispersing the as-prepared OG in distilled water with a concentration of 2 mg/mL under intensive sonication for 1 h. The reduction was carried out in water bath at 70 °C for 30 min with mild sonication by adding 5 mg aluminum powder and 6 M potassium hydroxide. Subsequently, the original brown suspension turned black after heated to the desired temperature. Finally, 0.5 M hydrochloric acid was added to neutralize excess alkali. The schematic illustration of the reduction procedure is shown in Figure 1.

2.3. Preparation of RGO/epoxy composites

The as-prepared RGO was dispersed in acetone under an ultra sonicator bath for 30 min. The dispersion was mixed with DGEBA and the ratio of RGO/DGEBA mixture was adjusted for different content of RGO. The mixture was placed in a warm sonicator bath at 65 °C until most of the solvents were removed. Subsequently, appropriate amount of curing agent was added. The mixture was stirred for a while to get good homogeneity and accelerate the evaporation of acetone, then placed at 60 °C for continuous vacuum in order to completely remove the solvent and get rid of air bubbles. Finally, the mixture was slowly poured into a mould and the whole system was placed in an oven. The RGO/epoxy composites were fabricated by curing the mixture at 70 °C for 3 h, then 110 °C for 1 h and at 150 °C for 3 h.

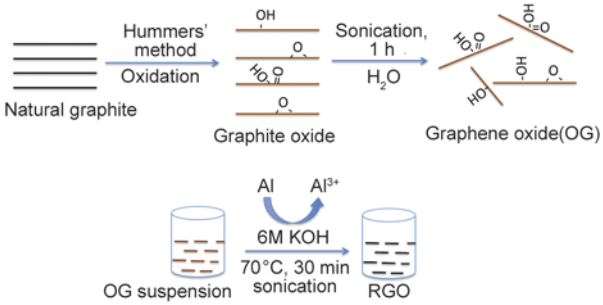

Figure 1. Schematic illustration of the preparation of RGO under alkali condition

2.4. Instrumental analysis

Infrared Spectra were obtained using a WQF-310 type Fourier transform infrared (FT-IR) spectrometer manufactured by Beijing Second Optical Instrument Factory. The RGO samples were ground into powder, and then made into KBr tablet. The spectrum was collected in a range from 4000 to 400 cm^{-1}. The resolution of apparatus was 4 cm^{-1} and the number of scans was 16 times. The as-prepared samples were characterized by Raman spectra (HR 800) and X-ray photoelectron spectra (XPS; PHI5300, Perkin-Elmer) for structure characterization and element analysis. The phase structures of OG and RGO were detected by X-ray powder diffraction (XRD; X'Pert Pro model, Holland) with a scan rate of 5°/min. The X-ray patterns from 10 to 80° were obtained. Transmission electron microscopy (TEM) was taken on H800-type (Hitachi Co.) to characterize the microstructures of OG and RGO. Thermal conductivity was conducted by employing a Hot Disk thermal analyzer (Hot Disk AB, Uppsala/Sweden) using transient place source (TPS) method. A disk-shaped TPS sensor with a diameter of 7 mm and a thickness of 0.07 mm was placed between two circular sam-

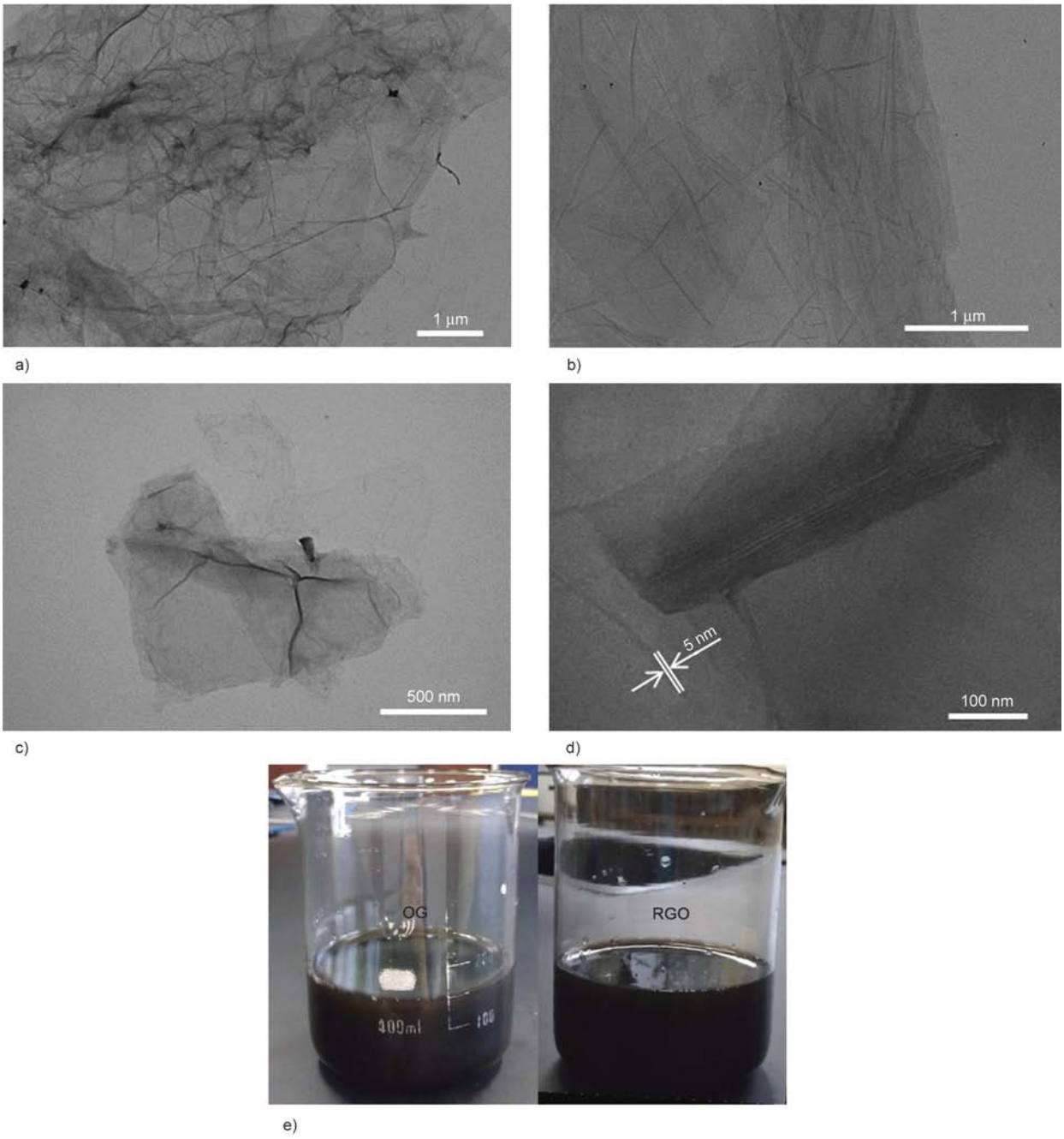

Figure 2. TEM micrographs of RGO under different magnification (a~d). Photographs of OG and RGO dispersion solution (e)

ple pieces with diameters of 20 mm and thicknesses of 2 mm. The upper surface and lower surface were polished with fine sand paper prior to use. The morphology was observed using a field emission scanning electron microscope (FESEM) (JSM-6360LV, Japan).

3. Results and discussion

3.1. TEM analysis of RGO

TEM images of RGO under different magnification are shown in Figure 2a, 2d). It can be observed from Figures 2a and 2b that the crumpled silk waves of graphene sheets possess large surface areas. Some graphene sheets fold and crinkle at some places, which can be seen in Figures 2c and 2d. Moreover, the as-prepared RGO is mostly monolayer while some multiple-layered graphene also exist, the thickness of which ranges from 5 to 50 nm (Figure 2d). The multiple-layered graphene should also exfoliate to monolayer as it experiences further ultrasonic treatment and agitation during the preparation. During the reduction process, a large amount of hydrogen bubbles were produced and the yellow-brown graphite oxide suspension gradually turned black, which are indicative of successfully deoxygenation of graphite oxide. The as-prepared RGO is very stable in water within several weeks, which can be seen in Figure 2e.

3.2. Structural characterization of OG and RGO

FTIR spectra shown in Figure 3a confirm the oxidation of graphite and identify specific functional group indicating the successful reduction of OG. A broad and intense peak centered at 3375 cm^{-1} from the spectrum of OG is attributed to the stretching vibration of –OH group. The peak around 1608 cm^{-1} is associated with vibration of absorbed water molecule [32] and also somewhat attributed to the skeletal vibrations of non-oxidized graphitic domains [33]. The characteristic peak at 1716 cm^{-1} is attributed to the stretching vibration of C=O bond in –COOH group. The signal at 1037 cm^{-1} is assigned to the stretching vibration absorption of the C–O–C bond. After deoxidization, the characteristic peaks of C=O bond and C–O–C bond disappeared. Moreover, the absorption peak of –OH group became weak and narrow and the peak around 1620 cm^{-1} decreased, indicating most of the oxygen-containing functional groups of OG were successfully deoxidized.

The structural changes of OG after reduction can also be reflected in the Raman spectra shown in Fig-

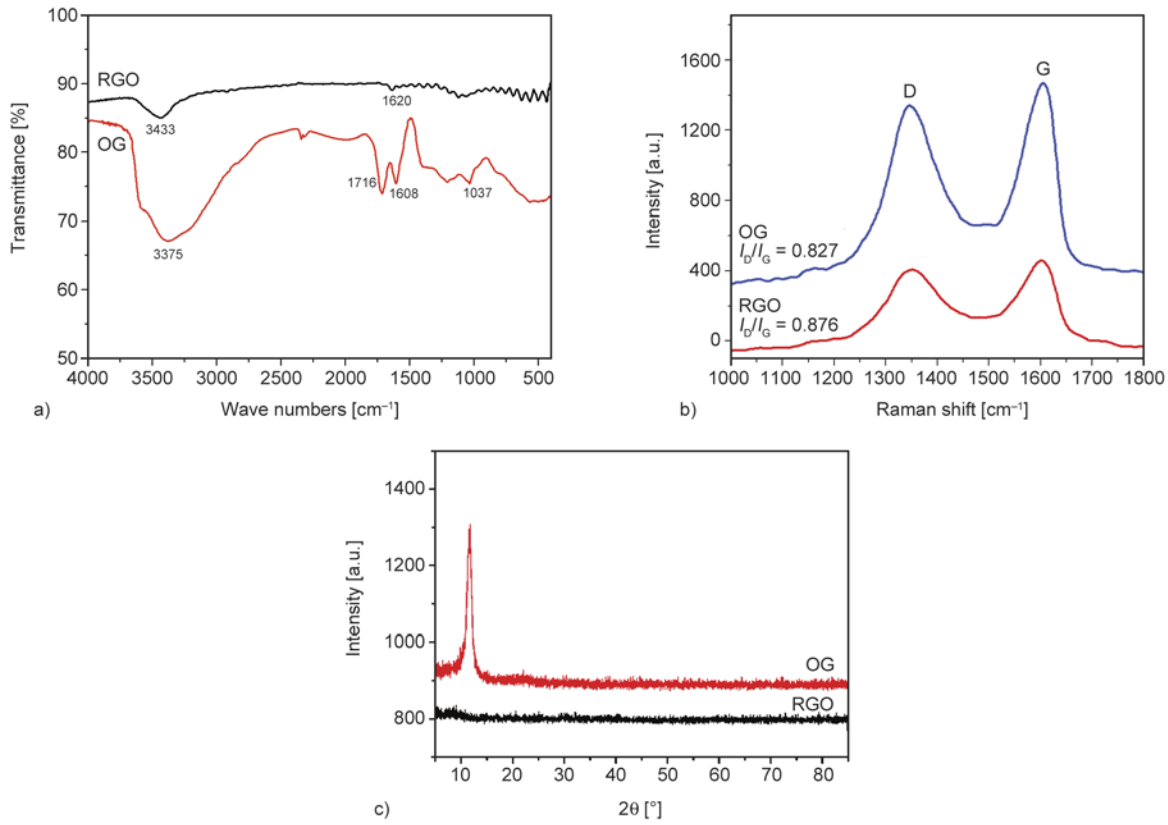

Figure 3. FT-IR spectra (a), Raman spectra (b), XRD patterns (c) of OG and RGO

ure 3b. I_D/I_G ratio can be used to qualitatively characterize the change of defects in the carbon materials. The intensity ratio (I_D/I_G) for OG was slightly increased after reduction. The reason may be that a decrease in the average size of the sp^2 domains upon the reduction of OG, indicating the formation of some sp^3 carbon after acid oxidation. The underlying mechanism is still unclear. The intensity ratio (I_D/I_G) of the *D* bond and *G* bond of OG is about 0.827, while the ratio of RGO is 0.876. This I_D/I_G ratio is consistent with the results reported by other researchers [34]. *D* band of RGO becomes stronger and broader, indicating that a higher level of disorder of the graphene layers and defects were introduced. XRD is used to further study the changes in structure. The XRD patterns shown in Figure 3c indicate that OG has a larger interlayer distance (2θ = 10.3) from (001) due to the formation of hydroxyl, epoxy, and carboxyl groups. After reduction, the interlayer distance decreases due to the removal of some oxygen-containing functional groups, which means that the sp^2 carbon is reestablished during the reduction. This can be explained by the ring-opening reaction of the epoxides. The complete disappearance of the native graphite XRD peaks in the pattern of the obtained graphene supports its single sheet nature.

3.3. XPS characterization and TGA analysis

The chemical compositions of OG and RGO were investigated by XPS. The XPS survey is presented in Figure 4a and high-resolution C1s spectra of OG and RGO were shown in Figure 4b and Figure 4c, respectively. The survey clearly revealed that the intensity of O1s peak of RGO decreased obviously as compared to that of OG, suggesting the ratio of C/O increased remarkably after chemical reduction. That is to say, the majority of oxygen-containing functional groups were successfully removed. The increased C=C peak at 284.8 eV and decreased signal intensity of C–O at 286.9 eV in C1s XPS spectrum of RGO further indicate the reduction of graphite oxide and formation of graphene.

Thermal stabilities of OG and RGO are investigated by TGA and the result is shown in Figure 4d. OG is thermally unstable and starts to lose mass upon heating even below 100 °C. There is a sharp weight loss at approximately 200 °C, which is caused by the decomposition of oxygen-containing functional groups into CO, CO_2, water vapor and so on. Hence,

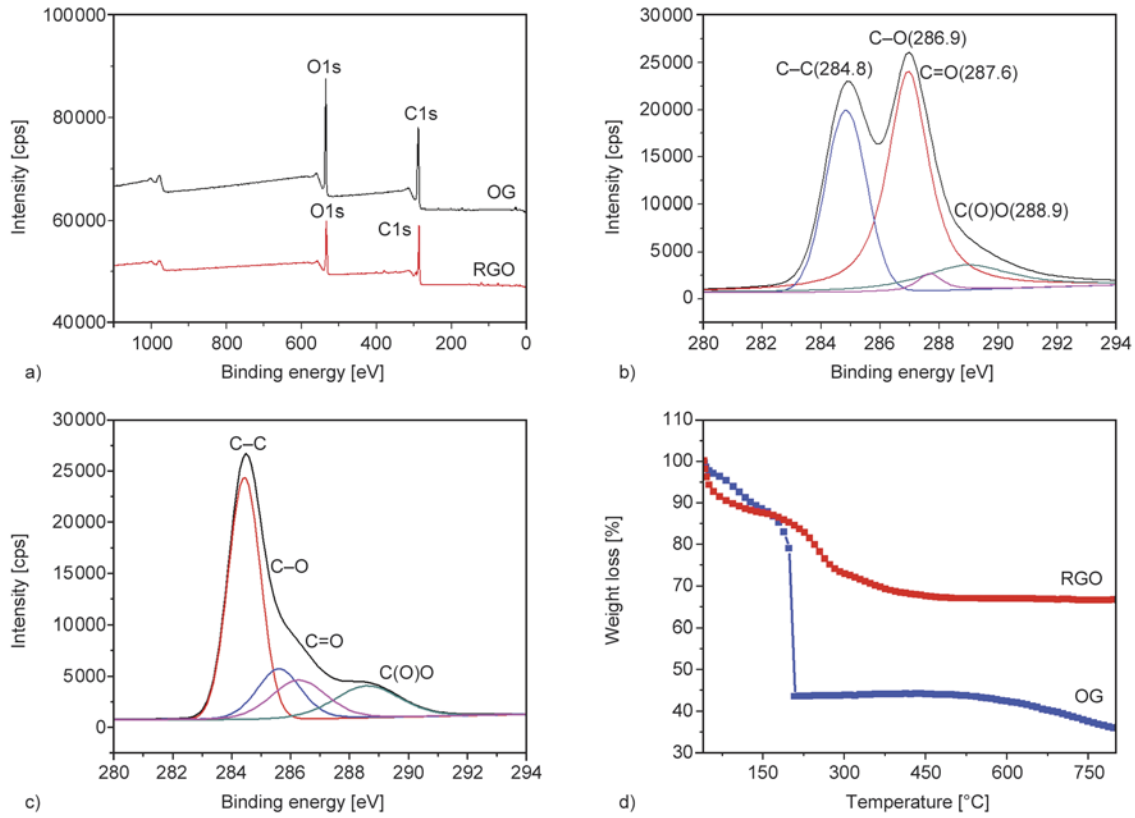

Figure 4. XPS spectra and TGA curves of OG and RGO. XPS Survey (a), high resolution C1s region of OG (b) and RGO (c), TGA curves (d).

the thermal decomposition of OG is accompanied by a vigorous release of gas, resulting in a rapid thermal expansion of the material, which is revealed in the curve. After reduction, thermal stability of RGO increased due to the removal of thermally labile oxygen-containing functional groups, indicative of the successful reduction process. Besides, no significant weight loss can be found after heated up to 800 °C.

3.4. Thermal properties and microstructure of RGO/epoxy composites

Figure 5a shows that with the increasing content of RGO, there is a significant increase in thermal conductivity of the RGO/epoxy composites. This is because that adding the fillers could form a thermal conductive network path. Furthermore, higher filler content could form more conductive paths thus increasing the heat flow of the surface [35, 36]. Thermal conductivity is affected by the filler structure, loading, and dispersion. Besides, the interfacial physical contact between polymer and filler is also very critical since phonons are very sensitive to surface defects. Previously, we did some research on the amino-functionalized MWCNT/epoxy composites in order to decrease the interfacial barrier [37]. The thermal conductivity of MWCNT/epoxy composites is significantly increased. However, the process is a little more complicated than our method reported here. The as-prepared RGO possesses higher surface area and can connect with the epoxy adequately, which reduces the barriers of phonon transport to a large extent. Moreover, the excellent solubility of RGO facilitates its dispersion in polymer composites, resulting in an increased contact surface area between RGO and epoxy matrix. Accordingly, it can facilitate the heat flows and promote phonon diffusion in RGO/epoxy composites.

As can be seen in Figure 5a, thermal conductivity of RGO/epoxy composite is almost the same as that of amino-functionalized MWCNT/epoxy composite. By contrast, thermal conductivity of composite with RGO by common hydrazine reduction was a little bit lower than that of RGO/epoxy composite acquired by our method, which is also shown in Figure 5a. RGO/epoxy composites prepared by this method exhibit the best efficiency in improving thermal conductivity, compared with those filled with ordinary graphene or OG [38]. It was noticeable that thermal conductivity of RGO/epoxy composite increased

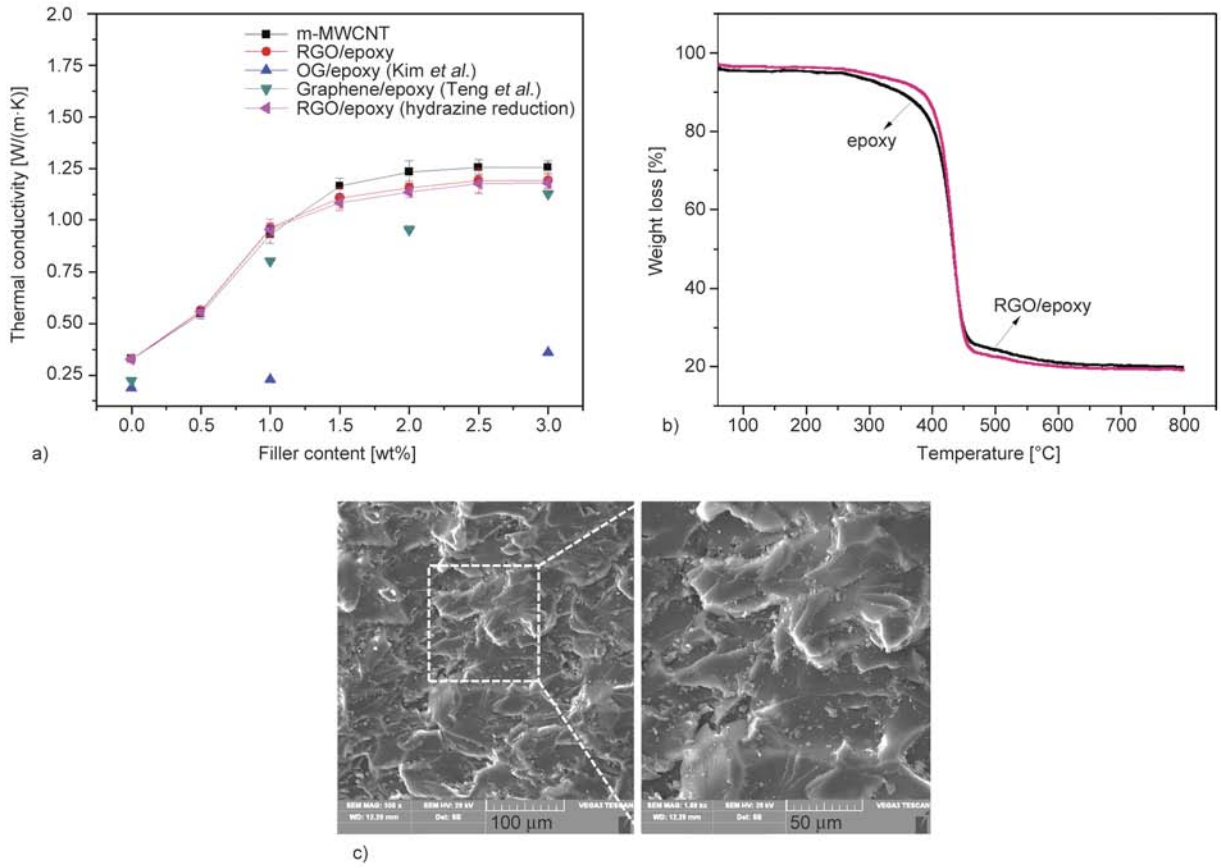

Figure 5. Thermal conductivity (a), thermal stability (b), and cross-section images (c) of epoxy-based composites

significantly and reached 1.192 W/(m·K) when filled with 3 wt% RGO, higher than that of OG/epoxy with the same weight percentage (Figure 5a) by Kim *et al.* [39]. In general, 40~50 wt% ceramic fillers is required to achieve the comparable thermal conductivity. As is also indicated in Figure 5a, the thermal conductivity of epoxy resin system increases obviously with increasing filler content up to 1 wt%. After that, it tends to increase slower. This can be explained by the established percolation theory [40].

Thermal stability of RGO/epoxy composite with a filler content of 3 wt% is shown in Figure 5b. The initial thermal decomposition temperature of pure epoxy is 348 °C. Compared to the pure epoxy resin, the initial thermal decomposition temperature of RGO/epoxy composite increased about 40 °C. Thermal stability of RGO/epoxy composite not only depends on thermal stability of RGO itself, but also relates to the dispersion of RGO in matrix and the interaction between them. If agglomeration of RGO exists, the relatively poor dispersion could make some defects in the epoxy matrix, which will reduce the initial decomposition temperature of the composites. Besides, the good interfacial affinity between RGO and matrix could delay the volatilization of small molecules at high temperature, thus increasing the thermal stability of the composites.

Cross-section SEM images of the RGO/epoxy composite can be seen in Figure 5c. No aggregations can be observed in the SEM images, indicating that RGO is uniformly dispersed in the epoxy resin. RGO is not easily observed in epoxy matrix even under higher magnification, while cracks in cross section of the composites verified that the adhesion between the filler and matrix is strong enough. The cross section of pure epoxy should be smooth and the crack is uniform and orderly [39]. The introduction of RGO can prevent rapid expansion of macroscopic crack in matrix and cracks become disordered and consume a part of the energy when subjected to external forces. Overall, the as-prepared RGO can homogeneously disperse in the epoxy matrix and the results show good interfacial affinity between RGO and epoxy matrix, which are consistent with the results of the thermal conductivity.

4. Conclusions

In conclusion, the exfoliated OG undergoes quick de-oxygenation process by aluminum in alkali solutions at moderate temperature. This provides a new facile way to synthesize graphene with large surface area and opens another opportunity for the production of graphene. Results from TEM, FT-IR, Raman, XRD, XPS and TGA analysis demonstrate that RGO is successfully prepared by this new method, although the reduction mechanism is still not clear enough. What's more, RGO/epoxy composite exhibits remarkable improvement of thermal conductivity. The thermal conductivity of RGO/epoxy composite increased significantly and reached 1.192 W/(m·K) when filled with 3 wt% RGO. The initial thermal decomposition temperature of RGO/epoxy composite is improved compared with pure epoxy resin from TGA analysis and the microstructure images further verify the good interfacial affinity between RGO and epoxy matrix.

Acknowledgements

The authors would like to express their deepest acknowledgement to Prof. Zhang for her continuous encouragement and help to facilitate this work. Authors also appreciate Northwestern Polytechnical University for its support as well as the companies and relatives who friendly offered the materials and help.

References

[1] Yu A., Ramesh P., Sun X., Bekyarova E., Itkis M. E., Haddon R. C.: Enhanced thermal conductivity in a hybrid graphite nanoplatelet – Carbon nanotube filler for epoxy composites. Advanced Materials, **20**, 4740–4744 (2008).
DOI: 10.1002/adma.200800401

[2] Teng C-C., Ma C-C. M., Chiou K-C., Lee T-M., Shih Y-F.: Synergetic effect of hybrid boron nitride and multi-walled carbon nanotubes on the thermal conductivity of epoxy composites. Materials Chemistry and Physics, **126**, 722–728 (2011).
DOI: 10.1016/j.matchemphys.2010.12.053

[3] Suriati G., Mariatti M., Azizan A.: Effects of filler shape and size on the properties of silver filled epoxy composite for electronic applications. Journal of Materials Science: Materials in Electronics, **22**, 56–63 (2011).
DOI: 10.1007/s10854-010-0082-2

[4] Özarslan Ö., Yildiz E., İnan T. Y., Kuyulu A., Güngör A.: Novel amine terminated elastomeric oligomers and their effects on properties of epoxy resins as a toughener. Journal of Applied Polymer Science, **115**, 37–45 (2010).
DOI: 10.1002/app.29693

[5] Luo Y., Zhang M., Dang G., Li Y., An X., Chen C., Yi X.: Toughening of epoxy resin by poly(ether ether ketone) with pendant fluorocarbon groups. Journal of Applied Polymer Science, **122**, 1758–1765 (2011).
DOI: 10.1002/app.34292

[6] Lee G-W., Park M., Kim J., Lee J. I., Yoon H. G.: Enhanced thermal conductivity of polymer composites filled with hybrid filler. Composites Part A: Applied Science and Manufacturing, **37**, 727–734 (2006). DOI: 10.1016/j.compositesa.2005.07.006

[7] Sim L. C., Ramanan S. R., Ismail H., Seetharamu K. N., Goh T. J.: Thermal characterization of Al_2O_3 and ZnO reinforced silicone rubber as thermal pads for heat dissipation purposes. Thermochimica Acta, **430**, 155–165 (2005). DOI: 10.1016/j.tca.2004.12.024

[8] Zhou W., Qi S., Tu C., Zhao H., Wang C., Kou J.: Effect of the particle size of Al_2O_3 on the properties of filled heat-conductive silicone rubber. Journal of Applied Polymer Science, **104**, 1312–1318 (2007). DOI: 10.1002/app.25789

[9] Gu J., Zhang Q., Dang J., Zhang J., Yang Z.: Thermal conductivity and mechanical properties of aluminum nitride filled linear low-density polyethylene composites. Polymer Engineering and Science, **49**, 1030–1034 (2009). DOI: 10.1002/pen.21336

[10] Peng W., Huang X., Yu J., Jiang P., Liu W.: Electrical and thermophysical properties of epoxy/aluminum nitride nanocomposites: Effects of nanoparticle surface modification. Composites Part A: Applied Science and Manufacturing, **41**, 1201–1209 (2010). DOI: 10.1016/j.compositesa.2010.05.002

[11] Bae J-W., Kim W., Cho S-H., Lee S-H.: The properties of AlN-filled epoxy molding compounds by the effects of filler size distribution. Journal of Materials Science, **35**, 5907–5913 (2000). DOI: 10.1023/A:1026741300020

[12] Teng C-C., Ma C-C. M., Chiou K-C., Lee T-M.: Synergetic effect of thermal conductive properties of epoxy composites containing functionalized multi-walled carbon nanotubes and aluminum nitride. Composites Part B: Engineering, **43**, 265–271 (2012). DOI: 10.1016/j.compositesb.2011.05.027

[13] Mcgrath L. M., Parnas R. S., King S. H., Schroeder J. L., Fischer D. A., Lenhart J. L.: Investigation of the thermal, mechanical, and fracture properties of alumina–epoxy composites. Polymer, **49**, 999–1014 (2008). DOI: 10.1016/j.polymer.2007.12.014

[14] Im H., Kim J.: Enhancement of the thermal conductivity of aluminum oxide–epoxy terminated poly(dimethyl siloxane) with a metal oxide containing polysiloxane. Journal of Materials Science, **46**, 6571–6580 (2011). DOI: 10.1007/s10853-011-5604-7

[15] Zhou W., Qi S., An Q., Zhao H., Liu N.: Thermal conductivity of boron nitride reinforced polyethylene composites. Materials Research Bulletin, **42**, 1863–1873 (2007). DOI: 10.1016/j.materresbull.2006.11.047

[16] He H., Fu R., Shen Y., Han Y., Song X.: Preparation and properties of Si_3N_4/PS composites used for electronic packaging. Composites Science and Technology, **67**, 2493–2499 (2007). DOI: 10.1016/j.compscitech.2006.12.014

[17] Eda G., Fanchini G., Chhowalla M.: Large-area ultrathin films of reduced graphene oxide as a transparent and flexible electronic material. Nature Nanotechnology, **3**, 270–274 (2008). DOI: 10.1038/nnano.2008.83

[18] Miller J. R., Outlaw R. A., Holloway B. C.: Graphene double-layer capacitor with ac line-filtering performance. Science, **329**, 1637–1639 (2010). DOI: 10.1126/science.1194372

[19] Lu C-H., Yang H-H., Zhu C-L., Chen X., Chen G-N.: A graphene platform for sensing biomolecules. Angewandte Chemie, **121**, 4879–4881 (2009). DOI: 10.1002/anie.200901479

[20] Kim K. S., Zhao Y., Jang H., Lee S. Y., Kim J. M., Kim K. S., Ahn J. H., Kim P., Choi J. Y., Hong B. H.: Large-scale pattern growth of graphene films for stretchable transparent electrodes. Nature, 457, 706-710 (2009). DOI: 10.1038/nature07719

[21] Li X., Cai W., An J., Kim S., Nah J., Yang D., Piner R., Velamakanni A., Jung I., Tutuc E., Banerjee S. K., Colombo L., Ruoff R. S.: Large-area synthesis of high-quality and uniform graphene films on copper foils. Science, **324**, 1312–1314 (2009). DOI: 10.1126/science.1171245

[22] Xu C., Wang X., Zhu J.: Graphene–metal particle nanocomposites. Journal of Physical Chemistry C, **112**, 19841–19845 (2008). DOI: 10.1021/jp807989b

[23] Chen W., Yan L.: *In situ* self-assembly of mild chemical reduction graphene for three-dimensional architectures. Nanoscale, **3**, 3132–3137 (2011). DOI: 10.1039/c1nr10355e

[24] Compton O. C., Dikin D. A., Putz K. W., Brinson L. C., Nguyen S. T.: Electrically conductive 'alkylated' graphene paper via chemical reduction of amine-functionalized graphene oxide paper. Advanced Materials, **22**, 892–896 (2010). DOI: 10.1002/adma.200902069

[25] Park S., An J., Potts J. R., Velamakanni A., Murali S., Ruoff R. S.: Hydrazine-reduction of graphite- and graphene oxide. Carbon, **49**, 3019–3023 (2011). DOI: 10.1016/j.carbon.2011.02.071

[26] Shin H-J., Kim K. K., Benayad A., Yoon S-M., Park H. K., Jung I-S., Jin M. H., Jeong H-K., Kim J. M., Choi J-Y., Lee Y. H.: Efficient reduction of graphite oxide by sodium borohydride and its effect on electrical conductance. Advanced Functional Materials, **19**, 1987–1992 (2009). DOI: 10.1002/adfm.200900167

[27] Stankovich S., Dikin D. A., Dommett G. H. B., Kohlhaas K. M., Zimney E. J., Stach E. A., Piner R. D., Nguyen S. T., Ruoff R. S.: Graphene-based composite materials. Nature, **442**, 282–286 (2006).
DOI: 10.1038/nature04969

[28] Fan X., Peng W., Li Y., Li X., Wang S., Zhang G., Zhang F.: Deoxygenation of exfoliated graphite oxide under alkaline conditions: A green route to graphene preparation. Advanced Materials, **20**, 4490–4493 (2008).
DOI: 10.1002/adma.200801306

[29] Fan Z., Wang K., Wei T., Yan J., Song L., Shao B.: An environmentally friendly and efficient route for the reduction of graphene oxide by aluminum powder. Carbon, **48**, 1686–1689 (2010).
DOI: 10.1016/j.carbon.2009.12.063

[30] Hummers W. S., Offeman R. E.: Preparation of graphitic oxide. Journal of the American Chemical Society, **80**, 1339 (1958).
DOI: 10.1021/ja01539a017

[31] Shen J., Hu Y., Li C., Qin C., Ye M.: Synthesis of amphiphilic graphene nanoplatelets. Small, **5**, 82–85 (2009).
DOI: 10.1002/smll.200800988

[32] Szabó T., Berkesi O., Dékány I.: Drift study of deuterium-exchanged graphite oxide. Carbon, **43**, 3186–3189 (2005).
DOI: 10.1016/j.carbon.2005.07.013

[33] Chen C., Yang Q-H., Yang Y., Lv W., Wen Y., Hou P-X., Wang M., Cheng H-M.: Self-assembled free-standing graphite oxide membrane. Advanced Materials, **21**, 3007–3011 (2009).
DOI: 10.1002/adma.200990138

[34] Yang D., Velamakanni A., Bozoklu G., Park S., Stoller M., Piner R. D., Stankovich S., Jung I., Field D. A., Ventrice C. A., Ruoff R. S.: Chemical analysis of graphene oxide films after heat and chemical treatments by X-ray photoelectron and micro-raman spectroscopy. Carbon, **47**, 145–152 (2009).
DOI: 10.1016/j.carbon.2008.09.045

[35] Li T-L., Hsu S-L. C.: Enhanced thermal conductivity of polyimide films *via* a hybrid of micro- and nano-sized boron nitride. Journal of Physical Chemistry B, **114**, 6825–6829 (2010).
DOI: 10.1021/jp101857w

[36] Zhou T., Wang X., Liu X., Xiong D.: Improved thermal conductivity of epoxy composites using a hybrid multiwalled carbon nanotube/micro-SiC filler. Carbon, **48**, 1171–1176 (2010).
DOI: 10.1016/j.carbon.2009.11.040

[37] Xie F., Qi S., Yang R., Wu D.: High thermal conductive m-xylylenediamine functionalized multiwall carbon nanotubes/epoxy resin composites. Journal of Applied Polymer Science, **132**, 41255/1–41255/6 (2015).
DOI: 10.1002/APP.41255

[38] Teng C-C., Ma C-C. M., Lu C-H., Yang S-Y., Lee S-H., Hsiao M-C., Yen M-Y., Chiou K-C., Lee T-M.: Thermal conductivity and structure of non-covalent functionalized graphene/epoxy composites. Carbon, **49**, 5107–5116 (2011).
DOI: 10.1016/j.carbon.2011.06.095

[39] Kim J., Yim B-S., Kim J-M., Kim J.: The effects of functionalized graphene nanosheets on the thermal and mechanical properties of epoxy composites for anisotropic conductive adhesives (ACAS). Microelectronics Reliability, **52**, 595–602 (2012).
DOI: 10.1016/j.microrel.2011.11.002

[40] Shante V. K. S., Kirkpatrick S.: An introduction to percolation theory. Advances in Physics, **20**, 325–357 (1971).
DOI: 10.1080/00018737100101261

eXPRESS Polymer Letters Vol.10, No.6 (2016) 479–492
Available online at www.expresspolymlett.com
DOI: 10.3144/expresspolymlett.2016.46

Solvent free synthesis and structural evaluation of polyurethane films based on poly(ethylene glycol) and poly(caprolactone)

V. Kupka[1*], *L. Vojtova*[1,3], *Z. Fohlerova*[1], *J. Jancar*[1,2,3]

[1]CEITEC – Central European Institute of Technology, Brno University of Technology, Technicka 3058/10, 616 00 Brno, Czech Republic
[2]Institute of Materials Chemistry, Faculty of Chemistry, Brno University of Technology, Purkynova 118, 612 00 Brno, Czech Republic
[3]SCITEG a.s., Brno, Czech Republic

Received 31 October 2015; accepted in revised form 4 January 2016

Abstract. Biodegradable amphiphilic polyurethane films (bio-PUs) were synthesized by solvent free polyaddition reaction of hydrophilic poly(ethylene glycol) (PEG) and hydrophobic poly(caprolactone) (PCL) as macrodiols with hexamethylene diisocyanate. Samples were subsequently heat cured in order to obtain 3D crosslinked structure. Different PCL/PEG ratios allowed controlling the toughness of the resulting bio-PUs. Significant enhancement of Young's modulus, strength and elongation at break was observed at a PCL/PEG molar ratio above 3. The change in the bio-PU mechanical behavior was ascribed to the formation of crystalline PCL domains in the bio-PU network. The presence of PEG increased both the ability to absorb water and the rate of hydrolytic degradation, while PCL increased the cell viability. Prepared solvent free bio-PUs may advantageously be used in medicine as elastic resorbable material applicable against post-surgical adhesions.

Keywords: *biodegradable polymers, polyurethane, elastomer, poly(ethylene glycol), poly(caprolactone)*

1. Introduction

Polyurethanes (PUs) form diverse class of elastomers covering a broad range of chemical and physical properties. In addition to industrial applications, their structure can be also formed from bioresorbable materials for the use in human medicine [1–4]. Favorable parameters of PUs for the use particularly in tissue engineering are tissue-specific biocompatibility, biodegradability, mechanical flexibility and moderate blood compatibility. PUs were initially used in medicine as bio-inert, hydrolytically stable materials (e.g. ventricle assist devices or heart valves [5]). Later on, bioresorbable PUs were introduced for various tissue constructs such as vascular grafts [6], cartilage [7], cancellous bone graft substitutes [8] or as grafts for small diameter vascular replacement [9]. Moreover, bioresorbable PUs can be tailored to possess a broad range of mechanical properties by selections and content of soft and hard segments [10, 11]. Soft segments are commonly polyols represented by polyesters such as poly(ε-caprolactone) (PCL), poly (lactic acid) and poly(glycolic acid) or polyethers like poly(ethylene glycol) (PEG) and poly(propylene glycol) having a low glass transition temperature (lower than 25 °C). The hard segments are provided by the combination of the chain extender and the diisocyanate component. The nature of hydrogen bonding in the hard segment causes a mutual

*Corresponding author, e-mail: vojtech.kupka@ceitec.vutbr.cz

attraction leading to a formation of hard and soft segment domains [12]. To eliminate the concern of aromatic amine by-products, the utilization of aliphatic diisocyanates (as alternatives to aromatic ones) provide a route to synthetize biodegradable polyurethanes yielding non-toxic degradation products [3].
Generally, PUs are synthesized either by polymerization in a solvent or in bulk. Subsequently, processing of PU polymers into films is carried out by dissolving the polymer in a solvent such as dimethyl sulfoxide (DMSO) or dimethylformamide (DMF) followed by casting into a mold. A range of bioresorbable linear PU systems has already been described in the literature [13–20]. However, avoiding the use of organic solvent is a favorable parameter for a material with the potential use in medicine.
In this work, we present novel and original solvent free 'green chemistry' procedure yielding compact biodegradable cross-linked PCL/PEG bio-PU films eliminating organic solvents commonly used in PU synthesis. Polymerization conditions were optimized and the effect of PCL/PEG ratio on the prepared bio-PU structure and physical properties is discussed below.

2. Experimental

2.1. Chemicals

Poly(ε-caprolactone) diol (PCL, M_n = 530 g·mol^{-1}, Sigma-Aldrich, Germany) and poly(ethylene glycol) (PEG, M_n = 400 g·mol^{-1}, Sigma-Aldrich, Germany) were degassed at 130 °C for 3 hours before the synthesis; 1,6-diisocyanatohexane (HDI, 98%, Sigma-Aldrich, Germany) was degassed at the laboratory temperature for 3 hours. Tin(II) 2-ethylhexanoate (95%, Sigma-Aldrich, Germany) and gaseous nitrogen (99.999 %, SIAD Czech spol. s r.o.) were used as received. Dealing with wide-angle X-ray scattering (WAXS) measurements high molecular weight poly(ε-caprolactone) (PCL, M_n = 80 000 g·mol^{-1}, Sigma-Aldrich, Germany) was used due to its high crystallinity. Ultrapure water (UPW) of type II according to ISO 3696 was prepared on Elix 5 UV Water Purification System (Merck Millipore).

2.2. Synthesis

Synthesis was carried out under nitrogen atmosphere using a high vacuum manifold utilizing Schlenk's technique in combination with nitrogen flushed glove-box. Typical synthesis procedure is described below.
PCL and PEG were used as macrodiol components either alone or in the mixture under given PCL/PEG molar ratio. Both PEG and PCL were chosen with the low number average molecular weight (M_n = 400 g·mol^{-1} and M_n = 530 g·mol^{-1}, respectively), to allow easy casting of the reaction mixture into the mold at laboratory temperature. Firstly, degassed macrodiols were mixed together at the laboratory temperature for 1 hour. Consequently, 0.03 mol% of tin(II) 2-ethylhexanoate catalyst (related to moles of –OH groups in the mixture) was added followed by vigorous stirring for 1 hour to maximize dispersion of the catalyst. Finally, HDI in the molar ratio of NCO/OH = 1.2 was dosed into the diol mixture in glove-box, stirred at 250 rpm and the viscous polymer was poured into the 1 mm thick top-covered teflon® mold. The sample was left to cure overnight in the mold at room temperature followed by post-curing in the oven for 24 hours at 65 °C. Seven series of bio-PUs was prepared with varying

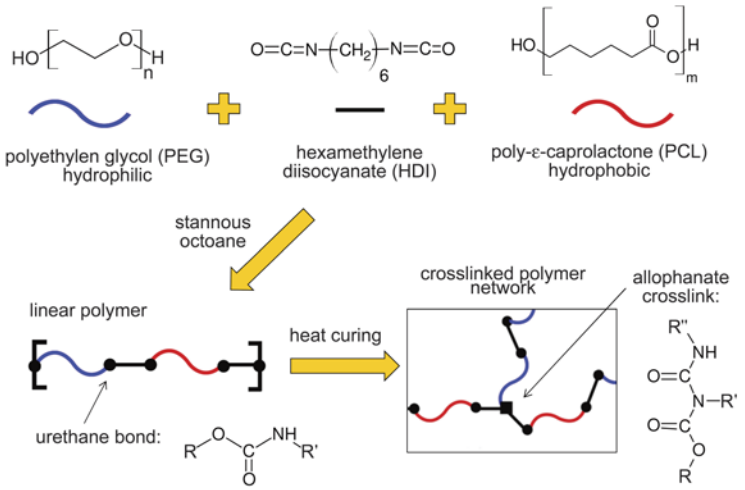

Figure 1. Procedure scheme for preparation of bio-PU films

Table 1. Composition of the prepared PU samples differing in the amount of PCL and PEG

PU sample label	Molar ratio of PCL/PEG	Weight ratio of PCL/PEG	NCO/OH ratio	Turbidity
PU_{PEG}	0/100	0/100	1.2	Transparent
$PU_{0.3}$	24/76	30/70	1.2	Transparent
$PU_{0.8}$	43/57	50/50	1.2	Transparent
$PU_{1.8}$	64/36	70/30	1.2	Transparent
$PU_{3.0}$	75/25	80/20	1.2	Translucent
$PU_{6.7}$	87/13	90/10	1.2	Translucent
PU_{PCL}	100/0	100/0	1.2	Translucent

PCL/PEG molar ratio. The scheme of the procedure is sketched in Figure 1. The composition of the prepared samples is summarized in Table 1.

2.3. Characterization methods

2.3.1. Temperature profiles acquisition

Temperature profiles were acquired by thermocouple inserted into the reaction mixture. The synthesis procedure was performed similarly to the described one in chapter 2.2. Instead of pouring the reacting mixture into the mold, the mixture was let to react until the obvious temperature decrease was recognized. Profiles were depicted for PU_{PEG} and PU_{PCL} samples. Each profile was measured twice to confirm the acquired trend. Reported results are depicted from the first measurement.

2.3.2. Ultraviolet-visible spectroscopy (UV-VIS)

Absorbance spectra were obtained using UV-VIS spectrophotometer (Jasco V-630, USA) in the interval of wavelengths from 240 to 1100 nm with resolution of 0.5 nm. Films with a thickness of 1.0±0.1 mm were placed directly into the light path and measured.

2.3.3. Attenuated total reflection infrared spectroscopy (ATR-IR)

Attenuated total reflection infrared spectroscopy (ATR-IR) was performed on Fourier-transform infrared spectrometer (Bruker Tensor 27, USA) equipped with a germanium crystal for ATR over the spectral range from 4000 to 600 cm^{-1} at the resolution of 4 cm^{-1} and 32 scans.

2.3.4. Wide-angle X-ray scattering

Wide-angle X-ray scattering (WAXS) was performed on the diffractometer (Rigaku MiniFlex 600, Japan) with Cu K_α radiation (λ = 1.5406 Å) operated at 40 kV and 15 mA and the scattering angle (2θ) ranging from 5 to 35° with the scan rate of 2°·min^{-1} with step of 0.02°. For calculating the size of crystallites according to Scherrer equation, the baseline was set as a line anchored to corresponding spectra from 15 to 30°. As a reference material, WAXS of a commercial PCL (M_n = 80 000 g·mol^{-1}) with high crystallinity was also measured.

2.3.5. Differential scanning calorimetry (DSC)

Calorimetric measurements were carried out utilizing differential scanning calorimetry (DSC) (Netzsch 204 F1, Germany) in nitrogen atmosphere. Each sample (5–10 mg) was heated first from –80 up to 100 °C with heating rate of 10 °C·min^{-1}. Raw data were processed using the NETZSCH Proteus® Software to obtain glass transition temperature (T_g), melting temperature (T_m) and melting enthalpy (ΔH_m). The crystallinity (α_c) was calculated from the first DSC heating run according to Equation (1):

$$\alpha_c\,[\,\%\,] = \frac{\Delta H_m \cdot 100}{w \cdot \Delta H_m^0} \tag{1}$$

where ΔH_m is heat of fusion of the bio-PU sample, ΔH_m^0 is heat of fusion of 100% crystalline PCL (135.44 J·g^{-1}) [21] and w is the PCL's weight fraction in the bio-PU sample.

2.3.6. Thermogravimetric analysis (TGA)

Thermal decompositions of bio-PUs were investigated using the thermogravimetric analysis (TGA) (TA Q500, USA) with sample mass in the range between 5–10 mg. All measurements were carried out in nitrogen atmosphere with a flow rate of 100 mL·min^{-1}. Heating rate was set at 10 °C·min^{-1} starting from 25 up to 750 °C.

2.3.7. Swelling

Swelling ratio of 10×10×1 mm specimens was measured in Ultrapure water (UPW) at laboratory temperature. Sample weight was measured every ten minutes within the first hour, every 20 minutes within the second hour and then every hour for the next 4 hours with the last measurement performed after 1 day since the beginning of the swelling experiment. Water uptake was calculated according to the Equation (2):

$$\text{Water uptake [\%]} = \frac{w_s - w_d}{w_d} \cdot 100 \tag{2}$$

where w_s is the weight of swollen sample at the given time and w_d is the weight of dry sample. From every sample three pieces were measured at each time point and data were expressed as mean ± standard deviation.

2.3.8. Hydrolytic degradation

Hydrolytic degradation tests employing the swelled samples were carried out in an incubator at 37 °C in UPW for 365 days. Each measurement was an average of 3 specimens and data were expressed as mean ± standard deviation. The specimens were removed at the given time from vials with UPW, wiped using filter paper and weighed to determine the weight loss. The UPW was changed every two weeks. Mass loss was calculated according to Equation (3):

$$\text{Mass loss [\%]} = \frac{w_0 - w_t}{w_0} \cdot 100 \quad (3)$$

where w_0 is the weight of swollen sample after 24 hours in water and w_t is the weight of the sample at the given time.

2.3.9. Extraction

Extraction of the bio-PU films was performed using Soxhlet apparatus. Small 10×10×1 mm pieces of dry bio-PU films were used for the extraction in dimethylformamide (DMF) and in acetone. Extractions were performed for 8 hours in 200 mL of the solvent followed by drying extracted samples in the vacuum oven at 25 °C to the constant weight. Weight loss was calculated according to Equation (4):

$$\text{Weight loss [\%]} = \frac{w_0 - w_e}{w_0} \cdot 100 \quad (4)$$

where w_0 is the weight of the sample before extraction and w_e is the weight of the sample after extraction. Extracts obtained from acetone with bio-PU dissolved residues were thickened by acetone evaporation and dried in the vacuum oven to be ATR-IR analyzed.

2.3.10. Tensile measurement

Tensile tests were performed employing a tensile tester (Zwick Roell Z010, Germany) according to the ISO 527 standard. Dog-bone specimens obtained according to ISO 527-2/5B were 35 mm in length, 2 mm in width in the middle part, 1 mm thick and gauge length was 10 mm. A 500 N load cell was used for the measurements with a cross-head speed of 10 mm·min^{-1} corresponding to a 100%·min^{-1} deformation rate. The 0.1 N preload was used and all tensile measurements were performed at the laboratory temperature. Six dog-bones were measured from each sample and data were averaged to get the standard deviation.

2.3.11. Confocal laser scanning microscopy (CLSM)

Morphology of the bio-PU films was acquired by confocal laser scanning microscope (Olympus OLS 3000 LEXT). Roughness average (R_a) was evaluated using the Olympus software. Five profiles were acquired from each sample and data were expressed as mean ± standard deviation. The length of the profile line for the R_a parameter calculation was 126 μm.

2.3.12. Contact angle measurement

Contact angle measurements were carried out on films using a contact angle apparatus (OCA 10, Dataphysics, Germany). The used liquid probe was ultrapure water. Drop of 1 μL was deposited on a bio-PU film and contact angle was acquired when steady state for angle was reached (around t = 10 s). Measurement was repeated five times on each film and data were expressed as mean ± standard deviation.

2.3.13. Cell viability evaluation

Selected samples of PU_{PEG}, $PU_{3.0}$ and PU_{PCL} films were tested for cytotoxicity by seeding human mesenchymal stem cells (MSCs) and evaluating their adhesion and viability after 24, 72 and 168 hours. Human MSCs were isolated from a fatty tissue of three healthy donors who had undergone cosmetic liposuction. Isolation of MSCs was based on the incubation of fresh lipoaspirates with collagenase and expanded in complete Dulbecco's Modified Eagle's medium with low glucose. Bio-PU 1 mm thick films in the form of 6 mm discs were sterilized using a combination of UV (15 min) and ethanol followed by incubation in culture medium (Dulbecco's Modified Eagle's medium with L-glutamine, 10% fetal bovine serum, 1% penicillin/streptomycin) overnight at 37 °C. Cells were seeded on the films at a density of $3 \cdot 10^4$ cells·cm-2 in 48-well plate. Bio-PU films with seeded MSCs were cultivated at 37 °C and 5% CO_2 atmosphere. The medium was changed every 3 days. Fluorescence microscopy and live/dead staining (calcein-AM/propidium iodide) were

used to determine cell viability acquired in 24, 72 and 168 hours after seeding. The mix of calcein-AM (2 μM) and propidium (1,5 μM) in phosphate buffered saline (PBS) was added to the cell-seeded films and incubated for 15 min at 37 °C and 5% CO_2 for live/dead cell detection. The cells were visualized using a Zeiss Axio Imager 2 microscope.

3. Results and discussion

Seven bio-PU samples with different PCL/PEG ratios were prepared in order to obtain biodegradable films applicable in regenerative medicine. Liquid low-molecular weight diols (hydrophilic PEG (M_n = 400 g·mol^{-1}) and hydrophobic PCL (M_n = 530 g·mol^{-1}) were used for polyaddition reaction with HDI without the use of any organic solvent. Important feature of the procedure was finding a proper time for pouring the reacting polymer into a mold. The mixing time was set according to acquired temperature profiles depicted in Figure 2. Rapid temperature's increase in the mixture of PEG with HDI or PCL with HDI after 90 and 140 sec, respectively, was accompanied by increase in viscosity. In order to easily pour the reacting mixture into the mold the time of mixing was set at 80 sec for all the samples.

3.1. Structural analysis

Captured images of samples in Figure 3 are showing differences in opacity. Bio-PU films having ratio PCL/PEG equal to 1.8 and lower were transparent (Figure 3a), when the molar excess of PCL was equal to 3 or higher bio-PU films became semi-transparent (Figure 3b) and samples with higher PCL's content were opaque (Figure 3c). This phenomenon was confirmed by UV-VIS measurements (see Figure 4) showing that bio-PU films having ratio PCL/PEG equal to 1.8 and lower were without significant absorption in the visible spectra from 390 to 700 nm. However, when the molar excess of

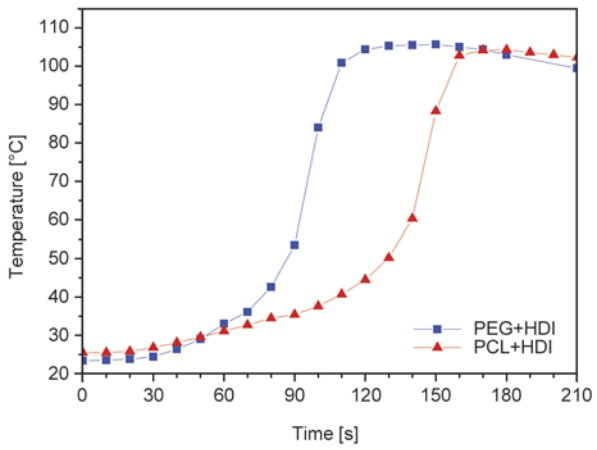

Figure 2. Temperature profiles of reaction between PEG with HDI and PCL with HDI

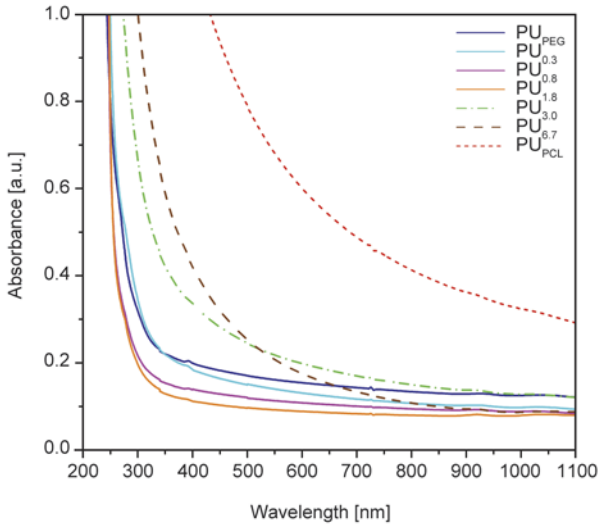

Figure 4. UV-VIS spectra showing change in opacity of bio-PUs

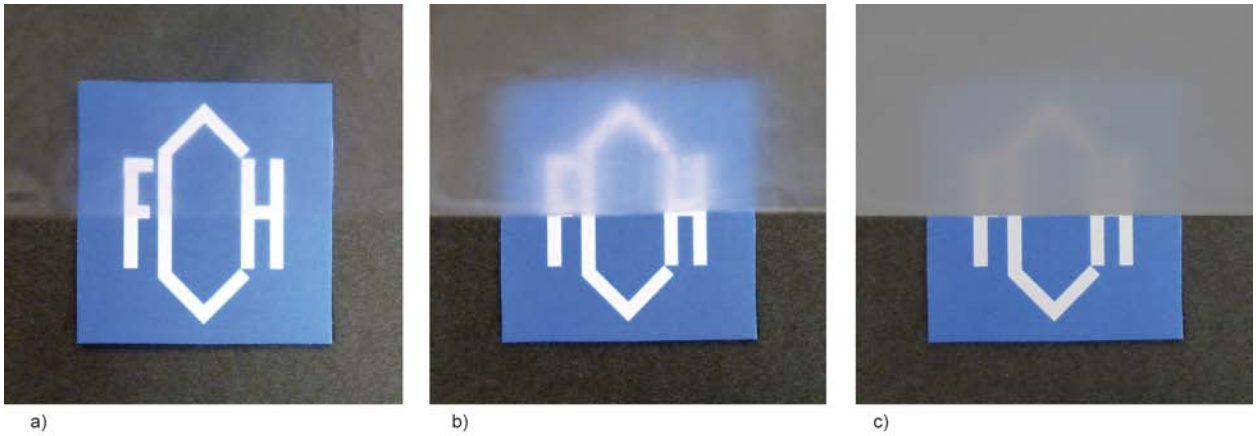

Figure 3. Images of samples differing in opacity: a) transparent PU_{PEG} sample, b) semi-transparent $PU_{3.0}$ and c) opaque PU_{PCL}

PCL was equal to 3 or higher, absorbance increased in the visible spectra range in agreement with semi-transparent appearance of $PU_{3.0}$ sample. The highest absorbance exhibited sample PU_{PCL} with opaque inhomogeneities.

The chemical structure of the synthesized bio-PU samples was qualitatively evaluated using ATR-IR spectroscopy. First, the spectra of PU_{PEG} and PU_{PCL} were compared with spectra of neat PEG, PCL and HDI (Figure 5) confirming the formation of urethane bonds. Their characteristic bands are represented by N–H stretching vibration at 3335 and at 3321 cm^{-1} for PU_{PEG} and PU_{PCL}, respectively. The absorption of amide II (urethane N–H bending and C–N stretching) is located at 1536 cm^{-1}. Strong absorption of C=O band is located at 1714 cm^{-1} and, in the case of PU_{PEG}, it was assigned to hydrogen bonded carbonyl groups in the disordered conformations [22]. In the case of PU_{PCL} the C=O peak split into two peaks, where the first one at 1730 cm^{-1} belongs to non-hydrogen bonded ester carbonyl groups and the second one at 1683 cm^{-1} was ascribed to hydrogen bonded carbonyl in crystalline region [23].

Other peaks presented in the spectra were assigned to asymmetric and symmetric CH_2 stretching located at 2919 and 2866 cm^{-1} for PU_{PEG} and at 2935 and 2858 cm^{-1} for the PU_{PCL}. Other CH_2 vibrations are demonstrated by the bands at 1458 and 1350 cm^{-1} for the PU_{PEG} sample and 1464, 1344 and 1260 cm^{-1} for PU_{PCL} sample. The band at 1100 cm^{-1} in the PU_{PEG} sample was attributed to stretching vibration of ether C–O–C bond in the PEG chain and in the PU_{PCL} sample was assigned to C–O–C ester bond. The strong isocyanate bands at 2360 and 2270 cm^{-1} are absent in both PU_{PEG} and PU_{PCL} spectra indicating complete conversion of the HDI during synthesis.

Interesting differences were observed when comparing free and hydrogen bonded carbonyl groups in all prepared bio-PUs as illustrated in Figure 6. The PU_{PEG} and the bio-PUs with PCL/PEG ratio below 1.8 ($PU_{0.3}$, $PU_{0.8}$ and $PU_{1.8}$) showed carbonyl peak in the region ascribed to hydrogen bonded C=O groups in disordered (amorphous) region [22]. However, the bio-PUs having the PCL/PEG ratio higher than 3 ($PU_{3.0}$, $PU_{6.7}$ and PU_{PCL}) exhibited C=O stretching at 1730 cm^{-1} assigned to non-hydrogen bonded ester carbonyl and also in the region between 1690–1674 cm^{-1} ascribed to hydrogen bonded carbonyl groups in ordered (crystalline) region. The possible functional groups acting as electron donors in the hydrogen bonding with the amide group are the urethane and the ester carbonyl. The higher amount of hydrogen bonded C=O groups in the PCL rich compositions can be explained by the PCL domain crystallinity. The parallel chains orientation in the crystalline regions is assumed to promote the formation of hydrogen bonds.

The glass transition temperature (T_g), melting temperatures (T_m), and crystallinity were determined using DSC traces (Table 2). DSC traces obtained

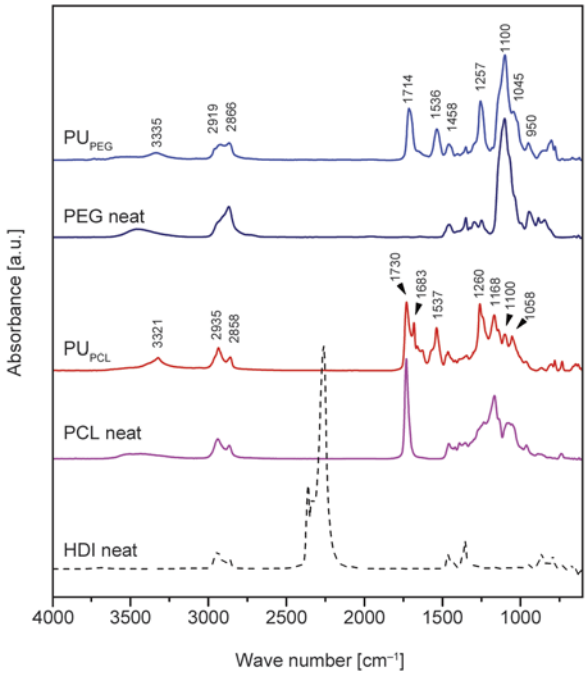

Figure 5. ATR-IR spectra of PU_{PEG} (blue line), PEG neat (dark blue line), PU_{PCL} (red line), PCL neat (violet line) and HDI neat (black dashed line)

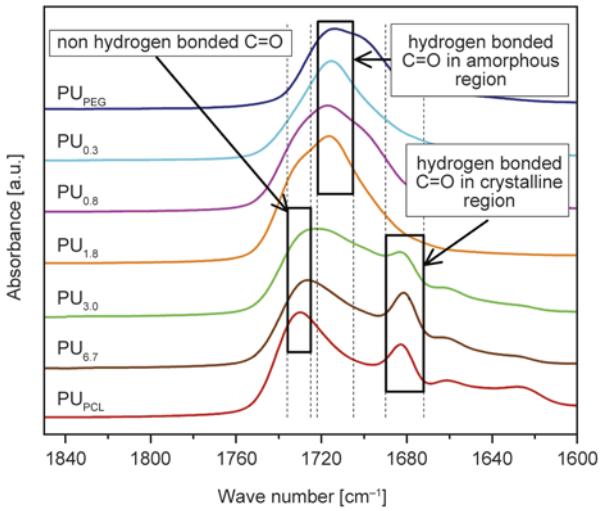

Figure 6. ATR-IR absorption spectra of bio-PU samples showing C=O stretching region

Table 2. T_g, T_m and crystallinity of bio-PU films obtained from DSC thermographs

Sample label	T_g [°C]	T_m [°C]	Crystallinity [%]
PU_{PEG}	–39	–	–
$PU_{0.3}$	–40	–	–
$PU_{0.8}$	–39	–	–
$PU_{1.8}$	–39	–	–
$PU_{3.0}$	–41	52.9	11
$PU_{6.7}$	–41	60.4	19
PU_{PCL}	–41	57.7	25

from the first heating are reported in Figure 7. Composition with a PCL/PEG ratio up to 1.8 showed only single glass transition near –39 °C suggesting amorphous one phase materials. An endothermic melting peak of crystalline PCL domains appeared with higher amounts of PCL. It was found that increasing the amount of PCL increases the bio-PU crystallinity up to 25% in the PU_{PCL}. The thermograph of neat PCL shows quite broad endothermic peak suggesting that PCL cannot crystallize in its neat form due to its low molecular weight.

X-ray diffraction (WAXS) revealed the structure of the crystalline domains in the bio-PUs (Figure 8). Comparing the WAXS spectra of neat PCL polymer (M_n = 80 000 g·mol^{-1}) exhibiting two peaks at 21.4 and 23.8° with the high PCL content bio-PUs, fair agreement with known PCL crystalline diffractions was found [24]. The increased width of the bio-PU X-ray peaks and lower intensity can be ascribed to their less perfectly developed crystalline order. The size of crystallites was ranging between 2–9 nm according to line broadening at half the maximum intensity of diffraction peaks. According to the

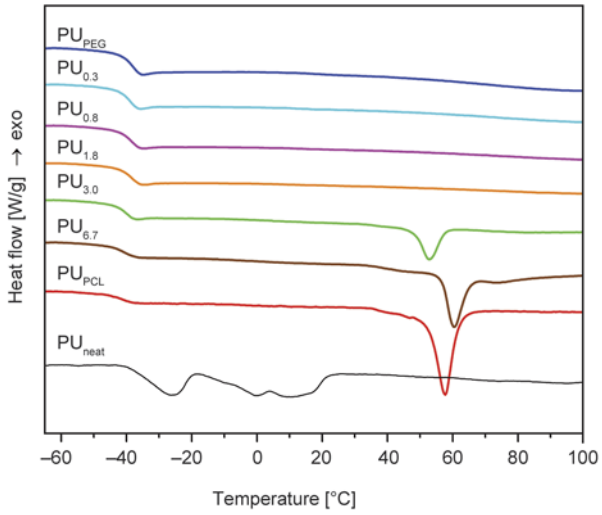

Figure 7. First heating endotherms of the prepared bio-PU samples obtained by DSC analysis

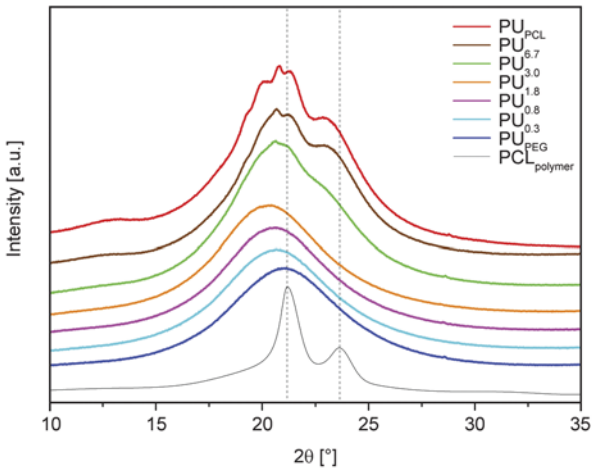

Figure 8. WAXS spectra of the prepared bio-PU specimens confirming crystalline domains of PCL at 20.8 and 22.7° in $PU_{3.0}$, $PU_{6.7}$ and PU_{PCL} samples. Other samples did not show any diffraction peaks.

Bragg's law, the small bands shift between the neat PCL polymer and PU_{PCL} means an increase of interplanar space of PCL crystalline domains formed in bio-PUs. Their structure is influenced by polyurethane network resulting in longer distances between ordered PCL units confirmed by shift of the diffraction peaks to the lower 2θ values. The molecular weight of the used PCL macrodiol was low (M_n = 530 g·mol^{-1}), which accounts for approximately 4 ε-caprolactone monomeric units between the urethane groups. Despite the use of such short PCL chains, crystalline domains in the bio-PU samples were confirmed by both, DSC and WAXS analysis. Bio-PU films made up to molar excess of PCL to PEG equal to 1.8 showed broad amorphous halo without any diffraction peaks indicating no presence of crystalline phase in such films.

Extractions of the prepared bio-PU films were performed using dimethylformamide (DMF) to prove their crosslinked nature and employing acetone to determine the chemical composition of extracted residues (Figure 9). Extraction in DMF has not shown clear composition dependence of the extracted mass. The fact that the prepared bio-PUs did not dissolve in DMF was taken as an indirect evidence of their crosslinked nature influenced by both the excess of isocyanate in the feedstock mixture (NCO/OH = 1.2) and heat post cure. When taking into account possible reactions of isocyanate with other groups forming crosslinks in the system, the only one that can occur in anhydrous conditions is the reaction between isocyanate and urethane group forming allophanate crosslinks. However, allophanates cannot be easily

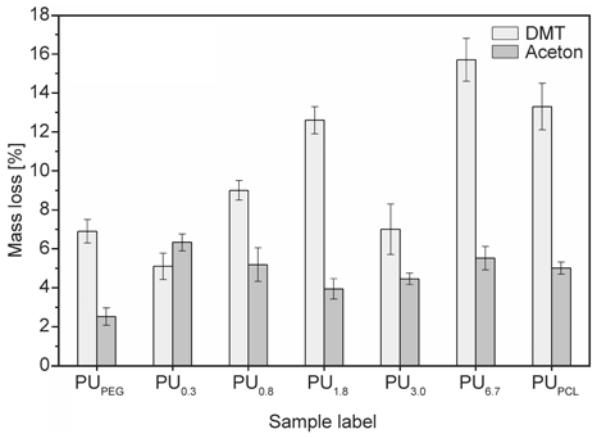

Figure 9. Results of the mass loss after extraction of bio-PU films

distinguished in infrared spectra due to the overlapping of the C=O carbonyl group with the other one from the urethane group.

The comparison between infrared spectra of acetone extracted residues from bio-PU films with those recorded before extraction and with neat PEG and PCL are shown in Figure 10 and 11. All ATR-IR spectra showed that linear, non-crosslinked bio-PUs are presented in extracted residues. Comparison between PUPEG film and its extracted residue showed urethane groups represented by presence of C=O band at around 1715 cm^{-1} and secondary amine band at 1536 cm^{-1} in the extracted residue. Broad –OH peak in the extracted residue suggest possible presence of free PEG diol. Similar results were obtained for the PU_{PCL} when compared with its extracted residue and neat PCL. The presence of the urethane group was also confirmed by second-

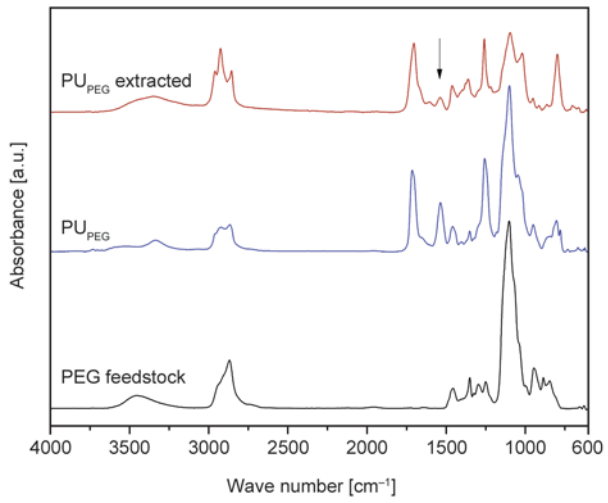

Figure 10. Comparison of PU_{PEG} film ATR-IR spectra with its extracted residue and PEG feedstock. Presence of secondary amine band in extracted residue is emphasized by arrow.

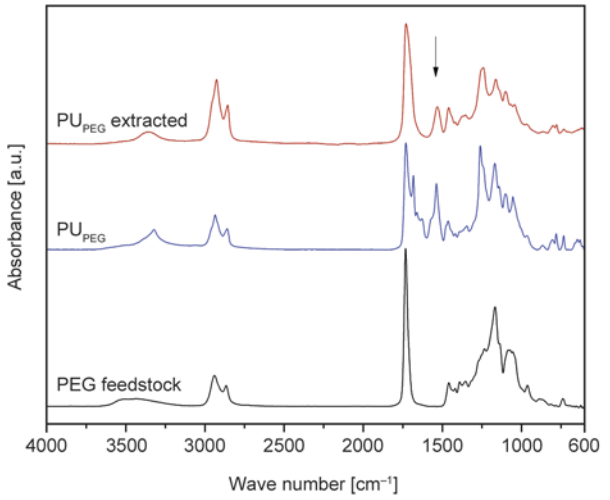

Figure 11. Comparison of PU_{PCL} film ATR-IR spectra with its extracted residue and PCL feedstock. Presence of secondary amine band in extracted residue is emphasized by arrow.

ary amine band at 1536 cm^{-1}. Additionally, the spectrum of extracted residue missed the band between 1690–1674 cm^{-1} attributed to hydrogen bonded carbonyl oxygen visible in PU_{PCL} sample. None of the spectra showed strong isocyanate bands at 2360 and 2270 cm^{-1} confirming that unreacted HDI is not presented in any of the bio-PU materials.

3.2. Swelling and hydrolytic degradation

Results of swelling experiments in terms of the time dependence of the water uptake are shown in Figure 12. The standard deviation varied depending on PCL/PEG ratio in the range from 0.1% for PU_{PCL} up to 6.3% for PU_{PEG}. PCL/PEG ratio strongly influences the ability to absorb water. As expected, hydro-

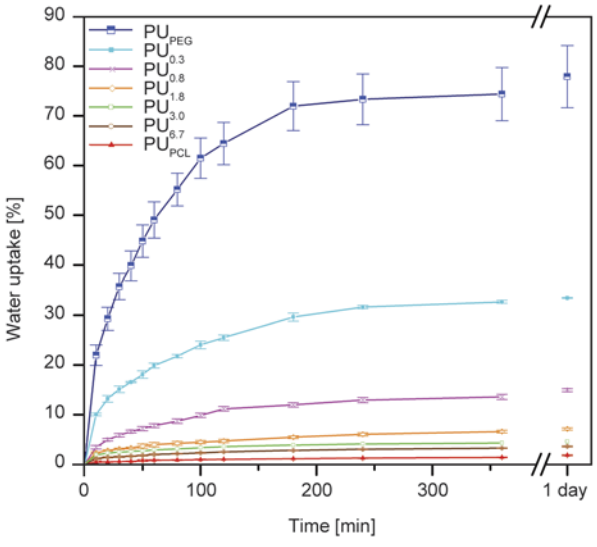

Figure 12. Swelling properties of the synthesized bio-PU films made with different PEG/PCL ratio

philic PU_{PEG} films showed the highest water uptake of 85.2±0.4% after one day of swelling. Water uptake decreased with decreasing amount of PEG diol. The hydrophobic PU_{PCL} film exhibited the lowest water uptake of only 1.8±0.1 % after one day swelling. The hydrophilic behavior of PEG is affected by the ether group repeating every 2 carbons in the macrodiol's chain compared with the hydrophobic PCL where five consecutive $–CH_2–$ groups in the main chain contribute further to PCL hydrophobicity [25]. Moreover, the crystalline domains of PCL exhibit substantially smaller diffusion coefficient, hence, the kinetics of water uptake is massively slowed down.

In vitro hydrolytic degradation tests of the prepared bio-PU films were performed at 37 °C in UPW. The time dependence of the mass loss is presented in Figure 13. The standard deviation increased for all the samples with time of degradation. The values depend on the PCL/PEG ratio ranging for PU_{PEG} sample from 0.36% (beginning) up to 18.2% (sample almost degraded) and for PU_{PCL} from 0.13% (beginning) until 0.32% (end of the observation). The PU_{PEG} film containing only PEG diol exhibited the fastest degradation rate since the sample completely decomposed in 23 weeks. Other compositions containing PCL did not show complete decomposition even over a period of one year. The expected bonds that undergo hydrolysis are ester and urethane ones, where esters are expected to be most unstable [16, 26]. Sample PU_{PEG} contained from the two mentioned only urethane ones and those are expected to be hydrolyzed yielding shorter PU chains. Other reason might be gradual solubilization of PU_{PEG} in water. Therefore, water uptake is an important parameter affecting the hydrolytic stability. Increase of the PEG content in the PU enhanced the rate of the degradation. Hydrophobic nature of samples with higher presence of PCL prevented penetration of water into the material resulted in hydrolytically stable materials over the period of one year.

3.3. Thermal stability

The rate of thermal degradation plotted against temperature is shown in Figure 14. The first weight reduction at approximately 125 °C was caused by removing adsorbed water from the bio-PU surface. The first weight loss was proportional to the amount of PEG in the bio-PU film due to its hydrophilic nature. The thermal degradation subsequently proceeded in two major steps.

More than 80% weight of all the prepared compositions was lost in the temperature interval between 270 and 380 °C. Temperature dependence of the rate of weight loss shows some evidence for presence of several thermal degradation processes. One can assume decomposition of urethane and ester groups with the maximum rate between 310–325 °C and decomposition of ether bonds at higher temperatures with maximum rate between 325–350 °C [27, 28]. The urethane bonds decompose into alcohols and isocyanates, while the decomposition of ester and ether bonds in PCL and PEG, respectively, is assumed through chain scission [29]. The second step occurring between 410–470 °C is assigned to the C–C bond cleavage.

3.4. Mechanical properties analysis

Stress-strain curves of the prepared bio-PU compositions are shown in Figure 15. Samples having the PCL/PEG ratio below 1.8 exhibited brittle deforma-

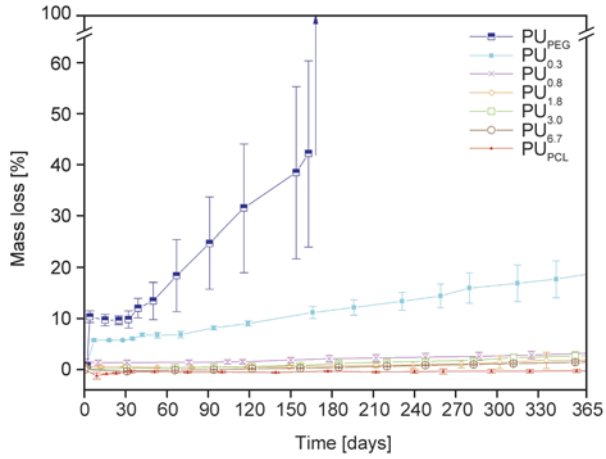

Figure 13. Hydrolytic degradation of the bio-PU films in the period of 1 year

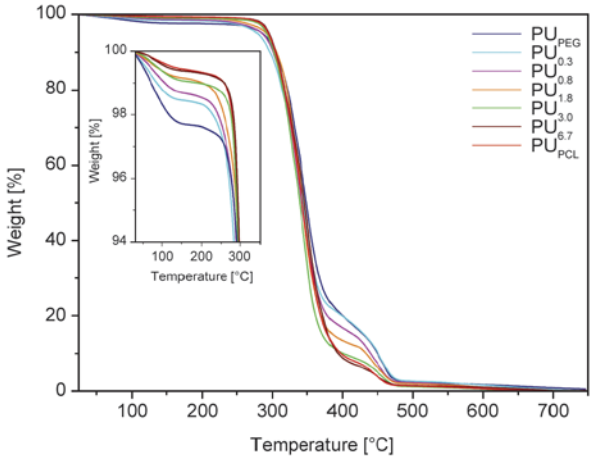

Figure 14. Thermal stability of the bio-PU samples

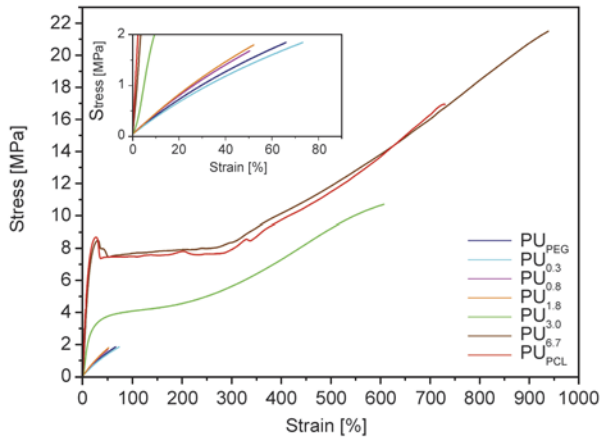

Figure 15. Stress-strain curves of bio-PU films showing rapid change in mechanical properties for PCL/PEG ratio ≥3

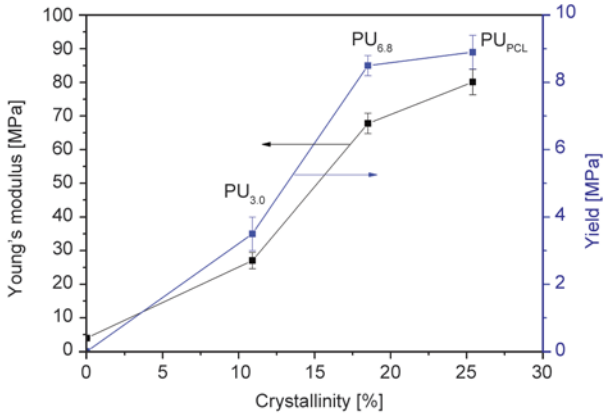

Figure 16. Correlation between mechanical properties (Young's modulus, yield point) plotted against crystallinity

tion behavior (inset in Figure 15). As the PCL/PEG ratio increased above 2, the mechanical response abruptly changed increasing the elastic modulus, stress and deformation at break by order of magnitude while not exhibiting post-yield strain softening. Considerable post-yield strain softening was observed for samples with PCL/PEG ratio above 6 (Figure 15). Young's modulus (E_y), tensile stress at break (σ_B), tensile strain at break (ε_B), and the yield point (σ_y) are listed in Table 3. Mechanical properties are profoundly affected by the increasing amount of PCL in the diol mixture.

Plausible explanation of such mechanical behavior is based on spider dragline model introduced by Termonia [30]. Model ascribes high tensile strength and ductility of spider dragline to the presence of very small crystals (2×6×21 nm) in the rubbery matrix. In agreement with WAXS evidence the bio-PUs with PCL/PEG ≥3 are assumed as a semicrystalline material containing a large number of small crystallites dispersed in amorphous regions made of rubber-like chains. The size of crystallites ranges between 2–9 nm according to line broadening at half the maximum intensity of diffraction peaks. This explanation

Table 3. Mechanical properties of the prepared bio-PU films calculated from stress-strain curves

Label of sample	E_y [MPa]	σ_y [MPa]	σ_B [MPa]	ε_B [%]
PU_{PEG}	3.6±0.2	–	1.9±0.2	70±11
$PU_{0.3}$	3.5±0.3	–	1.7±0.2	64±12
$PU_{0.8}$	4.2±0.1	–	1.7±0.2	50±8
$PU_{1.8}$	4.0±0.1	–	1.7±0.2	50±8
$PU_{3.0}$	27.1±2.4	–	10.7±1.2	600±103
$PU_{6.7}$	67.8±3.0	8.5±0.3	21.5±1.4	947±48
PU_{PCL}	80.1±3.8	8.9±0.5	18.1±1.7	830±100

Table 4. Mechanical properties of some human soft tissues [12]

Tissue	Young's modulus [MPa]	Strain at break [%]
Relaxed smooth muscle	0.006	300
Contracted smooth muscle	0.01	300
Myocardium [31]	0.2–0.5	20 < 90
Cerebral vein	6.85	83
Aortic valve leaflet	15±6	21±12
Pericardium	20.4±1.9	34.9±1.1
$PU_{3.0}$	27.1±2.4	600±103

is supported by correlation between mechanical properties (Young's modulus, yield point) plotted against crystallinity in Figure 16. Thus, the abrupt change of deformation response is explained by the formation of small crystalline domains of PCL.

The amount of PCL feedstock in the material is strongly influencing mechanical properties. This could be further utilized for the preparation of an elastic resorbable material useful in the human body, e.g. as an artificial vascular grafts or as a material against post-surgical adhesions. Short summary of mechanical properties of some human soft tissues is reported in Table 4. Selecting from the prepared bio-PU films the sample labeled as $PU_{3.0}$ did not show sharp yield point determining its very good elastic properties. In addition the sample is quite tough with elongation of about 600% which is favorable for safe manipulation with the material during surgical operation.

3.5. Morphology and surface properties

Bio-PU films morphology was affected by the roughness of the mold, most likely due to processing in bulk. Confocal microscopy images showed similar surface texture of prepared samples and calculated

Table 5. Water contact angles of bio-PU films

Sample label	Contact angle [°]
PU_{PEG}	61.8±3.4
$PU_{0.3}$	72.3±3.7
$PU_{0.8}$	77.1±3.0
$PU_{1.8}$	82.5±2.6
$PU_{3.0}$	84.0±1.3
$PU_{6.7}$	87.8±0.9
PU_{PCL}	88.6±1.1

roughness average (R_a) showed fair agreement between the Teflon® mold (R_a = 0.48±0.12 μm) as well as on the surfaces of PU_{PEG} (R_a = 0,67±0.35 μm) and PU_{PCL} samples (R_a = 0.55±0.28 μm). The roughness of the films can be advantageously tuned by roughness of the mold meeting different medical applications.

Macroscopic measurements of wettability depicted in Table 5 illustrated an increase in contact angle of around 30° from hydrophilic PU_{PEG} to hydrophobic PU_{PCL} sample. The resulting trend corresponds well with the data obtained by swelling where weight ratio between PCL and PEG influences the ability of the material to absorb water.

4. Cell viability evaluation

From all the synthesized samples three of them were chosen for preliminary tests on human mesenchymal stem cells (MSCs) response to the material. Chosen samples were bio-PUs made of only macrodiol (PEG or PCL) and isocyanate (samples PU_{PEG} and PU_{PCL}) and sample $PU_{3.0}$ due to its promising mechanical properties. Analysis of cell viability was performed to determine qualitative changes in cellular growth which involve cell adhesion and proliferation observed by confocal fluorescent microscopy. Cell viability tests were conducted by incubating MSCs on the sample over 24, 72 and 168 hours at 37 °C. Adhered cells were observed only on the samples $PU_{3.0}$ and PU_{PCL} (Figure 17a and 17b, respectively) after 24 hours. No MSCs have been seen on PU_{PEG} sample after 24 hours. This phenomenon is most likely because the PEG based PUs provide a non-adherent environment for MSCs which then undergo apparently no adhesion (PU_{PEG}) or fast detachment ($PU_{3.0}$) from PEGylated surface. By contrast, PU_{PCL} sample provided better substrate for MSCs which supported good adhesion of some MSCs. The cells attached to this bio-PU surface showed flat, well spread morphology over 48 hours (Figure 17c). Only a few surviving cells were observed on PU_{PCL} sample after the period of one week (Figure 17d).

Parameters that can change the biological activity of materials are related to physico-chemical properties of the material surface, such as surface chemistry, wettability, micro-roughness and especially in the case of biodegradable materials their degradation compounds.

Both materials that demonstrated cell adhesion were stable during performed degradation tests in UPW, nevertheless, they might release some uncrosslinked molecules. No cell adhesion on PU_{PEG} and the low adhesion without evident proliferation on $PU_{3.0}$ and PU_{PCL} could be partly attributed to the morphology of polymer surface promoting inhibition of the cell growth. Other reason might be the presence of remaining tin(II) 2-ethylhexanoate catalyst in the material due to the synthesis procedure carried out in bulk. Although the catalyst is FDA approved, this disadvantage has to be overcome by different synthesis procedure of bio-PU, e.g. synthesis at higher temperature without the need of catalyst and still without the need of solvent. Our preliminary results with MSCs did not provide complete information about the cell behavior on selected materials, therefore more *in vitro* analysis of cell viability will be performed as well as various cells must be tested. Observed low MSC's adherence is favorable parameter for the potential use of the material as an artificial vein. However for interaction with a body, further modification of the contact side is desirable by compounds favoring cell adhesion e.g. by RGD proteins.

5. Conclusions

Biodegradable PU films with variable PCL/PEG diol ratio were synthesized without the need of a solvent. The experimental study revealed that addition of PCL strongly affects mechanical properties of bio-PU films, especially for PCL/PEG ratio higher than 1.8. In comparison to PU containing only PEG (PU_{PEG}), the Young's modulus, tensile stress and strain at break increased by 1–2 orders of magnitude. WAXS and DSC measurements revealed formation of crystalline PCL domains at PCL/PEG ratio above 1.8. These domains reinforce the PU network and their small size allows for more uniform distribution of strain resulting in enhanced ductility. The ability to absorb water and the rate of hydrolytic

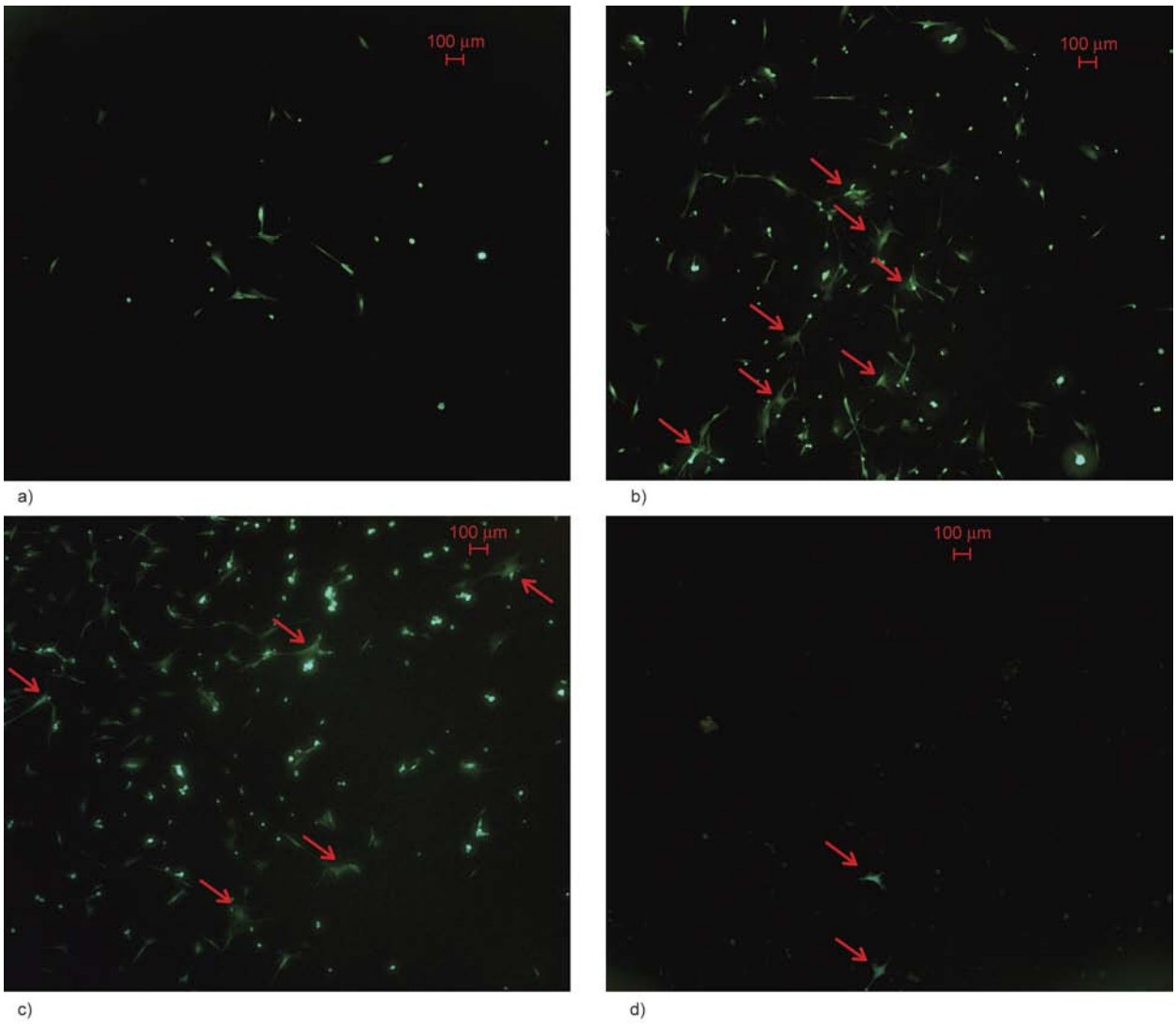

Figure 17. Live/dead assay after seeding with MSCs of sample a) $PU_{3.0}$ after 24 hours, b) PU_{PCL} after 24 hours, c) PU_{PCL} after 72 hours and d) PU_{PCL} after 168 hours. All other images (sample PU_{PEG} after 24, 72 and 168 hours and $PU_{3.0}$ after 72 and 168 hours) were black without any sign of adhered cells on the surface.

degradation both increased with increasing amount of hydrophilic PEG in the compositions. This study demonstrated that by changing the ratio between hydrophilic and hydrophobic macrodiols physico-chemical properties of biodegradable bio-PUs can be tailored. Bio-PU material could be utilized for the preparation of elastic resorbable materials applicable as non-adherent surface against post-surgical adhesions.

Acknowledgements

This research has been financially supported by the Ministry of Education, Youth and Sports of the Czech Republic under the project CEITEC 2020 (LQ1601). The authors are also thankful to Josef Skopalik and Ivan Justan (The International Clinical Research Center of St. Anne's University Hospital in Brno, Czech Republic) for providing MSCs.

References

[1] Howard G. T.: Biodegradation of polyurethane: A review. International Biodeterioration and Biodegradation, **49**, 245–252 (2002).
DOI: 10.1016/S0964-8305(02)00051-3

[2] Santerre J., Woodhouse K. A., Laroche G., Labow R.: Understanding the biodegradation of polyurethanes: From classical implants to tissue engineering materials. Biomaterials, **26**, 7457–7470 (2005).
DOI: 10.1016/j.biomaterials.2005.05.079

[3] Guelcher S. A.: Biodegradable polyurethanes: Synthesis and applications in regenerative medicine. Tissue Engineering Part B: Reviews, **14**, 3–17 (2008).
DOI: 10.1089/teb.2007.0133

[4] Sartori S., Chiono V., Tonda-Turo C., Mattu C., Gianluca C.: Biomimetic polyurethanes in nano and regenerative medicine. Journal of Materials Chemistry B, **2**, 5128–5144 (2014).
DOI: 10.1039/C4TB00525B

[5] Vermette P., Griesse H. J., Laroche G., Guidoin R.: Developments in design and synthesis of biostable polyurethanes. in 'Biomedical applications of polyurethanes' (eds.: Gunatillake P. A., Meijs G. F., McCarthy S. J.) Landes Bioscience, Georgetown, 160–170 (2001).
[6] Ratcliffe A.: Tissue engineering of vascular grafts. Matrix Biology, **19**, 353–357 (2000).
DOI: 10.1016/S0945-053X(00)00080-9
[7] Grad S., Kupcsik L., Gorna K., Gogolewski S., Alini M.: The use of biodegradable polyurethane scaffolds for cartilage tissue engineering: Potential and limitations. Biomaterials, **24**, 5163–5171 (2003).
DOI: 10.1016/S0142-9612(03)00462-9
[8] Gogolewski S., Gorna K.: Biodegradable polyurethane cancellous bone graft substitutes in the treatment of iliac crest defects. Journal of Biomedical Materials Research Part A, **80**, 94–101 (2007).
DOI: 10.1002/jbm.a.30834
[9] Bergmeister H., Seyidova N., Schreiber C., Strobl M., Grasl C., Walter I., Messner B., Baudis S., Fröhlich S., Marchetti-Deschmann M., Griesser M., di Franco M., Krssak M., Liska R., Schima H.: Biodegradable, thermoplastic polyurethane grafts for small diameter vascular replacements. Acta Biomaterialia, **11**, 104–113 (2015).
DOI: 10.1016/j.actbio.2014.09.003
[10] Penco M., Sartore L., Bignotti F., D'Antone S., Di Landro L.: Thermal properties of a new class of block copolymers based on segments of poly(D,L-lactic-glycolic acid) and poly(ε-caprolactone). European Polymer Journal, **36**, 901–908 (2000).
DOI: 10.1016/S0014-3057(99)00155-X
[11] Martin D. J., Meijs G. F., Gunatillake P. A., Yozghatlian S. P., Renwick G. M.: The influence of composition ratio on the morphology of biomedical polyurethanes. Journal of Applied Polymer Science, **71**, 937–952 (1999).
DOI: 10.1002/(SICI)1097-4628(19990207)71:6<937::AID-APP9>3.0.CO;2-0
[12] Chen Q., Liang S., Thouas G. A.: Elastomeric biomaterials for tissue engineering. Progress in Polymer Science, **38**, 584–671 (2013).
DOI: 10.1016/j.progpolymsci.2012.05.003
[13] Kim H-J., Kang M-S., Knowles J-C., Gong M-S.: Synthesis of highly elastic biocompatible polyurethanes based on bio-based isosorbide and poly(tetramethylene glycol) and their properties. Journal of Biomaterials Applications, **29**, 454–464 (2014).
DOI: 10.1177/0885328214533737
[14] Hassan M., Mauritz K., Storey R., Wiggins J.: Biodegradable aliphatic thermoplastic polyurethane based on poly(ε-caprolactone) and L-lysine diisocyanate. Journal of Polymer Science Part A: Polymer Chemistry, **44**, 2990–3000 (2006).
DOI: 10.1002/pola.21373
[15] Cometa S., Bartolozzi I., Corti A., Chiellini F., De Giglio E., Chiellini E.: Hydrolytic and microbial degradation of multi-block polyurethanes based on poly(ε-caprolactone)/poly(ethylene glycol) segments. Polymer Degradation and Stability, **95**, 2013–2021 (2010).
DOI: 10.1016/j.polymdegradstab.2010.07.007
[16] Mondal S., Martin D.: Hydrolytic degradation of segmented polyurethane copolymers for biomedical applications. Polymer Degradation and Stability, **97**, 1553–1561 (2012).
DOI: 10.1016/j.polymdegradstab.2012.04.008
[17] Sartori S., Boffito M., Serafini P., Caporale A., Silvestri A., Bernardi E., Sassi M. P., Boccafoschi F., Ciardelli G.: Synthesis and structure–property relationship of polyester-urethanes and their evaluation for the regeneration of contractile tissues. Reactive and Functional Polymers, **73**, 1366–1376 (2013).
DOI: 10.1016/j.reactfunctpolym.2013.01.006
[18] Chan-Chan L., Solis-Correa R., Vargas-Coronado R., Cervantes-Uc J., Cauich-Rodríguez J., Quintana P., Bartolo-Pérez P.: Degradation studies on segmented polyurethanes prepared with HMDI, PCL and different chain extenders. Acta Biomaterialia, **6**, 2035–2044 (2010).
DOI: 10.1016/j.actbio.2009.12.010
[19] Li G., Li D., Niu Y., He T., Chen K. C., Xu K.: Alternating block polyurethanes based on PCL and PEG as potential nerve regeneration materials. Journal of Biomedical Materials Research Part A, **102**, 685–697 (2014).
DOI: 10.1002/jbm.a.34732
[20] Silvestri A., Sartori S., Boffito M., Mattu C., di Rienzo A. M., Boccafoschi F., Ciardelli G.: Biomimetic myocardial patches fabricated with poly(ε-caprolactone) and polyethylene glycol-based polyurethanes. Journal of Biomedical Materials Research Part B: Applied Biomaterials, **102**, 1002–1013 (2014).
DOI: 10.1002/jbm.b.33081
[21] Kweon H. Y., Yoo M. K., Park I. K., Kim T. H., Lee H. C., Lee H-S., Oh J-S., Akaike T., Cho C-S.: A novel degradable polycaprolactone networks for tissue engineering. Biomaterials, **24**, 801–808 (2003).
DOI: 10.1016/S0142-9612(02)00370-8
[22] Rueda-Larraz L., d'Arlas B., Tercjak A., Ribes A., Mondragon I., Eceiza A.: Synthesis and microstructure–mechanical property relationships of segmented polyurethanes based on a PCL–PTHF–PCL block copolymer as soft segment. European Polymer Journal, **45**, 2096–2109 (2009).
DOI: 10.1016/j.eurpolymj.2009.03.013
[23] Pretsch T., Jakob I., Müller W.: Hydrolytic degradation and functional stability of a segmented shape memory poly(ester urethane). Polymer Degradation and Stability, **94**, 61–73 (2009).
DOI: 10.1016/j.polymdegradstab.2008.10.012

[24] Correlo V. M., Boesel L. F., Bhattacharya M., Mano J. F., Neves N. M., Reis R. L.: Properties of melt processed chitosan and aliphatic polyester blends. Materials Science and Engineering: A, **403**, 57–68 (2005). DOI: 10.1016/j.msea.2005.04.055

[25] Woodruff M. A., Hutmacher D. W.: The return of a forgotten polymer – Polycaprolactone in the 21st century. Progress in Polymer Science, **35**, 1217–1256 (2010). DOI: 10.1016/j.progpolymsci.2010.04.002

[26] Schollenberger C. S., Stewart F. D.: Thermoplastic polyurethane hydrolysis stability. Journal of Elastomers and Plastics, **3**, 28–56 (1971). DOI: 10.1177/009524437100300103

[27] Chattopadhyay D., Webster D.: Thermal stability and flame retardancy of polyurethanes. Progress in Polymer Science, **34**, 1068–1133 (2009). DOI: 10.1016/j.progpolymsci.2009.06.002

[28] Król P.: Linear polyurethanes: Synthesis methods, chemical structures, properties and applications. VSP, Boston (2008).

[29] Kong X., Liu G., Curtis J.: Novel polyurethane produced from canola oil based poly(ether ester) polyols: Synthesis, characterization and properties. European Polymer Journal, **48**, 2097–2106 (2012). DOI: 10.1016/j.eurpolymj.2012.08.012

[30] Termonia Y.: Molecular modeling of spider silk elasticity. Macromolecules, **27**, 7378–7381 (1994). DOI: 10.1021/ma00103a018

[31] Boffito M., Sartori S., Ciardelli G.: Polymeric scaffolds for cardiac tissue engineering: Requirements and fabrication technologies. Polymer International, **63**, 2–11 (2014). DOI: 10.1002/pi.4608

eXPRESS Polymer Letters Vol.10, No.6 (2016) 493–505
Available online at www.expresspolymlett.com
DOI: 10.3144/expresspolymlett.2016.47

A Voronoi-diagram analysis of the microstructures in bulk-molding compounds and its correlation with the mechanical properties

B. Bertoncelj[1,2], K. Vojisavljević[3], J. Rihtaršič[1], G. Trefalt[4], M. Huskić[5], E. Žagar[5], B. Malič[3]*

[1]Domel, d.o.o., Otoki 21, 4227 Železniki, Slovenia
[2]Jožef Stefan International Postgraduate School, Jamova cesta 39, 1000 Ljubljana, Slovenia
[3]Jožef Stefan Institute, Jamova 39, 1000 Ljubljana, Slovenia
[4]University of Geneva, Sciences II,Quai Ernest-Ansermet 30, 1205 Geneva, Switzerland
[5]National Institute of Chemistry Slovenia, Hajdrihova 19, 1001 Ljubljana, Slovenia

Received 27 October 2015; accepted in revised form 8 January 2016

Abstract. Voronoi analysis is implemented to assess the influence of fiber content on the microstructure and mechanical properties of bulk-molding compounds containing different weight fractions of E-glass fibers (EGF) (5–20 wt%). The fiber distribution in the polymer matrix is analyzed by scanning electron microscopy followed by the Voronoi tessellations, radial distribution function and statistical calculations. The experimental results are compared to modelled microstructures. The derived microstructural descriptors allow us to correlate the fiber weight content and the degree of fiber distribution homogeneity with the mechanical properties of EGF-reinforced composites. The distribution of fibers in composites with 10 and 15 wt% of fibers could be considered as the most homogeneous. This is in a good agreement with the results of the flexural strength and dynamic mechanical analyses, which confirmed that the latter samples exhibit the highest level of reinforcement.

Keywords: *polymer composites, microstructures, mechanical properties*

1. Introduction

Bulk-molding compounds are multiphase composite materials, most commonly consisting of a polymer resin as the matrix, discontinuous glass fibers as the secondary phase and mineral filler. BMCs are widely employed in transportation, in the electrical and the electronic industries, especially for the mass production of small, complex-shaped components, since they offer ease of manufacturing, have low costs, and exhibit good mechanical properties [1]. Common processing methods for the production of such parts are injection and compression molding [2].

The mechanical properties of composite components are strongly influenced by the morphology and weight percentage of the glass fibers. Evidently, an inhomogeneous microstructure can result in local variations of the stress concentration, which can affect the mechanical performance of the composite material [3, 4].

In recent years, in order to characterize the microstructures of fiber-reinforced composites, different image-analysis techniques have been applied using optical microscopy or scanning electron microscopy (SEM) [5–7]. One of the methods used to quantitatively describe the microstructure is a Voronoi diagram, commonly known as the Dirichlet tessellation [8, 9]. This approach is often used for describing non-crystalline structures for example amorphous solids, liquids, and dense gases [10, 11]. This is a method of dividing a plane into areas known as Voronoi poly-

*Corresponding author, e-mail: barbara.bertoncelj@domel.com

gons. Every polygon is assigned to a given point in a plane and occupies a region around that point, allowing that all neighboring points are closer to the tracked point than to any other point in the set. In fact, a set of convex polygons could be formed by introducing planar cell walls that are perpendicular to the lines connecting neighboring points. Voronoi analysis can be extended also in three dimensions. In this case, the Voronoi cells are defined as 3D polyhedrons [10, 12]. In material science the Voronoi diagram was used to quantify the distribution of the zirconia phase in alumina-matrix composites [13]. This study pointed out that the wear resistance is related to the microstructural homogeneity of the composite. Trefalt *et al*. [14] studied the distribution of tetragonal zirconia particles in $Pb(Zr,Ti)O_3$ ceramic composites using a Voronoi-diagram analysis. Summerscales *et al*. [15] used the Voronoi method to investigate the relationship between the processing, properties and structure in fiber-reinforced polymer-matrix composites. A characterization of sisal-reinforced composite microstructures was carried out by Sun *et al*. [16]. They characterized the porous structure of the sisal fibers and studied the effect of a maleated polypropylene compatibilizer on the polypropylene matrix's crystallization using Voronoi diagrams. They also used the Voronoi method to perform a quantitative analysis of the fiber distribution within the polymer matrix in order to relate it to the tensile modulus of differently treated composites. Ghosh *et al.* [17] applied a Voronoi diagram to characterize computer-simulated multiphase microstructures. The same authors also used the radial distribution functions (RDFs) to analyze the patterns in their composites. These RDFs give information about the distribution of particles around a central particle and can therefore be used to detect clustering in the system [17]. Another study of simulated microstructures was made by Pyrz and Bochenek, who investigated the topological disorder of inclusions in composites [18].

On the other hand, microstructural parameters, such as the length, loading, orientation and distribution of the reinforcing fibers, were identified as the most significant factors affecting the mechanical properties of composites. A dynamic mechanical analysis (DMA), where the storage modulus (E'), loss modulus (E'') and damping loss factor ($\tan\delta$) are measured as a function of temperature and frequency, was found to be useful in correlating the mechanical properties with the microstructure of the material [19–22]. Recently, studies were made of the influence of various glass/natural-fiber volume fractions, such as ramie and curaua fibers, on the dynamic mechanical properties [23, 24].

The aim of this study was to correlate the microstructural features, i.e. inhomogeneous fiber distribution and fiber clustering, with mechanical properties of BMC samples. Such approach could then be applied to obtain insight about mechanical response of critical parts of products manufactured from BMCs, especially those of complex geometry through microstructural analysis.

The Voronoi-diagram method and a RDF analysis were used to quantitatively characterize the microstructures of BMC composites fabricated with different weight fractions of glass fibers in order to evaluate the homogeneity of the fiber distribution in a polymer matrix (PM). The relationship between the homogeneity of the fiber distribution in cross-section, i.e. perpendicular to the compound filling flow direction upon compression molding, and the mechanical properties of the composites was investigated. Therefore, the effect of the glass fiber's weight fraction on the static and dynamic mechanical properties of the composites, such as the flexural strength, storage modulus, loss modulus and damping behavior, is related to the level of the microstructural homogeneity evaluated with the Voronoi analysis and the clustering described by the RDF.

2. Experimental

2.1. Materials

Four formulations of BMC (Tetradur Gmbh., Hamburg, Germany) were commercially prepared by varying the glass-fiber and mineral-filler weight fractions. As a reference, a composite of polymer matrix (subsequently denoted as PM) and mineral filler was also prepared. The E-glass fibers, denoted as EGF, were 4.5 mm long, with a diameter of approximately 11 μm, while the mineral filler was $CaCO_3$ with a particle size range from a few microns up to a few tens of microns as determined by SEM. Furthermore, the PM was based on thermosetting unsaturated polyester, styrene and additives, comprising 21 wt% of the overall composite material. The compositions of the samples are collected in Table 1.

Table 1. Compositions of the BMC composite materials

No.	PM [wt%]	EGF [wt%]	$CaCO_3$ [wt%]
0	21	0	79
1	21	5	74
2	21	10	69
3	21	15	64
4	21	20	59

The test specimens were fabricated by compression molding, in accordance with the standard ISO 3167 [25]. About 42 g of the compound was placed into a mold cavity that was heated to around 165 °C and pressed at a molding pressure of 20 MPa on a hydraulic compression press (HPK 100/6, Bussmann, Munchen, Germany) with a cure cycle of 2 minutes. After molding, the test specimens were cooled down to room temperature. The scheme in Figure 1 indicates the dimensions of the samples and the filling direction of the material during the compression-molding process. The test specimens were then cut perpendicular to the filling-flow direction, as represented in Figure 1, to yield a cross-sectional area with dimensions of 10 mm×4 mm.

2.2. Microstructural characterization

The cross-section microstructures of the composites were investigated using a field-emission scanning electron microscope FE-SEM (JSM-7600F JEOL Ltd., Tokyo, Japan). Prior to the investigation, special attention was paid to the standard metallographic technique normally used for the preparation of flat surfaces for the SEM investigation in order to establish the best conditions for the grinding and polishing of the samples' cross-sections. The polished

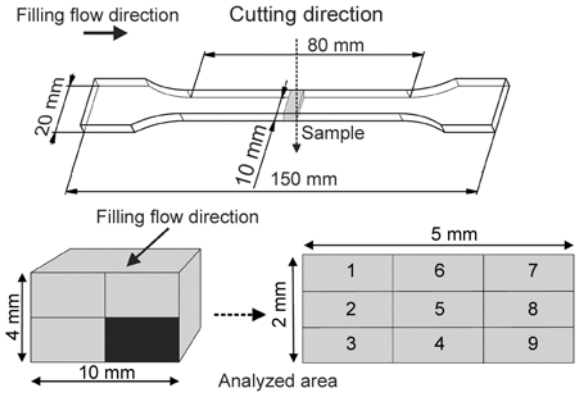

Figure 1. Schematic representation of the test specimen's dimensions, the cutting position and the sample dimensions, with the sampling scheme of the cross-sectional area for the morphological characterization

cross-section surfaces were sputter-coated with a thin carbon layer and micrographs were taken in backscattered-electron mode (composition contrast mode – COMPO) at an accelerating voltage of 15 kV.

For each sample, the cross-sectional area was divided into quarters, as shown in Figure 1. The sampling included capturing 9 images from 9 segments in one quarter. Each image size was 481 μm×361 μm. The overall investigated area for each sample was 1.6 mm^2.

2.3. Voronoi diagrams

The Voronoi diagrams were generated from the SEM micrographs. The process included analyzing 9 SEM micrographs taken from 9 different segments of an individual sample, as shown in Figure 1, and proceeded as follows (see Figure 2). First, the center of each glass fiber on the SEM micrograph (a) was marked with a black point using Corel Paint Shop Pro X7 software. The oval-shaped and elongated fibers were treated in the same way, meaning that the point mark was put at the center of the intersection area of each fiber. The point-pattern images (b) were then saved as binary images and subsequently employed to construct the Voronoi polygons (c) using ImageJ software. The area of each Voronoi polygon was measured using Image Tool software. As a reference, for each composition of the composite material, a pattern of randomly distributed disks (d) and a corresponding Voronoi diagram were generated (e). For the randomly generated pattern a constraint of 'no overlapping disk' was used. The randomness of the produced structures was ensured by the use of uniformly distributed random numbers in the [0,1] interval, which were used to generate random positions within the sample. Check of randomness was done by analyzing such point distributions which yielded RDF functions whose value was 1 in the whole interval. This ensures that the points are distributed perfectly random. Furthermore, the area distributions of our randomly generated Voronoi tessellations are in agreement with literature [26]. A sample area and a disk size of 481 μm×361 μm and 11 μm were chosen; these values correspond to the experimental values.

The tessellation of a microstructure into Voronoi polygons is a critical step in generating the geometrical descriptors necessary to quantify the fibers' distribution in a given microstructure of the com-

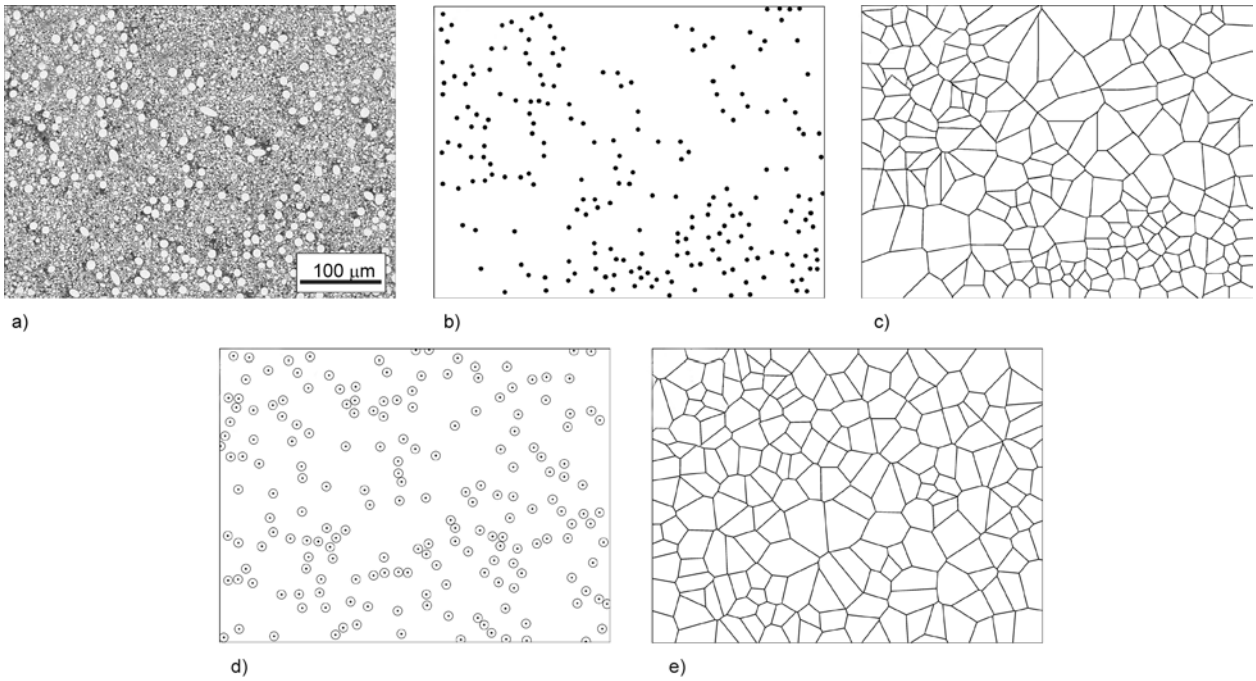

Figure 2. Representation of the sequence of steps involved in generating the Voronoi diagrams from the SEM micrograph (top) and from the randomly distributed disks (bottom): a) SEM micrograph, b) binary point-pattern image obtained from the SEM micrograph by point marking of each fiber, c) the Voronoi diagram generated from the point-pattern image, d) modelled microstructure of random distribution of fibers and e) the Voronoi diagram generated from the modelled microstructure. Note that the minimum interpoint distance in d) was set to be equal to the fibers' diameter, which ensures that there is no overlap of the fibers

posite material. In this way, the analyzed areas 1–9 (see Figure 1) could be easily identified and quantified using statistical parameters like the mean area size of the polygons, the standard deviation and the relative polygon areas. The number of polygons included in the calculations was 468, 998, 1370 and 1979 for the composites with fractions of EGF from 5 to 20 wt%, respectively. Between 250 and 1000 realizations were used in the case of the randomly generated samples to ensure good statistics. The areas of the Voronoi polygons were calculated for each sample. The absolute areas were then normalized to relative polygon areas, which enables an easier comparison of the samples with different fractions of fibers. The relative polygon areas, A_r were calculated according to Equation (1):

$$A_r = \frac{A_p N}{A_{total}} \tag{1}$$

where A_p is the absolute polygon area, N is the number of polygons in the sample, A_{total} is the area of the sample. Such a normalization defines the mean area of the polygons as being equal to 1, regardless of the fiber fraction. Histograms of the relative polygon areas were generated for each sample.

In addition, the shape of the fibers was obtained from binary (black fiber on a white background) images of the microstructures in which the individual fibers were outlined in black. A stereological analysis was performed using the Image Tool program. The elongation shape factor was determined as the ratio of the longest to the shortest axis of the fiber cross-section.

2.4. Radial distribution function analysis

The fiber-reinforced composite microstructures and the randomly created disk patterns were quantitatively described by the RDF, which is related to the probability of finding a particle j at a distance r from the center of a particle i, and is defined as Equation (2):

$$g_{ij}(r) = \frac{1}{\rho_j N_i} \sum_i \sum_{j \neq i} \left\langle \delta(r - r_{ij}) \right\rangle \tag{2}$$

where ρ_j is the density of the particles j, N_i is the number of particles i, r is the distance from the center of the particle i, r_{ij} is the distance between the i and j particles, and $\langle \delta(r - r_{ij}) \rangle$ is the averaged delta function [27]. In fact, the RDF measures the density of the particles j at a distance r from the center of

the particle *i*, normalized by the average density of the particles *j* (Equation (3)):

$$g_{ij}(r) = \frac{\rho_{ij}(r)}{\rho_j} \tag{3}$$

where ρ_{ij} is the local concentration of particles *j* at a distance *r* from a particle *i*. For the calculation of the RDFs, periodic boundary conditions with a minimum image convention were used [27, 28].

2.5. Flexural properties

The flexural strength of the test specimens was obtained using the three-point bending method with a 64 mm span and a crosshead speed of 2.0 mm/min (Alpha 50-5, Messphysik Materials Testing Gmbh., Fürstenfeld, Austria), in accordance with the standard ISO 178:2003 [29]. The test was carried out under ambient conditions using 15 specimens for each set. The flexural strength was calculated using Equation (4):

$$\sigma_f = \frac{3Pl}{2bh^2} \tag{4}$$

where σ is the flexural strength, *P* is the maximum fracture load, *l* is the span between the supports, *b* is the width of the sample and *h* is the thickness of the sample.

2.6. Dynamic mechanical analysis (DMA)

Dynamic mechanical analyses were performed on a TA Q800 thermal analyzer (Q800 DMA, TA Instruments, New Castle, Delaware, United States) in order to evaluate the dynamic moduli (E' and E'') and the damping behavior ($\tan\delta$) of the BMC composites. The $\tan\delta$ is the ratio between loss (E'') and storage modulus (E') (Equation (5)):

$$\tan\delta = \frac{E''}{E'} \tag{5}$$

For the measurement the test specimens were cut with a diamond blade saw to the length of 60 mm and thinned to 3.5 mm by grinding (the width remained the same, i.e. 10 mm). The test was carried out at a frequency of 1 Hz and at strain amplitude of 10 μm using a three-point bending mode. The properties were measured in the temperature range 20–200 °C at a heating rate of 2 °C/min.

3. Results and discussion

3.1. Microstructure, RDF analysis and Voronoi diagrams

3.1.1. Microstructure and Voronoi analysis of a selected cross-sectional segment

The segment 4 of the overall analyzed positions at the sample's cross-sectional area (see Figure 1) was chosen to represent the microstructure of the composites and the distribution of the EGF in the PM. The microstructures of the polished cross-sections of all the BMC composites with the corresponding Voronoi diagrams, and Voronoi diagrams from randomly generated microstructures are collected in Figure 3. The SEM micrographs show the distributed glass fibers, which are surrounded by irregularly shaped particles of $CaCO_3$ mineral filler and the PM (dark regions). Because the orientation of the glass fibers in the material is random, the intersections of the glass fibers that are perpendicular to the cutting position are circular and others, which are cut at an angle, are oval-shaped.

In order to distinguish between the microstructures with possible fiber clustering and a more even and regular fiber distribution in the composites with different EGF contents, the Voronoi diagrams from our experiment were compared with the diagrams from randomly generated microstructures (see Figure 3, central and right columns). It is clear that at lower weight fractions of the EGF, i.e., at 5 wt%, the Voronoi polygons are quite large. However, by increasing the weight fraction of the EGF the spatial distances between the fibers become smaller, and that is reflected in the smaller polygon areas. In particular, marked differences in the size of the polygons are observed in the Voronoi diagrams of the composites with 15 and 20 wt% of EGF (Figure 3 c, 3d). In experimental diagrams the relatively small polygon areas indicate EGF clustering within the PM, which arises from the insufficient space for the fibers to orient and regularly distribute at higher weight fractions. In contrast, homogeneous fiber distributions, which are reflected in equally sized polygons across the whole pattern, can be seen in the Voronoi diagrams obtained from the computer-generated random distribution of fibers.

3.1.2. Voronoi and RDF analyses of the cross-sectional area

The quantitative description of the fiber distribution in the host PM within the cross-sectional area, as

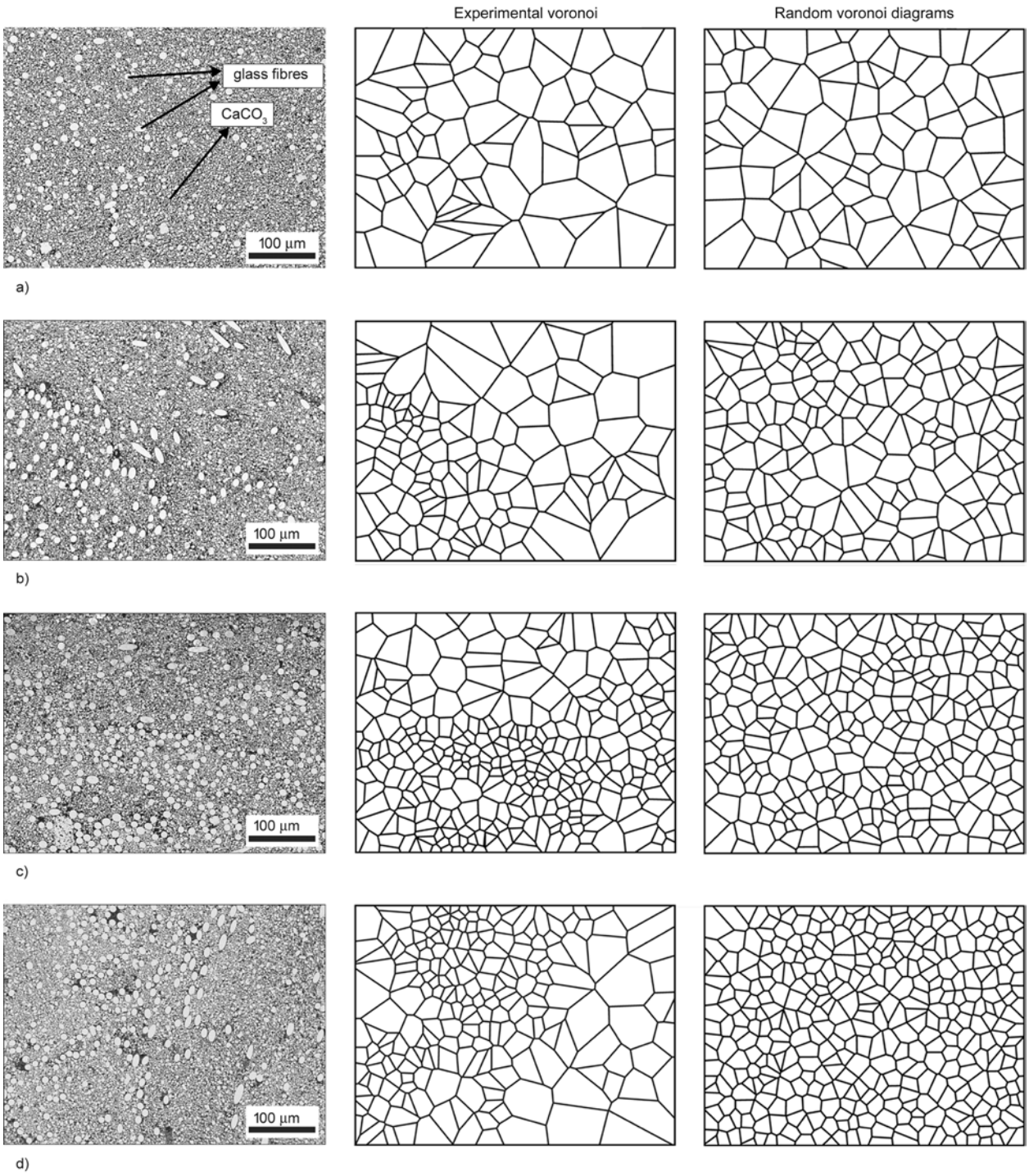

Figure 3. SEM micrographs of polished cross-sections of the BMC composites and the corresponding Voronoi diagrams from the experimental and randomly generated fiber distribution (from area 4): 5 wt% (a), 10 wt% (b), 15 wt% (c), and 20 wt% (d) of the EGF

shown in Figure 1, was carried out by RDF analysis. This method was already found to be useful in describing the fiber distribution in fiber-reinforced composites [17, 30]. In fact, the RDF gives information about the areal density of the fibers at a certain distance and can subsequently indicate the degree of fiber clustering in the microstructure. The results are shown in Figure 4 and include all 9 analyzed segments for all composites. The general shape of the experimental and modeled RDFs is similar. At distances below the fiber diameter the RDFs are equal to 0, since the fibers cannot interpenetrate each other. After the distance of closest approach of about 10 µm, the $g(r)$ increases rapidly above 1 and later

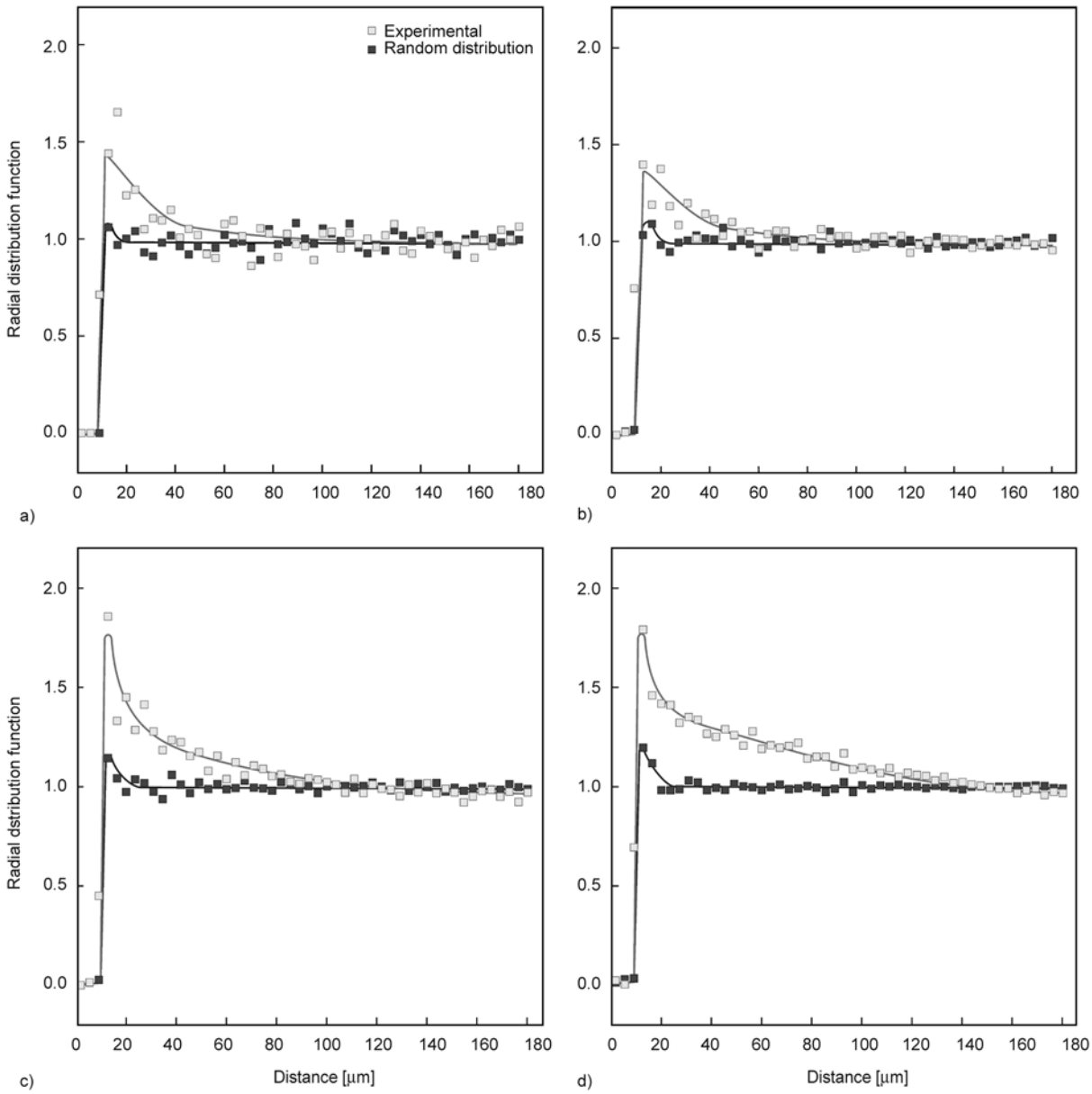

Figure 4. The RDFs of the experimental and randomly generated fiber patterns for all the BMC composites: a) 5 wt%, b) 10 wt%, c) 15 wt% and d) 20 wt% of EGF

decays to a value of 1 at large distances. The peak at the distance of closest approach shows that the density of the fibers at this distance is higher than the average density and can be connected to the clustering of the fibers.

Obviously, the experimental RDF values are higher than in the modeled RDFs in all the composites, especially at distances below 40 μm. The difference is even more noticeable at higher weight fractions of the EGF (15 and 20 wt% of EGF), indicating additional clustering of the fibers, which can be assigned to their increased number. As an example of such fiber-clustering, the cross-section microstructure of the segment 5 of the composite with 15 wt% of EGF is shown in Figure 5.

Hence, the values of the experimental fiber distribution are approaching the values of the ideal distribution with increasing distances, and they are reached sooner at a lower EGF weight content, i.e., at 5 and 10 wt% of EGF. Based on these results, it can be concluded that the distribution of fibers in the composites with 5 and 10 wt% of EGF most closely approximates to the values extracted from the random distributions.

The relative frequencies of the Voronoi-polygon areas from the experimental and simulated microstruc-

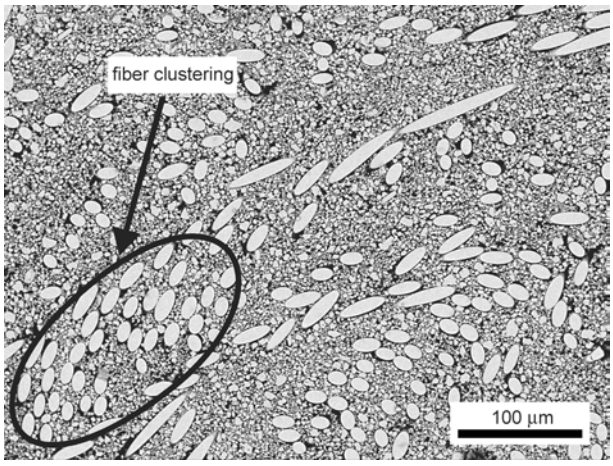

Figure 5. Cross section microstructure of the segment 5 of the composite with 15 wt% of EGF where fiber clustering is observed

tures are shown in Figure 6. In the case of the composite with 5 wt% of EGF the distribution is quite broad due to the larger number of smaller and larger polygons. This is a consequence of local areas with only resin and mineral filler that occur in the composite microstructure at lower weight fractions of EGF. Therefore, the spatial distances between the fibers are quite large in some areas, resulting in larger areas for the Voronoi polygons. Here, the experimental and modeled distributions of EGF are very close. However, the coincidence of the experimental and random distribution plots does not imply that such a composition is the best from the viewpoint of mechanical performance, since the mechanical properties depend on both the content

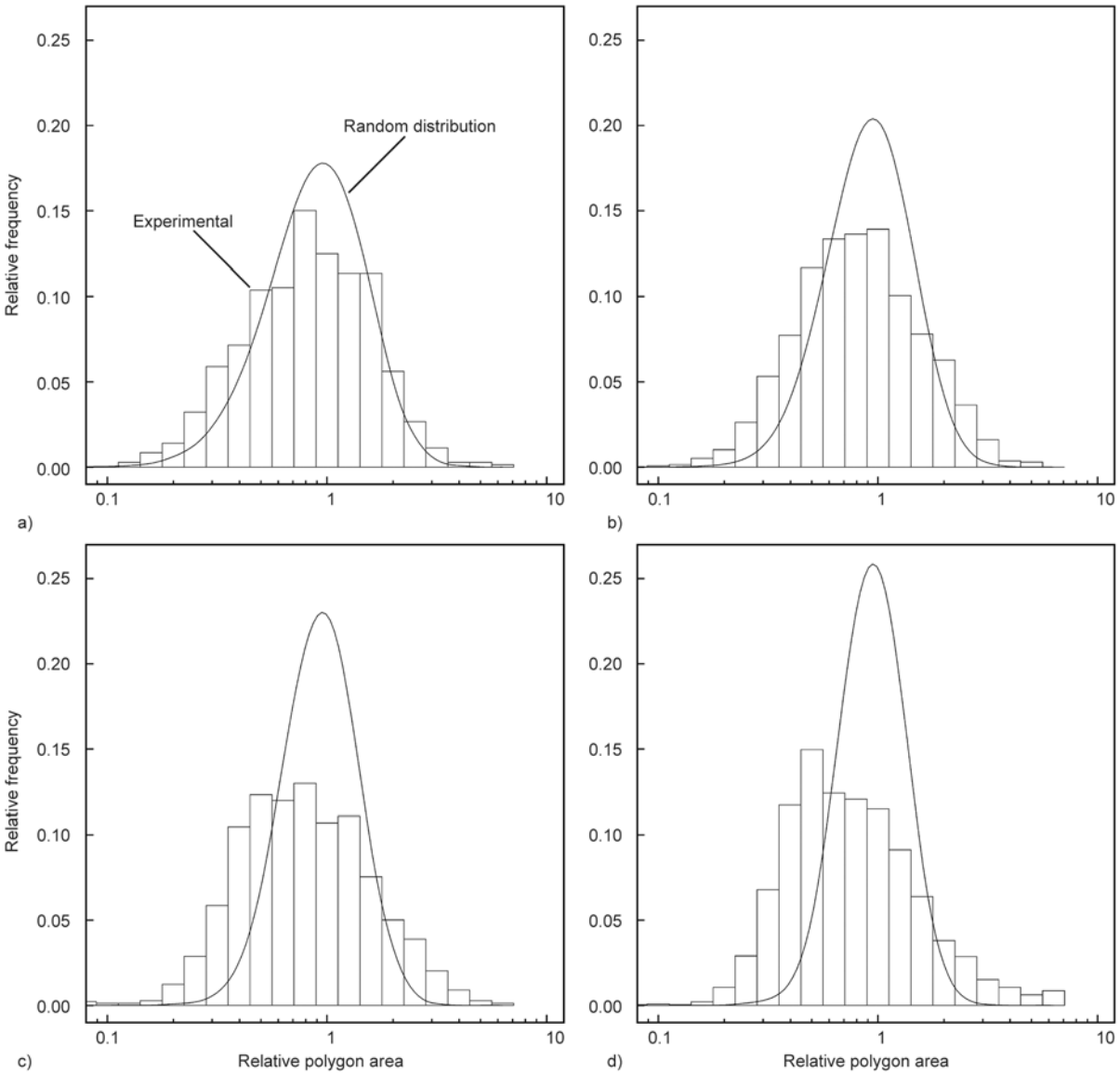

Figure 6. Histograms of the relative polygon areas of all the BMC composites extracted from the Voronoi diagrams of the experimental and randomly generated fiber-distribution pattern: a) 5 wt%, b) 10 wt%, c) 15 wt% and d) 20 wt% of EGF

of fibers and their distribution, as discussed below (see section 3.2.).

The histogram of the composite with 10 wt% of EGF indicates a somewhat narrower distribution of polygons. Such an improved distribution can be mainly related to the increased number of fibers in the PM, i.e., to the decreased number of the local areas filled with resin and mineral filler. Also, the histogram of the ideal random distribution becomes narrower, with the peak shifting to slightly higher values. The divergence of the experimental distribution from the ideal one is even more apparent at higher EGF contents, i.e., at 15 and 20 wt%, which could be primarily the result of clustering in the microstructures, where the distance between the fibers is short and equidistant only locally, rather than across the whole pattern. Due to the closer packing of the fibers at higher weight fractions of the EGF the area sizes of the Voronoi polygons become smaller. This is especially pronounced in the case of the composite with 20 wt% of EGF, where the peak maximum in the experimental distribution shifts toward a smaller relative polygon area, indicating fiber clustering. In general, one can observe that the histograms of randomly generated distributions are narrower and their peak is higher when the fiber content is increased. This observation suggests more even distributions at higher fractions of fibers, which is the consequence of a smaller available space for each fiber. On the other hand, the experimental histograms have a similar width and a shift to smaller polygon areas at higher fiber contents. This behavior shows that in the experimental samples, the clustering, which counteracts the evenness, is increasingly pronounced with increasing fiber content. This observation is very much in line with the results from the RDF analysis.

This was also confirmed with a stereological analysis. The elongation parameter, expressed as the ratio of the longest and shortest axis of the fiber cross-section, and is equal to 1 for a perfect circle, is shown in Figure 7. The results are presented for all 9 segments of an individual composite. The higher the weight percent of EGF, the more spread out the data points are over a wider range of values, meaning that almost round, to highly elongated, intersections of fibers are found in the cross-section of the microstructure of the sample with 20 wt% of EGF, with the elongation parameter values in some fibers even exceeding 25. By increasing the glass-fiber content, the mean elongation parameter of the EGF increases from 1.18 to 1.42 for 5 and 20 wt% of EGF, respectively.

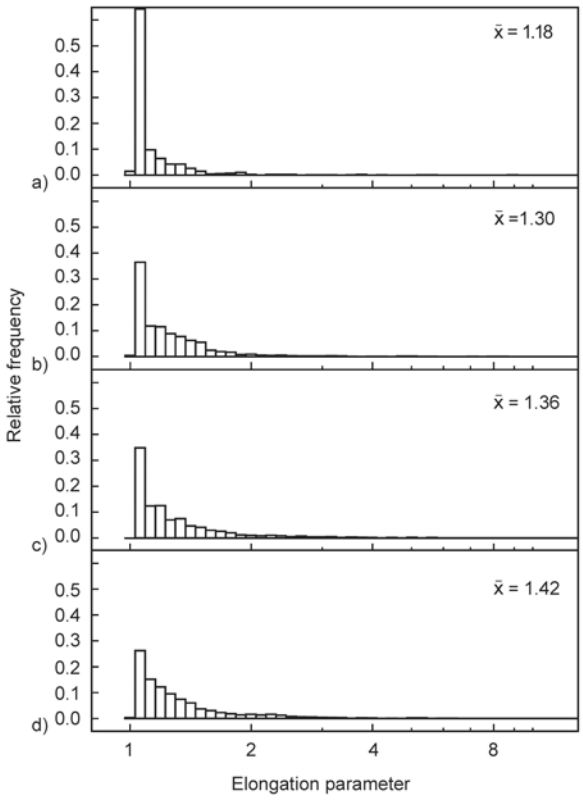

Figure 7. Distribution and mean values of the elongation parameter in the cross-section microstructures of the composites: a) 5 wt%, b) 10 wt%, c) 15 wt% and d) 20 wt% of EGF

3.2. Mechanical properties

3.2.1. Flexural strength

The flexural strength, the standard deviation, the relative standard deviation and the flexural modulus for the BMC composites with different EGF contents are presented in Table 2. It is evident that with increasing glass-fiber content the flexural strength increases from 73.4 to 108.8 MPa for the samples with 5 wt% of EGF and 10 wt% of EGF, respectively, reaching a maximum value of 121.0 MPa for the composite with 15 wt% of EGF, thus showing the effectiveness of the reinforcement given by the EGF. With a further increase of the EGF content the flexural strength decreases to 95.8 MPa, i.e., for the sample with 20 wt% of EGF. However, an increase in the flexural strength, to some degree, of the composites was expected. It seems that at higher weight fractions, the number of contacts between the fibers increases, thus it may affect the effective stress transfer in the material and, consequently cause a flexural strength reduction that we observed in our samples.

The clustering of fibers and the increased fiber-fiber interactions at higher fiber contents were also observed in the SEM micrographs (see Figure 5). This is especially apparent in the composite with 20 wt% of EGF, where the flexural strength was reduced. The results of the flexural strength measurements can be related to the degree of fiber-distribution homogeneity in the individual composites, as previously indicated in Figure 5 by the RDF. The values of the relative standard deviation for the composites with 15 and 20 wt% of EGF indicate an uneven load capacity, since they are higher (RSD > 10%) than for the composites with a lower EGF fraction. The composite with 10 wt% of EGF has the smallest value of the relative standard deviation, i.e., 3.3%, (see Table 2) suggesting the most uniform stress transfer between the fibers. The presence of differently oriented fibers in the microstructure, as evidenced by the increased elongation factor (see Figure 7), could locally increase the stress, which could affect the interfacial de-bonding and brittle-matrix cracking and could be responsible for the less effective mechanical performance of the composite material. Furthermore, it is important to note that at lower weight fractions of the EGF, below 10 wt%, there are not enough fibers to reinforce the PM and to achieve sufficient mechanical strength. Flexural modulus of all BMC composites is increasing with fiber content from 15.2 to 16.9 GPa for 5 and 20 wt% of EGF, respectively.

3.2.2. Dynamic mechanical analysis

In order to study the mechanical response of the composites with different weight portions of EGF, a DMA was performed with the aim being to correlate the obtained results with the microstructural analyses. The composite without EGF (0 wt% EGF, 79 wt% $CaCO_3$) was additionally analyzed to obtain a better insight into how the viscoelastic properties change with the fiber loading. The temperature dependence of the storage modulus (E'), the loss modulus (E'') and the damping behavior ($\tan\delta$) for all the BMC composites are shown in Figure 8. Evidently, the composites' storage moduli increased with the addition of the EGF to the host PM across the entire temperature range due to the increase in the material stiffness. The coefficient of reinforcement, calculated using Equation (6):

$$C = \frac{\left(\frac{E'_G}{E'_R}\right)_{composite}}{\left(\frac{E''_G}{E'_R}\right)_{PM+minereal\ filter}} \quad (6)$$

where E'_G and E'_R are the storage-modulus values in the glassy and rubbery regions, respectively, was used to evaluate the extent of the reinforcing action. According to the theory, the lower the value of C is, the greater is the reinforcement. The calculations (see Table 2) revealed that the sample with 15 wt% of EGF has the lowest C coefficient and therefore the highest reinforcement.

The temperature dependence of the loss modulus is shown in Figure 8b). Below the glass-transition temperature (T_g) the loss modulus increases with increasing EGF content up to 15 wt%, which is indicative of better packing of the fibers in the PM and their effective coupling. The T_g, when determined as the peak value of the loss modulus curves, is about 85–96 °C for all the composites. Above the T_g, a sharp decrease is observed, which is assigned to the enhanced movement of the polymer chains. In the case of the composite with 20 wt% of EGF the deviation from the trend is attributed to the increased fiber-fiber interactions that can lead to faults in the material and deterioration of the mechanical properties.

As shown in Figure 8c), the damping factor for all the composites ($\tan\delta$) increases with the increasing temperature. All the curves reach a peak in the temperature range from 91 to 113 °C (T_g), see Table 2 According to [23], the incorporation of fibers in the PM should lower the $\tan\delta$ peak due to the greater restriction of the polymer chains caused by the presence of fibers. In contrast to the literature, here the

Table 2. Flexural strength, (σ_f), standard deviation, (SD), relative standard deviation, (RSD) and flexural modulus, (E_f), of the BMC composites. In the bottom part of the table is listed the coefficient of reinforcement (C) obtained from the storage modulus (DMA analysis) and T_g values of all BMC composites determined from the $\tan\sigma$ curves

	Weight content of EGF [wt%]				
	0	**5**	**10**	**15**	**20**
σ_f [MPa]		73	109	121	96
SD		5.4	3.6	15.3	9.8
RSD [%]		7.4	3.3	12.6	10.2
E_f [GPa]		15.2	15.4	16.7	16.9
	DMA				
C		0.86	0.85	0.79	0.87
T_g [°C]	99	101	94	91	113

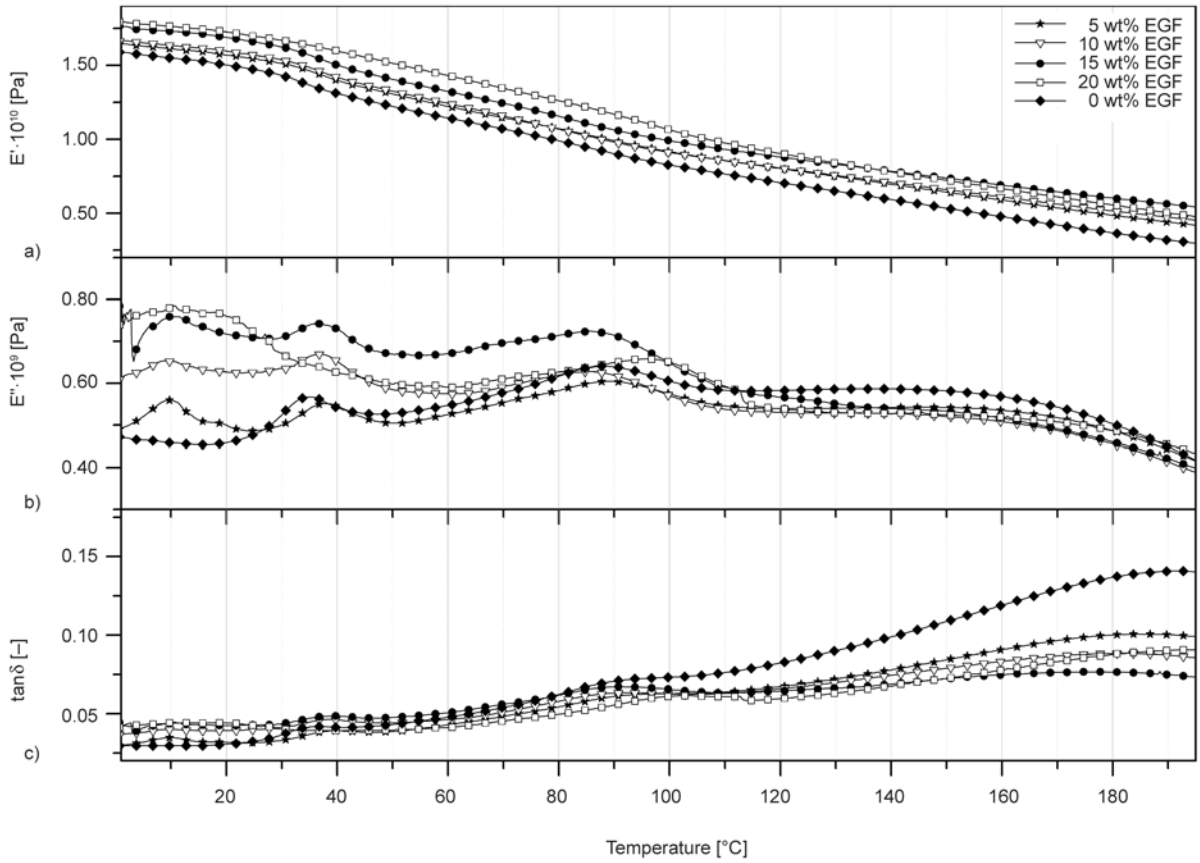

Figure 8. a) storage modulus (E'), b) loss modulus (E'') and c) damping behavior ($\tan\delta$) for all the BMC composites

opposite was observed for the composites with 15, 10 and 5 wt% of EGF, which is probably influenced by the presence of $CaCO_3$ mineral filler.

4. Conclusions

Different characterization techniques were used to analyze the EGF distribution in the polymer matrix in order to obtain a better insight into how the degree of the fibers' order/disorder and their orientation influence the mechanical properties of fiber-reinforced composites. Methodologies and computational techniques such as the Dirichlet tessellation and the RDF were considered during a quantitative characterization of the composites, where a set of criteria was used to determine whether the simulated microstructures are, to some degree, equivalent to the experimental observations and to link the microstructural changes with the composite properties, i.e., the flexural strength, storage modulus, loss modulus and damping behavior.

According to the results of the RDF analyses the experimental fiber distribution approaches the ideal fiber distribution with increasing distances and is reached more quickly at low weight fractions of the EGF. It was shown that the fiber distributions in the composites with 5 and 10 wt% EGF most closely approximate the values of ideal random fiber distributions. Consistent results were obtained from histograms of the relative frequency of the Voronoi diagrams, where the divergence of the experimental fiber distribution from the ideal one is more pronounced at higher fiber contents, i.e., above 15 wt%. Such results indicate that for higher fiber contents the fibers are clustered together, resulting in areas where the distances between the fibers are only locally equidistant. Such a microstructural inhomogeneity then affects and deteriorates the mechanical properties: increased fiber-fiber interactions lead to a less effective stress transfer between the fibers. The flexural strength of the composites increased with increasing EGF content, but only up to a certain point. The highest value was measured for the composite with 15 wt% of EGF. The coefficient of reinforcement showed an optimum value for the composite with 15 wt% of EGF. We can conclude that the right balance of properties, i.e., a high degree of fiber distribution homogeneity and a suitable mechanical performance can be achieved by tailoring the EGF con-

tent for a selected composite formulation. Furthermore, such quantitative analysis of the microstructure of BMC composites could be applied for obtaining information about the mechanical response of complex parts of BMC products.

Acknowledgements

BB gratefully acknowledges the financial support of the Ministry for Education, Science and Sport of the Republic of Slovenia and the European Commission through the European Social Fund. BM and KV acknowledge the financial support of the Slovenian Research Agency (research program P2-0105), and EŽ and MH (program P2-0145).

References

[1] Burns R.: Polyester molding compounds. Marcel Dekker, New York (1982).

[2] Monk J. F.: Thermosetting plastics: Moulding materials and processes. Longman, Harlow (1997).

[3] Harper L. T., Turner T. A., Warrior N. A., Dahl J. S., Rudd C. D.: Characterisation of random carbon fibre composites from a directed fibre preforming process: Analysis of microstructural parameters. Composites Part A: Applied Science and Manufacturing, **37**, 2136–2147 (2006).
DOI: 10.1016/j.compositesa.2005.11.014

[4] Sreenivasan V. S., Ravindran D., Manikandan V., Narayanasamy R.: Mechanical properties of randomly oriented short *Sansevieria cylindrica* fibre/polyester composites. Materials and Design, **32**, 2444–2455 (2011).
DOI: 10.1016/j.matdes.2010.11.042

[5] Guild F. J., Summerscales J.: Microstructural image analysis applied to fibre composite materials: A review. Composites, **24**, 383–393 (1993).
DOI: 10.1016/0010-4361(93)90246-5

[6] Avérous L., Quantin J-C., Lafon D., Crespy A.: Morphological determinations of fiber composites. Microscopy Microanalysis Microstructures, **7**, 433–439 (1996).
DOI: 10.1051/mmm:1996142

[7] Zangenberg J., Larsen J. B., Østergaard R. C., Brøndsted P.: Methodology for characterisation of glass fibre composite architecture. Plastics, Rubber and Composites, **41**, 187–193 (2012).
DOI: 10.1179/1743289811Y.0000000067

[8] Voronoi G.: Nouvelles applications des paramètres continus à la théorie des formes quadratiques. Deuxième mémoire. Recherches sur les parallélloèdres primitifs. (in French). Journal für die reine und angewandte Mathematik, **134**, 198–287 (1908).

[9] Voronoi G.: Nouvelles applications des paramètres continus à théorie des formes quadratiques. Deuxième mémoire. Recherches sur les paralléloèdres primitifs. (in French). Journal für die reine und angewandte Mathematik, **136**, 67-182 (1909).

[10] Brostow W., Castaño V. M.: Voronoi polyhedra as a tool for dealing with spatial structures of amorphous solids, liquids and gases. Journal of Materials Education, **21**, 297–304 (1999).

[11] Medvedev N. N., Geiger A., Brostow W.: Distinguishing liquids from amorphous solids: Percolation analysis on the Voronoi network. Journal of Chemical Physics, **93**, 8337–8342 (1990).
DOI: 10.1063/1.459711

[12] Kalogeras I. M., Hagg Lobland H. E.: The nature of the glassy state: Structure and transitions. Journal of Materials Education, **34**, 69–94 (2012).

[13] Heijman M. J. G. W., Benes N. E., ten Elshof J. E., Verweij H.: Quantitative analysis of the microstructural homogeneity of zirconia-toughened alumina composites. Materials Research Bulletin, **37**, 141–149 (2002).
DOI: 10.1016/S0025-5408(01)00806-6

[14] Trefalt G., Benčan A., Kamplet M., Malič B., Seo Y., Webber K. G.: Evaluation of the homogeneity in $Pb(Zr,Ti)O_3$–zirconia composites prepared by the hetero-agglomeration of precursors using the Voronoi-diagram approach. Journal of the European Ceramic Society, **34**, 669–675 (2014).
DOI: 10.1016/j.jeurceramsoc.2013.09.014

[15] Summerscales J., Guild F. J., Pearce N. R. L., Russell P. M.: Voronoi cells, fractal dimensions and fibre composites. Journal of Microscopy, **201**, 153–162 (2001).
DOI: 10.1046/j.1365-2818.2001.00841.x

[16] Sun Z., Zhao X., Ma J.: Characterization of microstructures in sisal fiber composites by Voronoi diagram. Journal of Reinforced Plastics and Composites, **32**, 16–22 (2012).
DOI: 10.1177/0731684412461191

[17] Ghosh S., Nowak Z., Lee K.: Quantitative characterization and modeling of composite microstructures by Voronoi cells. Acta Materialia, **45**, 2215–2234 (1997).
DOI: 10.1016/S1359-6454(96)00365-5

[18] Pyrz R., Bochenek B.: Topological disorder of microstructure and its relation to the stress field. International Journal of Solids and Structures, **35**, 2413–2427 (1998).
DOI: 10.1016/S0020-7683(97)00140-6

[19] Pinheiro A., Mano J. F.: Study of the glass transition on viscous-forming and powder materials using dynamic mechanical analysis. Polymer Testing, **28**, 89–95 (2009).
DOI: 10.1016/j.polymertesting.2008.11.008

[20] Budai Z., Sulyok Z., Vargha V.: Glass-fibre reinforced composite materials based on unsaturated polyester resins. Journal of Thermal Analysis and Calorimetry, **109**, 1533–1544 (2012).
DOI: 10.1007/s10973-011-2069-5

[21] Devi L. U., Bhagawan S. S., Thomas S.: Dynamic mechanical analysis of pineapple leaf/glass hybrid fiber reinforced polyester composites. Polymer Composites, **31**, 956–965 (2010).
DOI: 10.1002/pc.20880

[22] Idicula M., Malhotra S. K., Joseph K., Thomas S.: Dynamic mechanical analysis of randomly oriented intimately mixed short banana/sisal hybrid fibre reinforced polyester composites. Composites Science and Technology, **65**, 1077–1087 (2005).
DOI: 10.1016/j.compscitech.2004.10.023

[23] Romanzini D., Lavoratti A., Ornaghi Jr H. L., Amico S. C., Zattera A. J.: Influence of fiber content on the mechanical and dynamic mechanical properties of glass/ramie polymer composites. Materials and Design, **47**, 9–15 (2013).
DOI: 10.1016/j.matdes.2012.12.029

[24] Almeida Júnior J. H. S., Ornaghi Júnior H. L., Amico S. C., Amado F. D. R.: Study of hybrid intralaminate curaua/glass composites. Materials and Design, **42**, 111–117 (2012).
DOI: 10.1016/j.matdes.2012.05.044

[25] ISO 3167: Plastics. Multipurpose test specimens (2002).

[26] Járai-Szabó F., Néda Z.: On the size distribution of Poisson Voronoi cells. Physica A: Statistical Mechanics and its Applications, **385**, 518–526 (2007).
DOI: 10.1016/j.physa.2007.07.063

[27] Allen M. P., Tildesley D. J.: Computer simulation of liquids. Clarendon Press, Oxford (1989).

[28] Frenkel D., Smit B.: Understanding molecular simulation: From algorithms to applications. Academic Press, San Diego (2001).

[29] ISO 178: Plastics. Determination of flexural properties (2003).

[30] Everett R. K.: Quantification of random fiber arrangements using a radial distribution function approach. Journal of Composite Materials, **30**, 748–758 (1996).
DOI: 10.1177/002199839603000606

eXPRESS Polymer Letters Vol.10, No.6 (2016) 506–524
Available online at www.expresspolymlett.com
DOI: 10.3144/expresspolymlett.2016.48

'Containers' for self-healing epoxy composites and coating: Trends and advances

P. Vijayan[1*], *M. A. AlMaadeed*[1,2]

[1]Center for Advanced Materials, Qatar University, P.O. Box 2713, Doha, Qatar
[2]Materials Science and Technology Program, Qatar University, P.O. Box 2713, Doha, Qatar

Received 6 November 2015; accepted in revised form 14 January 2016

Abstract. The introduction of self-healing functionality into epoxy matrix is an important and challenging topic. Various micro/nano containers loaded self-healing agents are developed and incorporated into epoxy matrix to impart self-healing ability. The current report reviews the major findings in the area of self-healing epoxy composites and coatings with special emphasis on these containers. The preparation and use of polymer micro/nano capsules, polymer fibers, hollow glass fibers/bubbles, inorganic nanotubes, inorganic meso- and nano-porous materials, carbon nanotubes etc. as self-healing containers are outlined. The nature of the container and its response to the external stimulations greatly influence the self-healing performance. The self-healing mechanism associated with each type of container and the role of container parameters on self-healing performance of self-healing epoxy systems are reviewed. Comparison of the efficiency offered by different types of containers is introduced. Finally, the selection of containers to develop cost effective and green self-healing systems are mentioned.

Keywords: *smart polymers, epoxy, self-healing, coating*

1. Introduction

Excellent adhesion, high mechanical strength, high thermal stability and high chemical and corrosion resistance of epoxy make this material suitable for versatile applications like structural adhesives, protective coatings and resin matrices for composites [1]. However, as an inherently brittle material, epoxy thermosets are highly susceptible to defects/cracks [1–3]. Fracture/fatigue loadings, thermal effects or any kind of environmental effects influence the matrix service life. In general, the material failure starts at nano-scale, which then enlarges to micro- and then to macro-scale until failure occurs. It is difficult to detect and repair these micro/nano cracks formed in the structural components [4]. Hence, it is promising to develop self-healing epoxy composites that can repair damages by themselves without any external intervention to recover their functions. In a similar way, the introduction of self-healing functionality into protective coating is a better alternative for a long-term corrosion protection of metallic structures by eliminating toxic chromate based coatings. The self-healing coating provides an active protection to the metallic surface not only by mechanical covering but also by protection even after partial damage of the coating [5–7]. In self-heling coatings controlled release of the corrosion inhibitor has been triggered by the changes in local environment (change in pH).

The development of self-healing technology for epoxy materials attracted growing interest and various methods have been reported based on healing agents, healing agent containers, healing mechanisms etc. A great deal of attention has been paid to design self-healing epoxy after their first introduction in 2001 by White *et al*. [8]. In this breakthrough

*Corresponding author, e-mail: poornimavijayan@qu.edu.qa

self-healing concept, healing agent (dicyclopentadiene) encapsulated inside a poly (urea-formaldehyde) microcapsule reacted with a catalytic chemical trigger (Grubbs' catalyst) within epoxy matrix to provide self-healing ability. The successive reports on self-healing epoxies, disclosed various combination of self-healing components and healing mechanisms. Among them, the containers to encapsulate the healing agent have been investigated widely. These containers are specially designed to release the loaded healing agents in case of the failure of the epoxy structure due to any kind of external stimulus. The nature of the container such as the material, morphology, shell wall thickness, storage stability, core content etc. and its response to the external stimulations are of great importance in determining the self-healing performance. The external stimulation to trigger the release of healing agent from the containers includes light, mechanical impact, local change in pH during the corrosion process etc.

Self-healing polymers are subject to intense discussion in the scientific community during the last decade [9–11]. The studies on micro/nanocapsules used for self-healing coatings were reviewed by Samadzadeh *et al*. [12]. Wu *et al*. [13] reviewed the trends and developments in self-healing polymeric materials including preparation and characterization of the self-healing systems, evaluation of self-healing efficiencies in thermoplastic and thermoset materials. Yang *et al*. [14] reviewed different aspects of self-healing polymers including the thermodynamic requirements and chemical reactions for self-healing, encapsulation process, remote self-healing etc. A specific area in self-healing polymers i.e. container based self-healing polymer coatings wase reviewed by Shchukin [15]. Fayyad *et al*. [16] discussed in detail different techniques used to follow the self-healing process in protective epoxy coatings. However, the absence of a systematic review in the area self-healing epoxy in specific, make the current review unique, which focuses on self-healing agent loaded containers used in epoxy matrix.

The present review aims to report the investigations on the development and use of various micro/nano containers for epoxy composites and coatings. An ideal self-healing container should be resistant to solvents, temperature and mechanical stresses such as mixing, curing etc. during the manufacturing processes by maintaining the healing agents inside. At the same time, the container should break upon propagation of cracks through the matrix and release enough healing agents to recover the crack. Extensive research works were reported to achieve containers which fulfill these criteria. Researchers used different types of self-healing agent loaded containers with hollow cavity of different shapes including polymer capsules, polymer fibers, hollow glass fibers and capsules, inorganic capsules and tubes etc. in the size range from micro to nano. Figure 1 shows containers of different origin which are capable of loading healing agents inside their cavity. The influence of container parameters on the self-healing performance is reviewed in detail. The potential of inorganic nanotubes, mesoporous materials and carbon nanotubes materials to act as multifunctional containers for epoxy is proposed.

2. Polymer capsules as self-healing agent containers

2.1. Preparation of polymer microcapsules

In situ emulsion polymerization, interfacial polymerization, vacuum infiltration etc. are used to prepare the polymer microcapsules. Among them *in situ* emulsion polymerization is the most widely used method for the preparation of polymer microcapsules. Different types of liquid healing agents such as

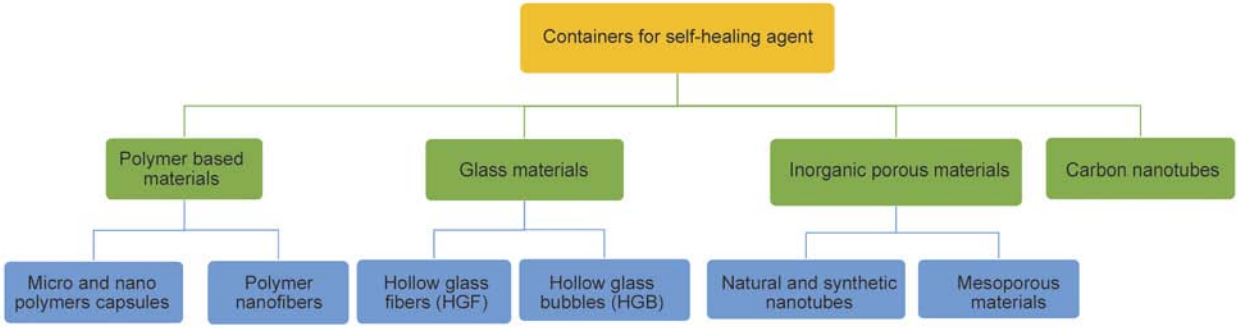

Figure 1. Containers of different origin capable of loading healing agents inside

dicyclopentadiene (DCPD), organic solvents, epoxy resin, curing agents and drying oils are encapsulated inside polymeric shells like poly (urea-formaldehyde) (PUF), poly (melamine-formaldehyde) (PMF) etc. using *in situ* polymerization reaction [17]. White and coworkers [8, 18] prepared DCPD encapsulated PUF microcapsules in oil-in-water emulsion. The processing parameters like agitation speed, temperature, emulsifier concentration etc. can influence the morphology, shell wall parameters, size distribution, storage stability and core content of these microcapsules.

The procedure adopted by White and coworkers [8, 18] was also extended to encapsulate other healing materials in PUF shell. Organic solvents encapsulated polymer capsules were prepared by researchers. Chlorobenzene was encapsulated in PUF shell using *in situ* polymerization method with an average diameter of 160±20 μm [19]. In an advanced attempt, co-encapsulation of epoxy monomer with solvents in PUF shells were done by dissolving epoxy resins in solvents before adding to the emulsion mixture [19, 20]. Drying oil encapsulated microcapsules, specifically designed for self-healing epoxy coatings, were also generated by *in situ* polymerization [21].

The self-healing based on DCPD or solvent encapsulated microcapsules make use of chemistries which are different from that of the matrix. This might result in deterioration of the mechanical properties of the healed area. So researchers found methods for the safe encapsulation of both epoxy resin and curing agent. While using epoxy as reactive healing agent, the microencapsulation of epoxy monomer was done by a two-step process [22]. Initially, urea and formaldehyde were pre-polymerized and then formed microcapsules via *in situ* condensation. In another attempt, epoxy was encapsulated in an epoxy shell itself [23]. Liu *et al*. [23] prepared microcapsules with epoxy as the core healing agent and epoxy-amine polymer as the shell by interfacial polymerization of epoxy resin droplets with ethylenediamine (EDA). The reaction of epoxy which cannot be dissolved in water with EDA which is readily dissolved in water at the interface of epoxy droplets to form the shell material.

Though it is easy to achieve the epoxy encapsulation, encapsulation of liquid amine hardeners is difficult due to their amphoteric nature and high reactivity. The conventional amine hardener could not encapsulate by urea-formaldehyde shell under acidic conditions. Researchers chose mercaptan as curing agent suitable for encapsulation purpose [24, 25]. Since mercaptan is very active, it was microencapsulated with melamine-formaldehyde by an improved *in situ* polymerization approach. The mercaptan-loaded PMF capsules showed high storage stability. The catalyst was infiltrated into the mercaptan-loaded PMF capsules, to produce microcapsules containing both mercaptan and its amine catalyst.

Later, a new method to encapsulate amine hardeners was introduced [26]. In this method diethylenetriamine was infiltrated into hollow PUF microcapsules using vacuum process. Initially, hollow PUF microcapsules were prepared by a poly-condensation reaction of urea-formaldehyde pre-polymer on the surface of entrained air bubbles. These hollow capsules were immersed in diethylenetriamine and carried out the vacuum infiltration for several hours to encapsulate the amine inside the PUF capsules.

In an another attempt, polyetheramine, a flowable and low temperature curable curing agent was successfully encapsulate in poly(methylmethacrylate) (PMMA) shell [27]. In this case, PMMA microcapsules were prepared by a controlled phase separation process within droplets of an oil-in-water (O/W) emulsion. Successively, the solvent evaporation technique was employed to form a PMMA shell around the polyetheramine core.

Very recently, a facile method of preparation of microcapsules based on Pickering emulsion, in which the solid particles adsorbed on oil-water interface instead of surfactants in traditional emulsion was introduced [28, 29]. Soild particles like nanoclay and lignin are remarkably stable to protect droplets from aggregation. Yi *et al*. [29] used cheap and eco-friendly material-lignin as Pickering emulsion stabilizer and the active hydroxyl groups in the chemical structure of lignin could react with isocyanate groups in oil phase and reinforced the stability of emulsions. Isophorone diisocyanate, (IPDI) was effectively loaded in lignin nanoparticle-stabilized oil-in-water (O/W) Pickering emulsion templates (Figure 2).

2.2. Preparation of polymer nanocapsules

To develop thin polymer coating, the incorporation of nanocapsules is better choice than microcapsules. The possible lower capsule diameter limit of the PUF microcapsule developed by the *in situ* polymerization was 10 μm [8]. However, a combination of ultra-

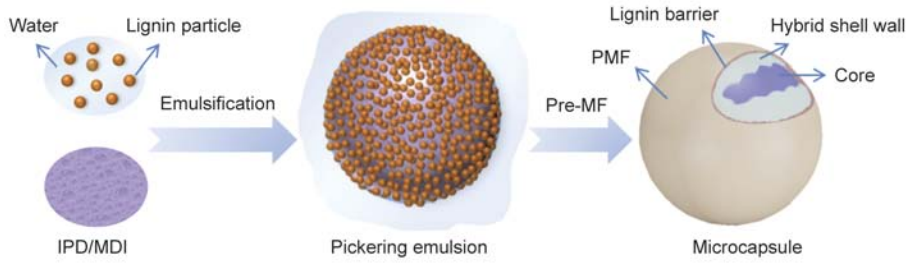

Figure 2. Schematic for the synthesis process of multilayer composite microcapsules loaded with healing agents based on Pickering emulsion templates [29]

sonication and *in situ* encapsulation techniques was used to produce submicron and nano PUF capsules filled with DCPD [30]. This method was reported to produce nano-capsules with smooth outer surface and thin shell walls.

Zhao *et al*. [31] introduced a general method to develop nanocapsules from polymers like poly (L-lactide) (PLLA), poly(vinyl acetate) (PVAc), poly (methyl methacrylate) (PMMA), poly(vinyl formal) (PVF) and poly(vinyl cinnamate) (PVCi) using combination of solvent evaporation and miniemulsion techniques. The steps involved in this process is shown in Figure 3. Initially, a homogeneous hydrophobic phase containing pre-synthesized polymer and healing agent in a good polymer solvent was ultrasonicated with aqueous surfactant solution, to obtain miniemulsion droplets. Further upon good solvent evaporation, the nanocapsule encapsulated with healing agent was formed through internal phase separation. This method can be applied to encapsulate hydrophobic healing agents like solvents and monomers, reflecting their use in self-healing epoxy systems.

2.3. Polymer capsules in epoxy composites

Polymer capsules are developed as self-healing containers to fracture along the crack to release the healing agent into the failure site. The understanding of the micromechanical properties of these encapsulated shells using nanoindentation technique can help in predicting the self-healing performance of microcapsule incorporated epoxy systems [32]. In addition to the ability to act as healing agent reservoirs, theses containers can also serve as a toughening agent for virgin epoxy. The detailed toughening mechanism operates in fluid filled PUF microcapsules embedded epoxy was investigated. The toughening mechanisms induced by these microcapsules are found to be different from that by solid particle fillers [33, 34]. The increased hackle marking and subsurface micro-cracking were identified in fluid-filled microcapsules incorporated epoxy. It was reported that the PUF microcapsules with optimal wall thickness (56±5 μm), diameter (400±50 μm) and surface morphology have the lower permeability and high stability. This makes them applicable to polymers fabricated at higher temperature (<250 °C) [35]. However, it was found that the presence of microcapsules caused a reduction in modulus and strength of the matrix [33, 24].

The self-healing epoxy system introduced by White *et al*. [8] used PUF microcapsules with thin shell to encapsulate DCPD as healing agent. When the crack propagates thorough the matrix, the embedded microcapsules ruptured to release the DCPD monomer into the crack. Grubbs catalyst embedded in the matrix initiated the polymerization of the released DCPD via ring-opening metathesis polymerization (ROMP)

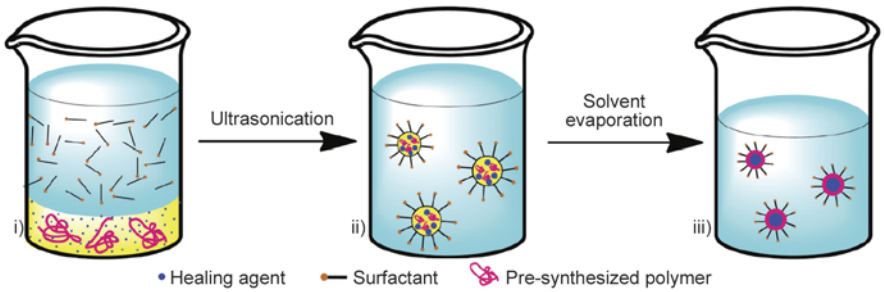

Figure 3. Schematic illustration of the general route towards fabrication of healing agent-filled nanocapsules from miniemulsions using pre-synthesized polymers [31]

to rebond the crack plane at room temperature. Figure 4a schematically shows the self-healing mechanism operates in encapsulated DCPD/Grubbs catalyst based self-healing epoxy systems. The scanning electron microscopic (SEM) image of ruptured PUF microcapsule is shown in Figure 4b. In this case, the self-healing process was found to influence the concentration and size of PUF microcapsules [36]. It was found that a lower capsule concentration of 5 wt% achieved a satisfactory healing. However, in this case, the size of the microcapsule did not show a prominent effect on fracture toughness (K_{IC}) and healing efficiency ($\eta = K_{IC}$ healed/K_{IC} virgin), even though the capsule size had a direct influence on the volume of DCPD monomer released. The fracture toughness per volume fraction of capsules was found to be higher for 1.5 μm capsules than for larger capsules (180 μm). The PUF nanocapsules synthesized by Suryanarayana *et al*. [21] were found to provide better compatibility with the matrix. The dispersion of DCPD filled PUF nanocapsules in epoxy matrix caused a significant increase in fracture toughness with a slight decrease of tensile strength.

The microcapsules made of urea-formaldehyde filled with DCPD was used in successive research to develop carbon fiber reinforced epoxy structural composites with self-healing ability [37]. The encapsulation of fluorescent dye along with DCPD into the melamine–urea–formaldehyde (MUF) shell was effectively used to observe the recovering process using fluorescence microscopy [38]. The transport of self-healing agent between crack planes released from a microcapsule were traced using fluorescence microscopy in cracked epoxy incorporated with MUF microcapsules containing DCPD with fluorescent dye.

The limitations of DCPD/Grubbs catalyst based self-healing system includes catalyst unavailability, cost, environmental toxicity, instability, and difficult materials processing could be eliminated by an economical and simple way of using encapsulated solvents to recover the virgin properties of epoxy system [19]. Chlorobenzene loaded PUF microcapsules were incorporated into the epoxy matrix. When a crack propagated through the material, the solvent was released upon cleavage of the capsules and healed the crack. The healing mechanism they proposed involved the local swelling of the matrix by the solvent which allowed the accessibility of residual amines and further crosslinking with residual epoxy functionality. The self-healing ability of the solvent-based system could be further improved by

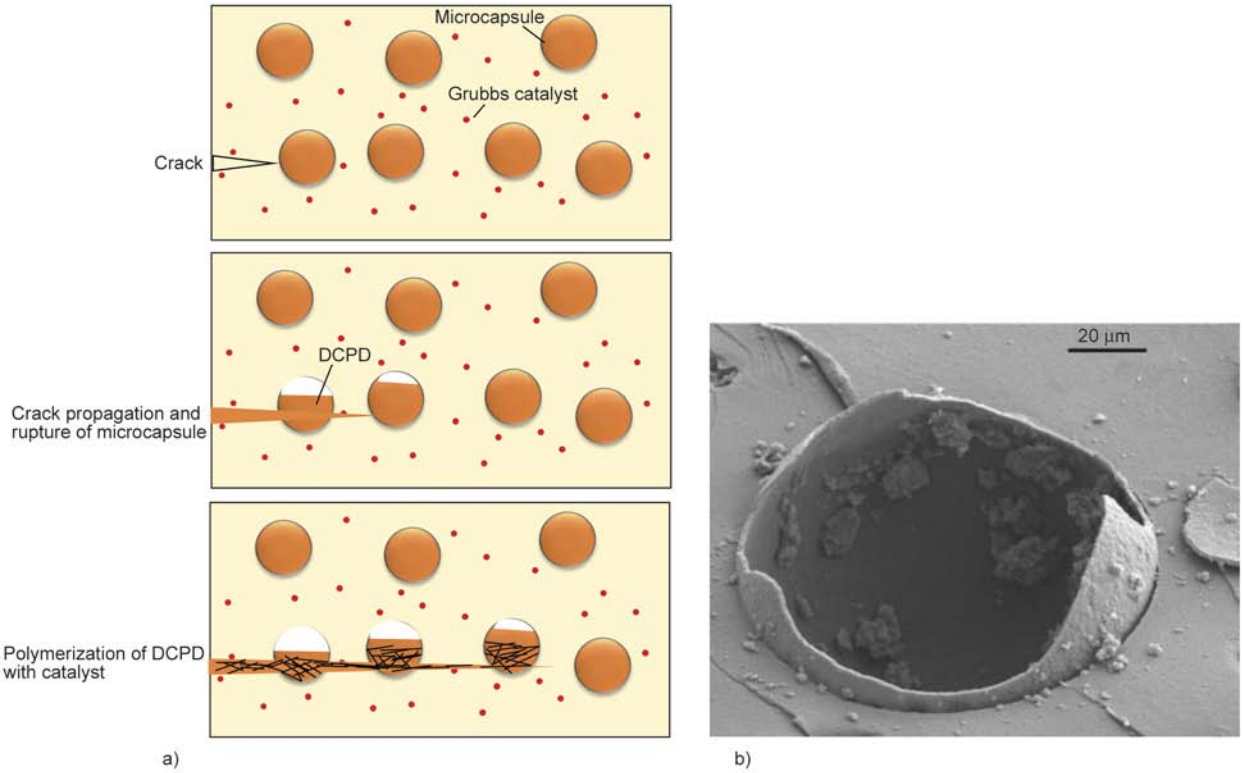

Figure 4. a) The schematic representation of self-healing concept introduced by White *et al*. in encapsulated DCPD/Grubb's catalyst based epoxy self-healing systems, b) scanning electron microscope image shows the fracture plane of a self-healing material with a ruptured PUF microcapsule in a thermosetting matrix [8]

using an epoxy monomer co-encapsulated with solvents [20, 39]. In such case, the additional epoxy monomer delivered to the crack plane provided additional crosslinking to have new thermoset material to the original matrix interface with multiple healing events. The solvent-based self-healing concept was extended to greener solvents like phenylacetate and ethyl phenylacetate [39, 40]. These aromatic ester are significantly less toxic solvents than chlorobenzene. Coope *et al*. [40] incorporated PUF microcapsule containing mixture of ethyl phenylacetate/epoxy mixture into scandium(III) triflate catalyst embedded epoxy. In this system, the epoxy monomer from the ruptured microcapsule undergoes ring-opening polymerization in contact with dispersed catalyst. Here the self-healing activity was promoted by the swelling of epoxy matrix by ethyl phenylacetate to facilitate catalyst dissolution.

The PUF encapsulated ethyl phenylacetate/epoxy mixture was used along with shape memory alloy wires in epoxy matrix to allow the healing of larger damage volumes [41, 42]. Here the use of shape memory alloy wires along with ethyl phenylacetate helped to reduce the crack face separation and provide internal heating to accelerate the healing kinetics.

Blaiszik *et al*. [20] demonstrated the influence of shell wall morphology on the microcapsule rupture based on the study carried out on PUF micro/nanocapsules containing a mixture of resin and solvent. The capsule shell wall was found to comprise of two distinct regions with a thin continuous inner shell wall of low molecular weight polymer that deposits at the oil–water interface formed by urea and formaldehyde reaction in aqueous phase, and a thicker rough exterior shell wall formed by coalesce the colloidal UF particles as the UF reaction progresses. When incorporating this microcapsule into epoxy matrix, the rough surface of the wall allowed a good adhesion to the epoxy matrix by increasing capsule fracture and healing agent delivery.

To provide a repair system with matching chemical entity with host epoxy matrix, researchers focused on the use of microcapsule encapsulated with epoxy and hardener. Yin *et al*. [22] developed a two-component healing system consisting of epoxy encapsulated PUF microcapsules (30–70 μm) and a latent hardener dissolved in epoxy. When cracks were propagated through the composites, the damaged microcapsule released the epoxy. The latent hardener which is soluble in the matrix encountered with released epoxy from the broken microcapsules to recover the crack upon curing at 130–180 °C.

Yuan and coworkers [24, 43] developed a self-healing epoxy system by incorporating both epoxy loaded and mercaptan loaded microcapsules. The size distributions of epoxy-loaded and hardener-loaded PMF capsules are shown in Figure 5a. This two-component self-healing epoxy with stoichiometric weight ratio (i.e. 1.26) of epoxy to mercaptan capsules offered maximum self-healing at or below room temperature with crack healing chemistry similar to the matrix polymer (Figure 5b). As the cracks propagate through the matrix, both type microcapsules fractured and successively released their contents. In the cracked surface, the epoxide groups quickly reacted with mercaptan in the presence of catalyst benzyldimethylamine to recover the matrix. The high flowability, fast consolidation and miscibility of the released epoxy and mercaptan facilitated rapid repair.

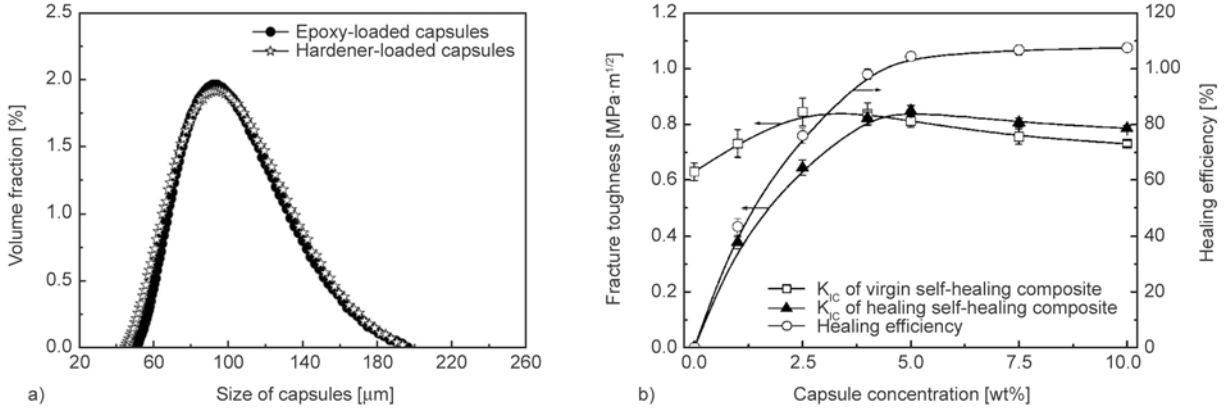

Figure 5. a) Size distribution of epoxy-loaded capsules and hardener-loaded capsules and b) influence of capsule concentration on fracture toughness and healing efficiency. Weight ratio of the two types of capsules in all the self-healing specimens is 1:1. Healing of the fractured specimens was conducted at 20 °C for 24 h [24].

Later, a two component epoxy self-healing system based on epoxy-amine healing chemistry was developed [26]. Both epoxy encapsulated capsules (produced by *in situ* polymerization) and amine encapsulated capsules (produced by the vacuum infiltration) in optimal ratio were incorporated into epoxy matrix. The reaction of epoxy and amine released from the respective capsules healed the damaged area. The healed fracture surfaces revealed that the healed matrix failed cohesively which indicated the *in situ* formation of epoxy and good bond strength to the matrix.

In recent studies, poly(methylmethacrylate) (PMMA) was chosen as the capsule shell as it has superior stability, biocompatibility and good compatibility with epoxy. Both one component PMMA microcapsules [27] and two component PMMA microcapsules [44] were investigated. The one component system [27] was designed in such a way that the released curing agent (polyetheramine) upon rupture of the PMMA shell crosslinked with the residual epoxy groups to form the new thermoset region in the original matrix interface. They found that the healing efficiency of the two-components system was higher than that of the single component self-healing system due to fast reaction occurred between the resin and the hardener leaked from the microcapsule to the crack surface. The effect of weight ratios of epoxy-/hardener-contained microcapsules on the healing efficiencies of epoxy composites was also investigated. It was observed that the self-healing efficiency significantly increased with increasing microcapsules content from 5 to 15 wt%. Increased microcapsule content helped to release enough epoxy and hardener to heal the cracks.

Very recently, nanocontainers with copolymer shell walls were developed as the functional copolymers containing oxirane function to match the epoxy structure as well as a second monomer to create fragility to fracture under crack [45]. Nanocontainers encapsulated with amine healing agent were prepared using poly (glycidylmethacrylate-*co*-methylmethacrylate) [poly(GMA-*co*-MMA)] via double emulsion technique.

The dual microcapsules were also used in glass fiber reinforced epoxy composites and studied the self-healing action upon low velocity impact damage [46]. Epoxy encapsulated PUF microcapsules (produced via *in situ* polymerization) and amine hardener encapsulated PUF microcapsules (produced via vacuum infiltration method) were properly mixed with epoxy in the ratio 10:3. Appropriate fabrication technique via hand layup followed by vacuum bag molding confirmed the protection of microcapsules in this glass fiber reinforced composite. In the crack area, the bleeding from microcapsules recovered the damaged area by formation of new bond.

As the weakest region in fiber reinforced polymer composite, the fiber/matrix interphase should require preferential self- repairing action [47]. The knowledge gained on bulk self-healing has also been transferred to the fiber/matrix interphase. Carbon fiber/epoxy interphases [48] and glass fiber/epoxy interphases [49] were functionalized with capsules containing reactive epoxy resin and ethyl phenyl acetate solvent to provide the interfacial self-healing upon debonding of the fiber/matrix interface.

During the progress of research in self-healing epoxy, scientists discovered methods to compensate the reduction in elastic modulus and hardness of the epoxy due to the presence of microcapsule by incorporating carbon nanotubes (CNTs), which was proved to improve the aforementioned values significantly [50]. Table 1 tabulated the healing efficiency obtained for epoxy composites with different polymer capsules.

2.4. Polymer capsules in epoxy coatings

The self-healing concept was also applied in epoxy coating besides in epoxy composites structures. Protective self-healing epoxy coatings are developed by incorporating containers, which are able to release a corrosion inhibitor or self-healing agents under the situations like pH changes caused by the triggering situations like start of corrosion process, ion-exchange process, and mechanical damage. Stankiewicz *et al*. [51] reviewed different type of self-healing coating for anti-corrosion applications. Drying oil encapsulated capsules such linseed oil encapsulated phenol-formaldehyde (PF) microcapsules [52] and tung oil encapsulated PUF microcapsules [53] were used to make self-healing epoxy coatings. Drying oils are chemically unsaturated glycerides of long chain fatty acids. When these oils contact with oxygen, carbon–carbon chain cleaved to polymerize and the degree of double bond unsaturation controls the polymerization rate. The linseed oil and tung oil released from microcapsules polymerized when contact with the air to heal the scratched area. Even though the chemical nature, physical and mechani-

Table 1. The healing efficiency reported for different type of containers

No.	Matrix	Containers	Self-healing agent	Self-healing efficiency	Ref.
1	Epoxy	PUF	Encapsulated DCPD/Grubbs catalyst	85±5% at room temperature	[36]
2	Epoxy/carbon fiber	PUF	Encapsulated DCPD/Grubbs catalyst	45% at room temperature 80% at 80 °C	[37]
3	Epoxy	PUF	Encapsulated chlorobenzene	82% at room temperature	[19]
4	Epoxy	PUF	Encapsulated phenyl acetate/ethyl phenyl acetate	100% at room temperature	[39]
5	Epoxy	PUF	Encapsulated epoxy/latent hardener	111% at 130–180 °C	[22]
6	Epoxy	PMF	Encapsulated epoxy/Encapsulated mercaptan based hardener	104% at 20 °C	[24]
7	Epoxy	PUF	Encapsulated epoxy (by *in situ* polymerization)/encapsulated amine hardener (by vacuum infiltration)	91% at room temperature	[26]
8	Epoxy	PMMA	Encapsulated epoxy/encapsulated amine hardener	84.5% at room temperature	[44]
9	Epoxy/glass fiber	PUF	Encapsulated epoxy (produced via *in situ* polymerization)/encapsulated amine hardener (produced via vacuum infiltration)	40% at room temperature	[46]
10	Epoxy	GMA-*co*-MMA	Encapsulated amine hardener	85% at room temperature	[45]
11	Epoxy	Electrospun PAN mats	Immersed epoxy/immersed amine	38% at room temperature	[61]
12	Epoxy	HGBs	Loaded epoxy/loaded amine	62% at 50 °C	[69]

cal characteristics of healed area are not the same as the matrix, the authors claimed that the creation of a barrier between air and surface could increase the life cycle of the coating. The corrosion resistance studies by electrochemical impedance spectroscopy (EIS) showed a better preservation of corrosion resistance of epoxy coating incorporated with tung oil encapsulated PUF microcapsule.

The encapsulated epoxy microcapsules were incorporated into epoxy paint composed of epoxy and modified polyamide hardener to prepare self-healing coating for carbon steel [23]. The capsules were ruptured along with the damage on the coating and the stored epoxy resin released into the matrix. The released epoxy polymerized when contacting with the residual polyamide hardener after curing of the epoxy in matrix, to repair the scratch. The EIS studies were used to evaluate the self-healing activity of epoxy microcapsules filled epoxy coating on carbon steel. These microcapsules were found to heal the scratched coating surface in a short time. Coating with an optimum concertation of epoxy microcapsules (20 wt%) completely healed the scratched surface with in 4 hrs. Also, these epoxy microcapsules were later used in epoxy/polyamide coatings for mild carbon steel for self-healing performance along with polyaniline nanofibers for passive property [54].

In epoxy protective coatings, solvents used to lower resin viscosity and heat treatment used to remove solvent or to cure coating matrix adversely affect the stability of the microcapsules. Hence solvent and thermal resistant microcapsule are practically required for self-healing epoxy coatings. A novel double-layered polyurea microcapsules containing hexamethylene diisocyanate (HDI) with excellent shell tightness synthesized via interfacial polymerization reaction showed good resistance to temperature and nonpolar solvents [55]. These HDI encapsulated double-layered polyurea microcapsules showed outstanding anticorrosion performance through self-healing functionality of the released HDI in damaged locations.

The epoxy coating loaded with these multilayer composite microcapsules based on Pickering emulsion had excellent anticorrosive and self-healing performance. This was confirmed from the optical images of the scratched coating with and without microcapsule loading (Figure 6). This cheaper and greener approaches adopted for the self-healing technology pave way for further use in industrial and environmental fields.

3. Polymer fibers as self-healing agent containers

Polymer fibers were also found as effective healing agent containers in epoxy matrix. Different methods were adopted to encapsulate the healing agents inside these polymer fibers including coelectrospinning [56–58], emulsion electrospinning [56] and emulsion solution blowing [56]. DCPD enwrapped into polyacrylonitrile (PAN) using coelectrospin-

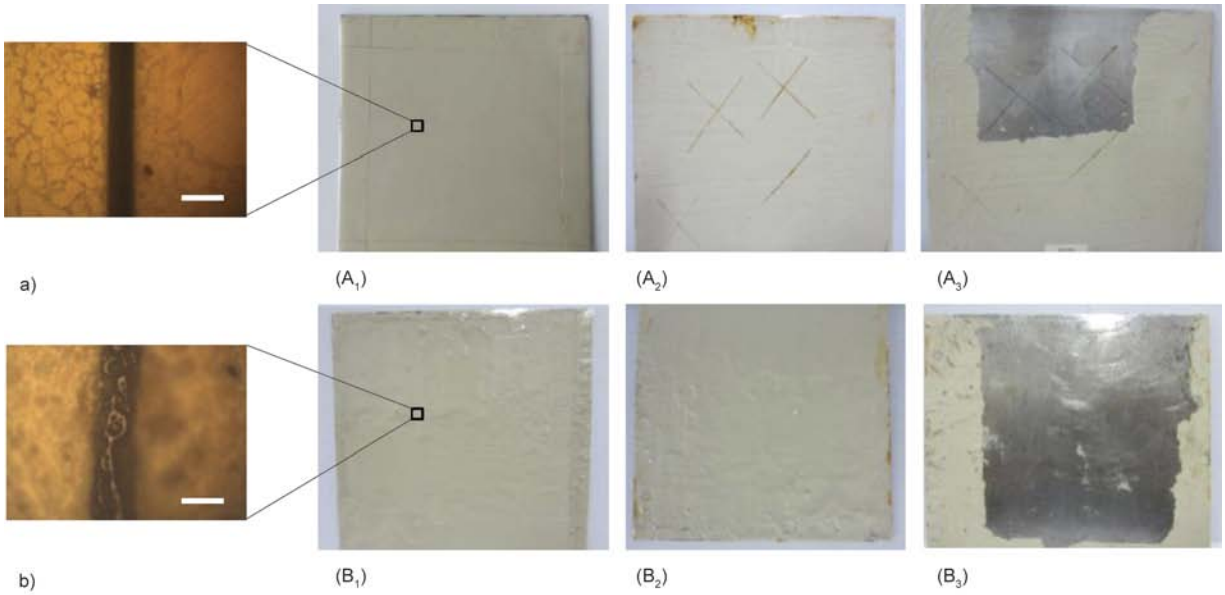

Figure 6. Brine-submersion corrosive-accelerating test. Photograph of steel plates coated with common coating (Group A) and multilayer microcapsules based on Pickering emulsion -embedded self-healing coating (Group B): (A_1, B_1) before, (A_2, B_2) after submersed in 10 wt% NaCl solution for 120 h, and (A_3) traces of corrosion on steel plate, (B_3) anticorrosive performance of self-healing coating on steel plate. OM images of enlarged view of scratched region on (a) common coating and (b) self -healing coating, the scale bars are 200 μm. The steel plates (10×10 cm^2) were submerged in NaCl solution (10 wt%) for 120 h [29].

ning to form core-shell DCPD/PAN nanofibers [56, 57]. The electrospinning was carried out in a lab-made coaxial needle setup for generating the core–shell jet [59, 60] by supplying a solution of 10 wt% PAN in dimethyl formamide (DMF) as the outer jet (shell) and the solution of 10 wt% DCPD in DMF as the inner jet (core). Self-healing carbon-fiber/epoxy composites were developed by incorporating this core-shell DCPD/ PAN nanofibers at laminate interfaces. Epoxy monomer was also encapsulated within a poly(vinyl alcohol) (PVA) nanofiber using coelectrospinning [58]. Thus obtained core-shell epoxy/ PVA nanofibers was found to be stable enough within the curing epoxy matrix.

In a different approach, as-electrospun mats of polyacrylonitrile (PAN) containing both epoxy and amine as healing solutions were embedded into an epoxy matrix [61]. Here, the healing agents were not subjected to encapsulation or electrospinning process as in the previous case and hence this technique could be implemented to carry reactive healing agents without tedious process. The electrospun PAN mats were simply immersed in liquid epoxy solution or diethylenetriamine (DETA) and were alternatively layered up in epoxy composite structure. Thus generated composites structures achieved multiple healing cycles. This method open up a way to the mass production of self-healing composites for structural applications.

4. Hollow glass fibers (HGF) and hollow glass bubbles (HGB) as self-healing agent containers

The high chemical inertness as well as thermal stability of hollow glass based self-healing containers offers advanced self-healing technology which can eliminate the limitations of corrosive feature of some healing agents and thermally degradability of the shell. The hollow glass fibers can be used as an ideal medium for storing healing components together with exploring them as structural reinforcing agents in advanced epoxy composite structures [62–65]. Hollow glass fibers with external diameter of 60 μm and 50% hollow fraction was used by Pang and Bond [62] to restore the healing components. They incorporated the unidirectional hollow glass fibers in epoxy matrix with 0°/90° lay-up. A significant fraction of flexural strength lost after impact damage was found to be restored by the self-healing action of resin and hardener stored within hollow fibers. The self-healing mechanism operates in this systems is similar to bleeding mechanism in biological organisms. During a damage event, healing agent passed from within any broken hollow fibers infiltrated the damage area.

These HGF were also incorporated into carbon fiber reinforced epoxy in order to impart the self-healing ability to carbon fiber reinforced polymer (CFRP) laminates used in aerospace applications [66]. It was found that the presence of HGF within a CFRP laminate produce minimal degradation in flexural strength and ply disruption. Recently, much thinner hollow glass fibers (13 μm outer diameter) were used in a damage-detecting and self-repairing epoxy composite to ensure major reinforcement [67]. Self-repair in this system was achieved by adding polyester resin (catalyzed resin and initiator) to the hollow fibers. When compared to the filled–damaged specimens, the healed specimens had 20 and 26% higher bending strength and bending modulus respectively.

Etched HGB are found to be another stable container for amine curing agent. Etched HGB with holes at the micrometer level were fabricated by etching the glass bubbles using dilute hydrofluoric acid (HF) in specially designed mixer. [68]. Etched HGB in micrometer range (diameter 66.9±8.2 μm, and shell thickness 0.79±0.41 μm) were used to encapsulate both epoxy resin and the amine hardener [69]. The healing agents inside the HGB survived from the manufacturing process and following 24 hour of cure. These healing agent containers were incorporated in the optimized ratio of 4:1 for epoxy loaded HGBs to amine loaded HGBs to get better self-healing performance.

5. Inorganic nanomaterials as self-healing agent containers

When compared with tedious encapsulation process required in the case of most of the polymer capsules, merely 'physical' encapsulation generally vacuum infiltration is required in the case of these inorganic nanomaterials which make this self-healing technique more demanding to heal the micro-crack. Even though there are some reports on the use of inorganic nanoporous and nanotubes as self-healing containers, still more detailed investigations are required in this area. Like polymer capsules, the inorganic containers also offer mechanical reinforcement apart from the healing agent loading and magnitude of reinforcement in most cases much higher than that offered by the polymer capsules. Moreover, the compatibility of the inorganic nanomaterials with epoxy is well understood.

Kirk *et al*. [70] encapsulated both epoxy and hardener separately inside channels of nanoporous silica using infiltration method. The feasible self-healing approach for the recovery of mechanical properties of epoxy by adding a mixture of epoxy filled nanoporous silica capsules and hardener filled nanoporous silica capsules were proposed by them. In their study, they observed only a partial self-healing, because the amount of healing agents inside the capsule was not large enough to heal large macro cracks analyzed. Hence they claimed the effective use of such self-healing containers for preventing/healing microcracks which are the precursor to macrocrack formation/extension.

Another promising 'green' nanocontainer for healing agents is naturally occurring halloysite nanotube (Figure 7). Halloysite is a two-layered aluminosilicate clay mineral and is available cheaply in thousands of tons from natural deposits. Depending on the deposit, the size of halloysite nanotubes (HNT) vary within 1–15 μm of length and 10–150 nm of inner diameter [71].

Halloysite can readily dispersed in epoxy without any surface treatment. It was reported that the halloysite nanotubes could act as impact and toughness modifier for epoxy [72, 73]. Abdullayev and Lvov [74, 75] reviewed the use of halloysite clay nanotubes for controlled release of protective agents for medical and pharmaceutical applications, anticorrosive and self-healing coatings etc.

Melo *et al*. [76] encapsulated solvents inside the halloysite lumen and they investigated the feasibility to use them for developing self-healing epoxy. After the insertion of the solvent (DMSO) inside HNT using vacuum infiltration, additional encapsulation using polyelectrolytes was done to block the ends of the HNT in order to trap the solvent inside the structure (Figure 8). This solvent encapsulated HNT can be effectively used in epoxy to make it self-healing in the future. Generally, high molecular weight substances like polymers (epoxy resin) have slow release time due to their stronger adsorption to the halloysite surface. This stronger adsorption is expected due the fact that the high molecular weight substances have more functional groups that can interact with OH groups in halloysite surface to establish hydrogen bonding. Hence no need for additional encapsulation in such case [74].

For self-healing coatings, the corrosion inhibitors are usually loaded as the healing agent inside the nanocontainers. Halloysite nanotubes were successfully used as container for corrosion inhibitor for paints

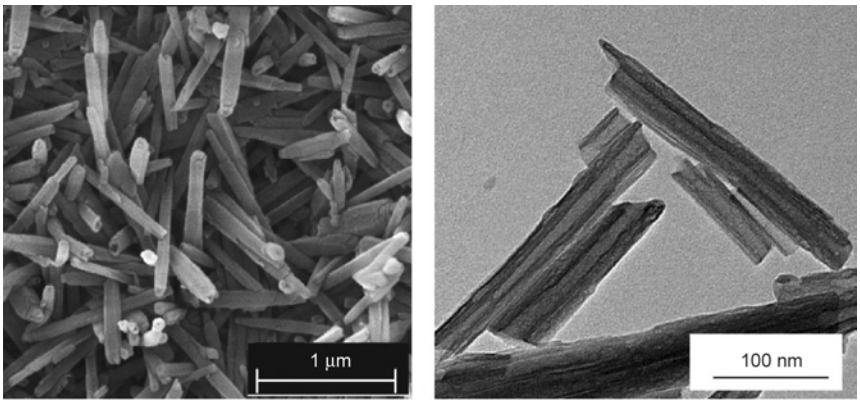

Figure 7. (a) SEM and (b) TEM images of halloysite nanotubes [78]

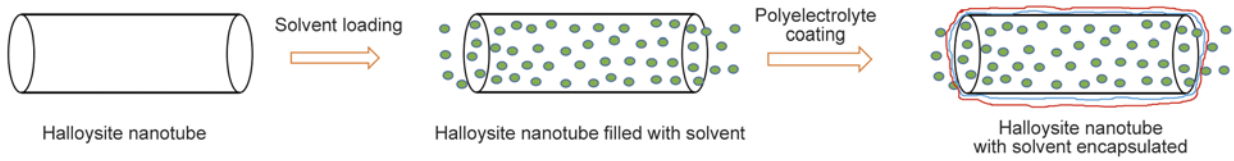

Figure 8. Encapsulation process of solvent into HNTs [76]

[77] and acrylic and polyurethane coatings [78]. While the halloysite inner void loaded with the corrosion inhibitor, the outer surface was covered with polyelectrolyte multilayers. The polyelectrolyte multilayers are sensitive to changes in the surrounding environment. The opening of the polyelectrolyte layer with pH changes resulted in occasional release of inhibitor in local corrosion areas. Once the corrosion area is healed, the pH shifted to its original value which could stop the release of corrosion inhibitor by closing the polyelectrolyte shell.

The similar corrosion inhibitor loaded halloysite nanotubes will be a promising candidate to generate self-healing anticorrosive epoxy protective coating for metals. Mesoporous silica was also used to load corrosion inhibitors for sol-gel protective coating for metal [79].

Maia *et al*. [80] adopted a one step process including synthesis of silica nanocapsules (SiNC) and loading of corrosion inhibitor 2-mercaptobenzothiazole (MBT) which outlook the mass production. This process route provided silica nanocontainers with an empty core and shell with gradual mesoporosity, which facilitates better loading efficiency and prolonged and stimuli-triggered release of the inhibitor. When incorporating these loaded silica nanocapsules into water-based epoxy system to coat aluminium alloy, the SiNC release a higher amount of MBT in acidic pH and at high concentrations of NaCl. This facilitated prolonged self-healing for long time in corrosive media.

Epoxy coatings containing corrosion inhibitor (MBT) loaded mesoporous silica was proved to have self-healing properties [81]. It was showed that epoxy coating with 4 wt% MBT loaded mesoporous silica had partial recovery from artificially created defects as shown by it response to EIS analysis when exposed to 3.5 wt% NaCl solution. Although a decrease in impedance values in the low-frequency range was observed during the first day, impedance values increased after 24 hours of immersion (Figure 9).

Moreover, the inherent corrosion protection capability of halloysite nanotubes and silica nanoparticles [82] will be an added advantage for epoxy coating incorporated with these inorganic materials loaded with corrosion inhibitors. Previously, it was shown that HNTs enhanced the corrosion protection capability of epoxy coating for a carbon steel substrate along with nanozinc dust [83].

Above all, the dimension of the epoxy monomer (diglycidyl ether of bisphenol A) (as per the molecular dynamic simulation studies) [84] is suitable to be loaded even inside the pores in meso-scale. Suzuki *et al*. [85] showed that the pore size in mesoporous silica (~4 nm) is sufficiently large enough for epoxy polymers (~0.5 nm) to penetrate into the internal mesospace. Hence, it is feasible to insert the epoxy monomers into the mesopores and nanotubes due to capillary force.

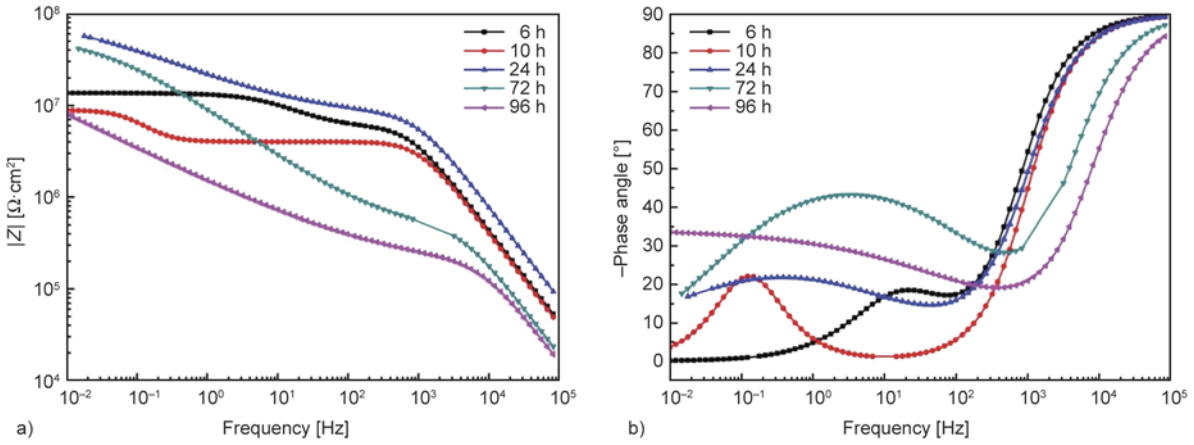

Figure 9. Electrochemical impedance spectroscopy bode plots of epoxy-4 wt% silica–MBT coating after artificial defect exposure to 0.1 mol·L⁻1 NaCl solution [81]

6. Carbon nanotubes (CNT) as containers for self-healing agents

The ability of carbon nanotubes to act as reservoirs for the self-healing agents has been investigated. As a primary research in this area, Lanzara *et al*. [86] studied the feasibility of using CNTs as containers for healing agents by understanding the molecular dynamics (MD) of a fluid which resembles an organic healing agent leaking out of a damaged single-walled CNT. As the crack propagates through the matrix the following would happen, (1) a CNT nanocontainer which would first slow down crack propagation, (2) then release the healing agent as the outer wall of the CNT is damaged and (3) finally CNT would seal back. This MD simulation suggested a new way of using carbon nanotubes as a reinforcing self-healing reservoir that have the potential to reduce the damage through the host matrix, self-repair the crack and at the same time strengthen the material before and after the repairing process.

Later, Sinha-Ray *et al*. [56] loaded the healing agents like DCPD and isophorone diisocyanate into CNTs by using self-sustained diffusion method. In this method, CNTs were blended with dilute solution of self-healing agents in benzene by means of sonication and the Fickian diffusion of healing agent equilibrate the healing agent concentration inside CNTs with that in the bulk. In order to avoid a halt in the intercalation process at this low solute concentration inside CNTs, the solution with suspended CNTs was left to evaporate. The bulk concentration of solute gradually increased due to the solvent lost and this permanently sustained the Fickian diffusion of the solute into CNTs, which allowed complete filling of the CNT bore. The TEM images of CNT samples intercalated with DCPD and isophorone diisocyanate (Figure 10) showed that the filled CNT with the healing agents. The amorphous turbostratic CNTs used in this work could be easily broken as evident form the partially broken wall by the sonication process (Figure 10b), which confirmed the possible release of the healing agents as formation of defect.

7. Combination of containers for self-healing epoxy composites and coating

Researchers utilized the combined benefit of different containers so as to achieve advanced self-healing ability. Encapsulated polymer and inorganic capsules are used together in epoxy matrix for the strength restoration [87]. Hollow silica capsules encapsulated with an instant hardener (antimony pentafluoride) in the form of antimony pentafluoride–ethanol complex and epoxy monomer encapsulated by PMF were incorporated into epoxy matrix. This system could effectively healed within few seconds and about 8.3% impact strength was recovered after 20 s. Within a healing time of 100 s, this system could reached its maximum healing efficiency (Figure 11).

PUF microcapsules loaded with epoxy and etched hollow glass bubbles (HGBs) loaded with amine were simultaneously used to produce self- healing epoxy composite [88]. The amount and the mass ratio of the released healing agents at the damaged area were found to depend on parameters like size, content and core capacity of the healing agent containers. The longest diffusion distance from their carriers is also critically influence the self-healing

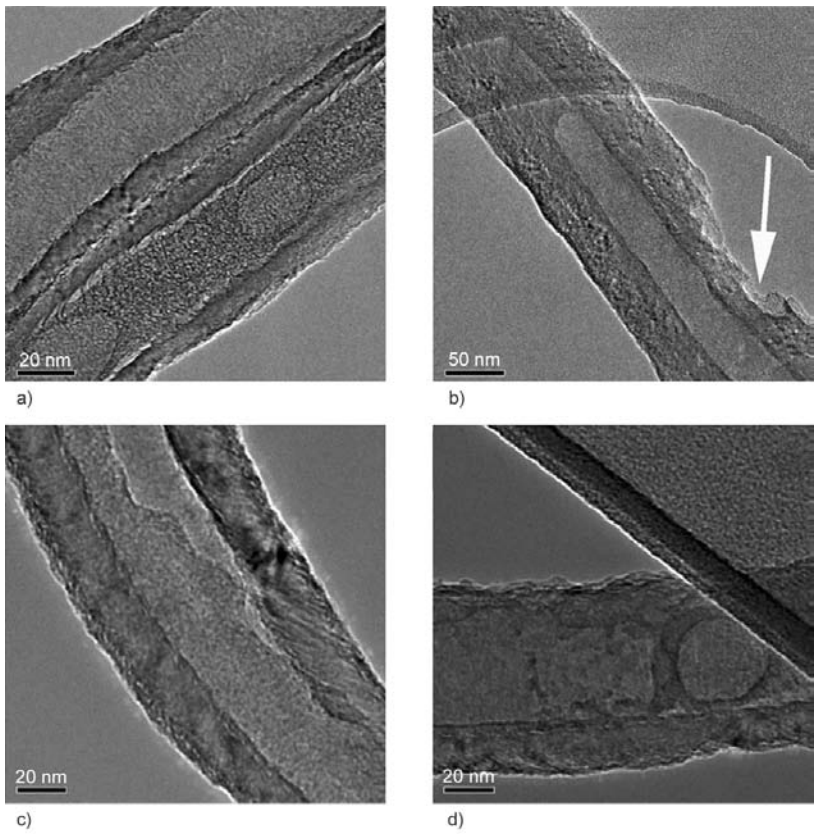

Figure 10. TEM images of the intercalated self-healing materials inside CNTs. Panels (a) and (b) show DCPD inside CNTs, while (c) and (d) show isophorone diisocyanate inside CNTs. In panel (b) the arrow indicates the partially broken CNT wall [56]

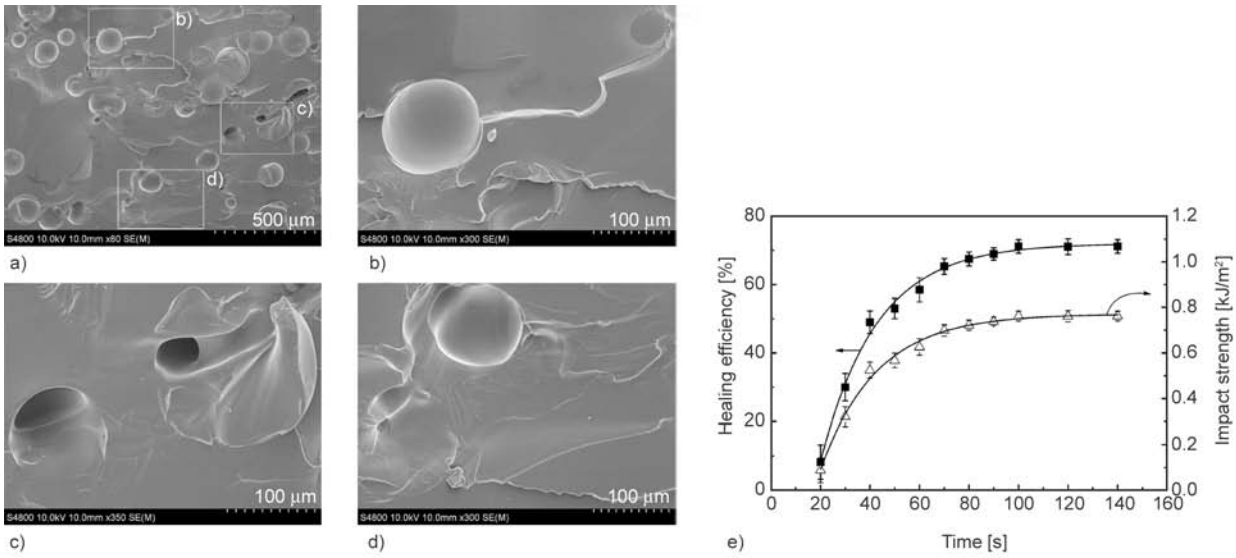

Figure 11. (a) SEM image of impact fracture surface of healed self-healing epoxy matrix with hardener encapsulated silica capsules and epoxy encapsulated PMF. The specimen had been fractured by the first impact test, healed at 25 °C for 100 s, and then fractured again by the second impact test. (b–d) Magnified views of different parts of (a): (e) healing efficiency versus healing time of self-healing specimens determined by impact test [87].

process in the two-part system. With a shorter diffusion distance at higher concentrations and efficient mixing lead to an improved healing performance.

8. The role of container parameters on self-healing performance of epoxy

One of the most important factors which affects the self-healing performance of epoxy system is the

easiness in releasing the healing agent upon damage and this in turn depends on the thickness of the container walls, container composition and container core composition. Researchers used characteristic techniques such as Fourier transform infrared spectroscopy, scanning electron microscopy, particle size analyzer for evaluating these parameters of the capsules. Both the size and weight fraction of the microcapsule control the amount of healing agent released in the damaged plane and hence the degree of self-healing achieved. At a given weight fraction, larger microcapsules produce superior healing performance because the release of more healing agent per unit crack area [89]. Encapsulation of containers can be verified quantitatively and qualitatively by Fourier transform infrared analysis, X-ray diffraction, Brunauer-Emmett-Teller (BET) surface area, thermogravimetry and SEM.

Moreover, the competition between polymerization kinetics and crack increase rate is one of the factors for effective self-healing [90]. It was reported that a significant crack arrest and life-extension occurred when the healing rate is more than the growth rate of the damage. The effect of healing agent encapsulated microcapsule on epoxy cure kinetics was investigated [91]. The mechanism (autocatalytic) of epoxy cure reaction was found to be unaltered by the presence of the healing components responsible for the introduction of healing functionality such as resin encapsulated PUF and amine hardener immobilized on a mesoporous siliceous substrate.

9. Conclusions

The high cost of active monitoring and external repairing in epoxy structural materials can be better eliminated by introducing self-healing ability in them [92], for example corrosion cost reached 4.2% of the gross national product (GNP) of a country for 12 national surveys up to 2010 [93]. Similarly, the large economic concerns raised by corrosion of metallic structures, forces the researchers to search for cost effective self-healing coatings. With proper selection of containers, it could be possible to develop robust, cost-effective and highly efficient epoxy self-healing technologies so as to offer better service life to protective coatings, construction, aerospace, and electronics structures. The introduction of less expensive and possible green healing components in epoxy self-healing coating and composites material were reported. The use of catalyst free healing agents like solvents, epoxy resins etc. were developed in search for cost reduction. Due to the difficulty in encapsulating the amine hardener inside the common polymer capsules like PUF and PMF, PMMA based capsules loaded with epoxy and amine hardener can be a better choice to maintain the epoxy chemistry in the damage area even after the recovery. The novel preparation methods based on Pickering emulsion to achieve solid particle stabilized microcapsules and miniemulsion techniques to achieve the polymer nanocapsules are found to be promising in the area.

The ease of availability, better response to submicron crack, the easy penetration of epoxy monomer into the nano/meso pore and the ability to enhance the matrix properties are the advantages of the inorganic nanotubes as healing agent container for epoxy. Along with the capability to store the healing agent possessed by these inorganic nanomaterials, the inherent corrosion protection ability and their contribution to mechanical reinforcement to the matrix makes them a promising candidate as self-healing containers for developing multifunctional epoxy for structural composites and coating. For developing economically viable self-healing technology, along with the use of low-cost healing agents, the exploitation of readily available, cheaper and green containers like halloysite [94, 95] and nanoclay or lignin nanoparticle-stabilized Pickering emulsion templates are promising. Even though the studies are in the preliminary stage, the capability of CNT can also be effective as containers in epoxy self-healing technology. Moreover, the use of low cost lab-made electrospinning techniques open up promising future for the self- healing technology.

Abbreviations

CFRP	Carbon fiber reinforced polymer
CNT	Carbon nanotube
DCPD	Dicyclopentadiene
DETA	Diethylenetriamine
DMF	Dimethyl formamide
DMSO	Dimethyl sulfoxide
EDA	Ethylenediamine
EIS	Electrochemical impedance spectroscopy
GNP	Gross national product
HDI	Hexamethylene diisocyanate
HGB	Hollow glass bubbles
HGF	Hollow glass fibers
HNT	Halloysite nanotubes
IPDI	Isophorone diisocyanate

MBT	2-mercaptobenzothiazole
MD	Molecular dynamics
MUF-	Melamine–urea–formaldehyde
PAN	Polyacrylonitrile
PAN	Polyacrylonitrile
PLLA	Poly(L -lactide)
PMF	Poly(melamine-formaldehyde)
PMMA	Poly(methylmethacrylate)
Poly(GMA-*co*-MMA)	Poly(glycidylmethacrylatemethylmethacrylate)
PUF	Poly(urea-formaldehyde)
PVAc	Poly(vinyl acetate)
PVA	Poly(vinyl alcohol)
PVCi	Poly(vinyl cinnamate)
PVF	Poly(vinyl formal)
ROMP	Ring-opening metathesis polymerization
SEM	Scanning electron microscopic
SiNC	Silica nanocapsules

Acknowledgements

This review report was made possible by PDRA grant # PDRA1-1216-13014 from the Qatar National Research Fund (a member of Qatar Foundation). The findings achieved herein are solely the responsibility of the authors.

References

[1] Pascault J-P., Williams R. J. J.: Epoxy polymers: New materials and innovations. Wiley-VCH, Weinheim (2010).
DOI: 10.1002/9783527628704

[2] Ellis B.: Chemistry and technology of epoxy resins. Springer, Berlin (1993).

[3] Afendi M., Abdul Majid M. S., Daud R., Abdul Rahman A., Teramoto T.: Strength prediction and reliability of brittle epoxy adhesively bonded dissimilar joint. International Journal of Adhesion and Adhesives, **45**, 21–31 (2013).
DOI: 10.1016/j.ijadhadh.2013.03.008

[4] Takahashi I., Ushijima M.: Detection of fatigue cracks at weld toes by crack detection paint and surface SH wave. Materials Transactions, **48**, 1190–1195 (2007).
DOI: 10.2320/matertrans.I-MRA2007845

[5] Mittal V.: Self-healing anti-corrosion coatings for applications in structural and petrochemical engineering. in 'Handbook of smart coatings for materials protection' (ed.: Makhlouf A. S. H.) Woodhead, Cambridge, 183, 197 (2014).
DOI: 10.1533/9780857096883.2.183

[6] Lamaka S. V., Zheludkevich M. L., Yasakau K. A., Serra R., Poznyak S. K., Ferreira M. G. S.: Nanoporous titania interlayer as reservoir of corrosion inhibitors for coatings with self-healing ability. Progress in Organic Coatings, **58**, 127–135 (2007).
DOI: 10.1016/j.porgcoat.2006.08.029

[7] Hughes A. E., Cole I. S., Muster T. H., Varley R. J.: Designing green, self-healing coatings for metal protection. NPG Asia Materials, **2**, 143–151 (2010).
DOI: 10.1038/asiamat.2010.136

[8] White S. R., Sottos N. R., Geubelle P. H., Moore J. S., Kessler M. R., Sriram S. R., Brown E.N., Viswanathan S.: Autonomic healing of polymer composites. Nature, **409**, 794–797 (2001).
DOI: 10.1038/35057232

[9] Binder W. H.: Self-healing polymers: From principles to applications. Wiley-VCH, Weinheim (2010).
DOI: 10.1002/9783527670185

[10] Wool R. P.: Self-healing materials: A review. Soft Matter, **4**, 400–418 (2008).
DOI: 10.1039/b711716g

[11] Yuan Y. C., Yin T., Rong M. Z., Zhang M. Q.: Self healing in polymers and polymer composites. Concepts, realization and outlook: A review. Express Polymer Letters, **2**, 238–250 (2008).
DOI: 10.3144/expresspolymlett.2008.29

[12] Samadzadeh M., Boura S. H., Peikari M., Kasiriha S. M., Ashrafi A.: A review on self-healing coatings based on micro/nanocapsules. Progress in Organic Coatings, **68**, 159–164 (2010).
DOI: 10.1016/j.porgcoat.2010.01.006

[13] Wu D. Y., Meure S., Solomon D.: Self-healing polymeric materials: A review of recent developments. Progress in Polymer Science, **33**, 479–522 (2008).
DOI: 10.1016/j.progpolymsci.2008.02.001

[14] Yang Y., Urban M. W.: Self-healing polymeric materials. Chemical Society Reviews, **42**, 7446–7467 (2013).
DOI: 10.1039/c3cs60109a

[15] Shchukin D. G.: Container-based multifunctional self-healing polymer coatings. Polymer Chemistry, **4**, 4871–4877 (2013).
DOI: 10.1039/c3py00082f

[16] Fayyad E. M., Al-Ali AlMa'adeed M., Jones A., Abdullah A. M.: Evaluation techniques for the corrosion resistance of self-healing coatings. International Journal of Electrochemical Science, **9**, 4989–5011 (2014).

[17] Teixeira R. F. A., Hillewaere X. K. D., Billiet S., Du Prez F. E.: Chemistry of crosslinking processes for self-healing polymers. in 'Self-healing polymers' (Ed.: Binder W. H.) Wiley-VCH, Weinheim, 215–246 (2010).
DOI: 10.1002/9783527670185.ch9

[18] Brown E. N., Kessler M. R., Sottos N. R., White S. R.: *In situ* poly(urea-formaldehyde) microencapsulation of dicyclopentadiene. Journal of Microencapsulation, **20**, 719–730 (2003).
DOI: 10.3109/02652040309178083

[19] Caruso M. M., Delafuente D. A., Ho V., Sottos N. R., Moore J. S., White S. R.: Solvent-promoted self-healing epoxy materials. Macromolecules, **40**, 8830–8832 (2007).
DOI: 10.1021/ma701992z

[20] Blaiszik B. J., Caruso M. M., McIlroy D. A., Moore J. S., White S. R., Sottos N. R.: Microcapsules filled with reactive solutions for self-healing materials. Polymer, **50**, 990–997 (2009).
DOI: 10.1016/j.polymer.2008.12.040

[21] Suryanarayana C., Chowdoji Rao K., Kumar D.: Preparation and characterization of microcapsules containing linseed oil and its use in self-healing coatings. Progress in Organic Coatings, **63**, 72–78 (2008)
DOI: 10.1016/j.porgcoat.2008.04.008

[22] Yin T., Rong M. Z., Zhang M. Q., Yang G. C.: Self-healing epoxy composites – Preparation and effect of the healant consisting of microencapsulated epoxy and latent curing agent. Composites Science and Technology, **67**, 201–212 (2007).
DOI: 10.1016/j.compscitech.2006.07.028

[23] Liu X., Zhang H., Wang J., Wang Z., Wang S.: Preparation of epoxy microcapsule based self-healing coatings and their behavior. Surface and Coatings Technology, **206**, 4976–4980 (2012).
DOI: 10.1016/j.surfcoat.2012.05.133

[24] Yuan Y. C., Rong M. Z., Zhang M. Q., Chen J., Yang G. C., Li X. M.: Self-healing polymeric materials using epoxy/mercaptan as the healant. Macromolecules, **41**, 5197–5202 (2008).
DOI: 10.1021/ma800028d

[25] Yuan Y. C., Zhang M. Q., Rong M. Z.: The method to prepare microcapsules containing polythios (in Chinese). Chinese Patent 2007100299901, China (2007).

[26] Jin H., Mangun C. L., Stradley D. S., Moore J. S., Sottos N. R., White S. R.: Self-healing thermoset using encapsulated epoxy-amine healing chemistry. Polymer, **53**, 581–587 (2012).
DOI: 10.1016/j.polymer.2011.12.005

[27] Li Q., Mishra A. K., Kim N. H., Kuila T., Lau K., Lee J. H.: Effects of processing conditions of poly(methylmethacrylate) encapsulated liquid curing agent on the properties of self-healing composites. Composites Part B: Engineering, **49**, 6–15 (2013).
DOI: 10.1016/j.compositesb.2013.01.011

[28] McIlroy D. A., Blaiszik B. J., Caruso M. M., White S. R., Moore J. S., Sottos N. R.: Microencapsulation of a reactive liquid-phase amine for self-healing epoxy composites. Macromolecules, **43**, 1855–1859 (2010).
DOI: 10.1021/ma902251n

[29] Yi H., Yang Y., Gu X., Huang J., Wang C.: Multilayer composite microcapsules synthesized by Pickering emulsion templates and their application in self-healing coating. Journal of Materials Chemistry A, **3**, 13749–13757 (2015).
DOI: 10.1039/C5TA02288F

[30] Blaiszik B. J., Sottos N. R., White S. R.: Nanocapsules for self-healing materials. Composites Science and Technology, **68**, 978–986 (2008).
DOI: 10.1016/j.compscitech.2007.07.021

[31] Zhao Y., Fickert J., Landfester K., Crespy D.: Encapsulation of self-healing agents in polymer nanocapsules. Small, **8**, 2954–2958 (2012).
DOI: 10.1002/smll.201200530

[32] Lee J., Zhang M., Bhattacharyya D., Yuan Y. C., Jayaraman K., Mai Y. W.: Micromechanical behavior of self-healing epoxy and hardener-loaded microcapsules by nanoindentation. Materials Letters, **76**, 62–65 (2012).
DOI: 10.1016/j.matlet.2012.02.052

[33] Brown E. N., White S. R., Sottos N. R.: Microcapsule induced toughening in a self-healing polymer composite. Journal of Materials Science, **39**, 1703–1710 (2004).
DOI: 10.1023/B:JMSC.0000016173.73733.dc

[34] Brown E. N., White S. R., Sottos N. R.: Fatigue crack propagation in microcapsule-toughened epoxy. Journal of Materials Science, **41**, 6266–6273 (2006).
DOI: 10.1007/s10853-006-0512-y

[35] Yuan L., Liang G-Z., Xie J-Q., Li L., Guo J.: The permeability and stability of microencapsulated epoxy resins. Journal of Materials Science, **42**, 4390–4397 (2007).
DOI: 10.1007/s10853-006-0606-6

[36] Brown E. N., Sottos N. R., White S. R.: Fracture testing of a self-healing polymer composite. Experimental Mechanics, **42**, 372–379 (2002).
DOI: 10.1007/BF02412141

[37] Kessler M., Sottos N., White S.: Self-healing structural composite materials. Composites Part A: Applied Science and Manufacturing, **34**, 743–753 (2003).
DOI: 10.1016/S1359-835X(03)00138-6

[38] Noh H. H., Lee J. K.: Microencapsulation of self-healing agents containing a fluorescent dye. Express Polymer Letters, **7**, 88–94 (2013).
DOI: 10.3144/expresspolymlett.2013.8

[39] Caruso M. M., Blaiszik B. J., White S. R., Sottos N. R., Moore J. S.: Full recovery of fracture toughness using a nontoxic solvent-based self-healing system. Advanced Functional Materials, **18**, 1898–1904 (2008).
DOI: 10.1002/adfm.200800300

[40] Coope T. S., Mayer U. F. J., Wass D. F., Trask R. S., Bond I. P.: Self-healing of an epoxy resin using scandium(III) triflate as a catalytic curing agent. Advanced Functional Materials, **21**, 4624–4631 (2011).
DOI: 10.1002/adfm.201101660

[41] Neuser S., Michaud V., White S. R.: Improving solvent-based self-healing materials through shape memory alloys. Polymer, **53**, 370–378 (2012).
DOI: 10.1016/j.polymer.2011.12.020

[42] Neuser S., Michaud V.: Fatigue response of solvent-based self-healing smart materials. Experimental Mechanics, **54**, 293–304 (2014).
DOI: 10.1007/s11340-013-9787-5

[43] Yuan Y. C., Rong M. Z., Zhang M. Q., Yang G. C., Zhao J. Q.: Self-healing of fatigue crack in epoxy materials with epoxy/mercaptan system. Express Polymer Letters, **5**, 47–59 (2011).
DOI: 10.3144/expresspolymlett.2011.6

[44] Li Q., Siddaramaiah, Kim N. H., Hui D., Lee J. H.: Effects of dual component microcapsules of resin and curing agent on the self-healing efficiency of epoxy. Composites Part B: Engineering, **55**, 79–85 (2013). DOI: 10.1016/j.compositesb.2013.06.006

[45] Khoee S., Kachoei Z.: Design and development of novel reactive amine nanocontainers for a self-healing epoxy adhesive: Self-repairing investigation using the lap shear test. RSC Advances, **5**, 21023–21032 (2015). DOI: 10.1039/C4RA16344C

[46] Chowdhury R. A., Hosur M. V., Nuruddin M., Tcherbi-Narteh A., Kumar A., Boddu V., Jeelani S.: Self-healing epoxy composites: Preparation, characterization and healing performance. Journal of Materials Research and Technology, **4**, 33–43 (2015). DOI: 10.1016/j.jmrt.2014.10.016

[47] Karger-Kocsis J., Mahmood H., Pegoretti A.: Recent advances in fiber/matrix interphase engineering for polymer composites. Progress in Materials Science, **73**, 1–43 (2015). DOI: 10.1016/j.pmatsci.2015.02.003

[48] Jones A. R., Cintora A., White S. R., Sottos N. R.: Autonomic healing of carbon fiber/epoxy interfaces. ACS Applied Materials Interfaces, **6**, 6033–6039 (2014). DOI: 10.1021/am500536t

[49] Jones A. R., Blaiszik B. J., White S. R., Sottos N. R.: Full recovery of fiber/matrix interfacial bond strength using a microencapsulated solvent-based healing system. Composites Science and Technology, **79**, 1–7 (2013). DOI: 10.1016/j.compscitech.2013.02.007

[50] Ahangari M. G., Fereidoon A.: Micromechanical properties and morphologies of self-healing epoxy nanocomposites with microencapsulated healing agent. Materials Chemistry and Physics, **151**, 112–118 (2015). DOI: 10.1016/j.matchemphys.2014.11.044

[51] Stankiewicz A., Szczygieł I., Szczygieł B.: Self-healing coatings in anti-corrosion applications. Journal of Materials Science, **48**, 8041–8051 (2013). DOI: 10.1007/s10853-013-7616-y

[52] Jadhav R. S., Hundiwale D. G., Mahulikar P. P.: Synthesis and characterization of phenol–formaldehyde microcapsules containing linseed oil and its use in epoxy for self-healing and anticorrosive coating. Journal of Applied Polymer Science, **119**, 2911–2916 (2011). DOI: 10.1002/app.33010

[53] Samadzadeh M., Boura S. H., Peikari M., Ashrafi A., Kasiriha M.: Tung oil: An autonomous repairing agent for self-healing epoxy coatings. Progress in Organic Coatings, **70**, 383–387 (2011). DOI: 10.1016/j.porgcoat.2010.08.017

[54] Zhang H., Wang J., Liu X., Wang Z., Wang S.: High performance self-healing epoxy/polyamide protective coating containing epoxy microcapsules and polyaniline nanofibers for mild carbon steel. Industrial and Engineering Chemistry Research, **52**, 10172–10180 (2013). DOI: 10.1021/ie400666a

[55] Sun D., An J., Wu G., Yang J.: Double-layered reactive microcapsules with excellent thermal and non-polar solvent resistance for self-healing coatings. Journal of Materials Chemistry A, **3**, 4435–4444 (2015). DOI: 10.1039/C4TA05339G

[56] Sinha-Ray S., Pelot D. D., Zhou Z. P., Rahman A., Wu X-F., Yarin A. L.: Encapsulation of self-healing materials by coelectrospinning, emulsion electrospinning, solution blowing and intercalation. Journal of Materials Chemistry, **22**, 9138–9146 (2012). DOI: 10.1039/c2jm15696b

[57] Wu X-F., Rahman A., Zhou Z., Pelot D. D., Sinha-Ray S., Chen B., Yarin A. L.: Electrospinning core-shell nanofibers for interfacial toughening and self-healing of carbon-fiber/epoxy composites. Journal of Applied Polymer Science, **129**, 1383–1393 (2013). DOI: 10.1002/app.38838

[58] Mitchell T. J., Keller M. W.: Coaxial electrospun encapsulation of epoxy for use in self-healing materials. Polymer International, **62**, 860–866 (2013). DOI: 10.1002/pi.4397

[59] Yarin A. L., Zussman E., Wendorff J. H., Greiner A.: Material encapsulation and transport in core–shell micro/nanofibers, polymer and carbon nanotubes and micro/nanochannels. Journal of Materials Chemistry, **17**, 2585–2599 (2007). DOI: 10.1039/b618508h

[60] Yarin A. L.: Coaxial electrospinning and emulsion electrospinning of core–shell fibers. Polymers for Advanced Technologies, **22**, 310–317 (2011). DOI: 10.1002/pat.1781

[61] Vahedi V., Pasbakhsh P., Piao C. S., Seng C. E.: A facile method for preparation of self-healing epoxy composites: using electrospun nanofibers as microchannels. Journal of Materials Chemistry A, **3**, 16005–16012 (2015). DOI: 10.1039/C5TA02294K

[62] Pang J. W. C., Bond I. P.: A hollow fibre reinforced polymer composite encompassing self-healing and enhanced damage visibility. Composites Science and Technology, **65**, 1791–1799 (2005). DOI: 10.1016/j.compscitech.2005.03.008

[63] Trask R. S., Bond I. P.: Biomimetic self-healing of advanced composite structures using hollow glass fibres. Smart Materials and Structures, **15**, 704–710 (2006). DOI: 10.1088/0964-1726/15/3/005

[64] Trask R. S., Williams G. J., Bond I. P.: Bioinspired self-healing of advanced composite structures using hollow glass fibres. Journal of the Royal Society Interface, **4**, 363–371 (2007). DOI: 10.1098/rsif.2006.0194

[65] Mehta N. K.: Self-healing fiber-reinforced epoxy composites: Solvent-epoxy filled hollow glass fibers. International Journal of Composite Materials, **3**, 145–155 (2013). DOI: 10.5923/j.cmaterials.20130306.02

[66] Williams G., Trask R., Bond I.: A self-healing carbon fibre reinforced polymer for aerospace applications. Composites Part A: Applied Science and Manufacturing, **38**, 1525–1532 (2007).
DOI: 10.1016/j.compositesa.2007.01.013

[67] Kling S., Czigány T.: Damage detection and self-repair in hollow glass fiber fabric-reinforced epoxy composites *via* fiber filling. Composites Science and Technology, **99**, 82–88 (2014).
DOI: 10.1016/j.compscitech.2014.05.020

[68] Zhang H., Yang J.: Etched glass bubbles as robust micro-containers for self-healing materials. Journal of Materials Chemistry A, **1**, 12715–12720 (2013).
DOI: 10.1039/C3TA13227G

[69] Zhang H., Wang P., Yang J.: Self-healing epoxy via epoxy–amine chemistry in dual hollow glass bubbles. Composites Science and Technology, **94**, 23–29 (2014).
DOI: 10.1016/j.compscitech.2014.01.009

[70] Kirk J. G., Naik S., Moosbrugger J. C., Morrison D. J., Volkov D., Sokolov I.: Self-healing epoxy composites based on the use of nanoporous silica capsules. International Journal of Fracture, **159**, 101–102 (2009).
DOI: 10.1007/s10704-009-9375-y

[71] Liu M., Guo B., Du M., Cai X., Jia D.: Properties of halloysite nanotube–epoxy resin hybrids and the interfacial reactions in the systems. Nanotechnology, **18**, 455703/1–455703/9 (2007).
DOI: 10.1088/0957-4484/18/45/455703

[72] Ye Y., Chen H., Wu J., Ye L.: High impact strength epoxy nanocomposites with natural nanotubes. Polymer, **48**, 6426–6433 (2007).
DOI: 10.1016/j.polymer.2007.08.035

[73] Deng S., Zhang J., Ye L., Wu J.: Toughening epoxies with halloysite nanotubes. Polymer, **49**, 5119–5127 (2008).
DOI: 10.1016/j.polymer.2008.09.027

[74] Abdullayev E., Lvov Y.: Halloysite clay nanotubes for controlled release of protective agents. Journal of Nanoscience and Nanotechnology, **11**, 10007–10026 (2011).
DOI: 10.1166/jnn.2011.5724

[75] Lvov Y., Abdullayev E.: Functional polymer–clay nanotube composites with sustained release of chemical agents. Progress in Polymer Science, **38**, 1690–1719 (2013).
DOI: 10.1016/j.progpolymsci.2013.05.009

[76] Melo J. D. D., Barbosa A. P. C., Costa M. C. B., de Melo G. N.: Encapsulation of solvent into halloysite nanotubes to promote self-healing ability in polymers. Advanced Composite Materials, **23**, 507–519 (2014).
DOI: 10.1080/09243046.2014.915116

[77] Abdullayev E., Lvov Y.: Clay nanotubes for corrosion inhibitor encapsulation: Release control with end stoppers. Journal of Materials Chemistry, **20**, 6681–6687 (2010).
DOI: 10.1039/c0jm00810a

[78] Abdullayev E., Abbasov V., Tursunbayeva A., Portnov V., Ibrahimov H., Mukhtarova G., Lvov Y.: Self-healing coatings based on halloysite clay polymer composites for protection of copper alloys. ACS Applied Materials and Interfaces, **5**, 4464–4471 (2013).
DOI: 10.1021/am400936m

[79] Skorb E. V., Fix D., Andreeva D. V., Möhwald H., Shchukin D. G.: Surface-modified mesoporous SiO_2 containers for corrosion protection. Advanced Functional Materials, **19**, 2373–2379 (2009).
DOI: 10.1002/adfm.200801804

[80] Maia F., Tedim J., Lisenkov A. D., Salak A. N., Zheludkevich M. L., Ferreira M. G. S.: Silica nanocontainers for active corrosion protection. Nanoscale, **4**, 1287–1298 (2012).
DOI: 10.1039/c2nr11536k

[81] Qiao Y., Li W., Wang G., Zhang X., Cao N.: Application of ordered mesoporous silica nanocontainers in an anticorrosive epoxy coating on a magnesium alloy surface. RSC Advances, **5**, 47778–47787 (2015).
DOI: 10.1039/C5RA05266A

[82] Shi X., Nguyen T. A., Suo Z., Liu Y., Avci R.: Effect of nanoparticles on the anticorrosion and mechanical properties of epoxy coating. Surface and Coatings Technology, **204**, 237–245 (2009).
DOI: 10.1016/j.surfcoat.2009.06.048

[83] Moazeni N., Mohamad Z., Faisal N. L. I., Tehrani M. A., Dehbari N.: Anticorrosion epoxy coating enriched with hybrid nanozinc dust and halloysite nanotubes. Journal of Applied Polymer Science, **130**, 955–960 (2013).
DOI: 10.1002/app.39239

[84] Wang Z., Liang Z., Wang B., Zhang C., Kramer L.: Processing and property investigation of single-walled carbon nanotube (SWNT) buckypaper/epoxy resin matrix nanocomposites. Composites Part A: Applied Science and Manufacturing, **35**, 1225–1232 (2004).
DOI: 10.1016/j.compositesa.2003.09.029

[85] Suzuki N., Kiba S., Yamauchi Y.: Fabrication of mesoporous silica/polymer composites through solvent evaporation process and investigation of their excellent low thermal expansion property. Physical Chemistry Chemical Physics, **13**, 4957–4962 (2011).
DOI: 10.1039/c0cp02071k

[86] Lanzara G., Yoon Y., Liu H., Peng S., Lee W-I.: Carbon nanotube reservoirs for self-healing materials. Nanotechnology, **20**, 335704/1–335704/7 (2009).
DOI: 10.1088/0957-4484/20/33/335704

[87] Ye X. J., Zhang J-L., Zhu Y., Rong M. Z., Zhang M. Q., Song Y. X., Zhang H-X.: Ultrafast self-healing of polymer toward strength restoration. ACS Applied Materials and Interfaces, **6**, 3661–3670 (2014).
DOI: 10.1021/am405989b

[88] Zhang H., Yang J.: Development of self-healing polymers via amine–epoxy chemistry: II. Systematic evaluation of self-healing performance. Smart Materials and Structures, **23**, 065004/1–065004/9 (2014).
DOI: 10.1088/0964-1726/23/6/065004

[89] Rule J. D., Sottos N. R., White S. R.: Effect of microcapsule size on the performance of self-healing polymers. Polymer, **48**, 3520–3529 (2007).
DOI: 10.1016/j.polymer.2007.04.008

[90] Brown E. N., White S. R., Scottos N. R.: Retardation and repair of fatigue cracks in a microcapsule toughened epoxy composite – Part II: *In situ* self-healing. Composites Science and Technology, **65**, 2474–2480 (2005).
DOI: 10.1016/j.compscitech.2005.04.053

[91] Tripathi M., Kumar D., Rajagopal C., Roy P. K.: Curing kinetics of self-healing epoxy thermosets. Journal of Thermal Analysis and Calorimetry, **119**, 547–555 (2014).
DOI: 10.1007/s10973-014-4128-1

[92] Aïssa B., Therriault D., Haddad E., Jamroz W.: Self-healing materials systems: Overview of major approaches and recent developed technologies. Advances in Materials Science and Engineering, **2012**, 854203/1–854203/17 (2012).
DOI: 10.1155/2012/854203

[93] Tems R., Al Zahrani A. M.: Cost of corrosion in oil production and refining. Saudi Aramco Journal of Technology, 2–14 (2006).

[94] Lvov Y. M., Shchukin D. G., Möhwald H., Price R. R.: Halloysite clay nanotubes for controlled release of protective agents. ACS Nano, **2**, 814–820 (2008).
DOI: 10.1021/nn800259q

[95] Kamble R., Ghag M., Gaikawad S., Panda B. K.: Halloysite nanotubes and applications: A review. Journal of Advanced Scientific Research, **3**, 25–26 (2012).